1 *Highly efficient and super-bright neurocircuit tracing using vector*

2 *mixing-based virus cocktail*

3   Pei Sun[1,3,8], Sen Jin[2,4,8], Sijue Tao[1,2,3,8], Junjun Wang[1,3], Anan Li[1,3], Ning Li[1,3], Yang

4   Wu[2], Jianxia Kuang[1,3], Yurong Liu[1,3], Lizhao Wang[7], Huimin Lin[1,3] Xiaohua Lv[1,3],

5   Xiuli Liu[1,3], Jundan Peng[2], Siyu Zhang[7], Min Xu[5], Zhen Luo[2], Xiaobin He[2], Tonghui

6   Xu[1,3], Xiangning Li[1,3], Shaoqun Zeng[1,3], Yu-Hui Zhang[1,3*] and Fuqiang Xu[1,2,3,5*]

7

8   [1]Britton Chance Center for Biomedical Photonics, Wuhan National Laboratory for

9   Optoelectronics-Huazhong University of Science and Technology, Wuhan, Hubei

10   430074, China.

11   [2]Centre for Brain Science, State Key Laboratory of Magnetic Resonance and Atomic

12   Molecular Physics, Key Laboratory of Magnetic Resonance in Biological Systems,

13   Wuhan Institute of Physics and Mathematics, CAS Centre for Excellence in Brain

14   Science and Intelligence Technology, Chinese Academy of Sciences, Wuhan 430071,

15   China.

16   [3]MoE Key Laboratory for Biomedical Photonics, School of Engineering Sciences,

17   Huazhong University of Science and Technology, Wuhan, Hubei 430074, China.

18   [4]Shenzhen Institutes of Advanced Technology, Chinese Academy of Sciences,

19   Shenzhen 518055, China.

20   [5]Brain Cognition and Brain Disease Institute (BCBDI), Shenzhen Institutes of

21   Advanced Technology, Chinese Academy of Sciences, Shenzhen-Hong Kong

22   Institute of Brain Science-Shenzhen Fundamental Research Institutions, Shenzhen

23   518055, China.

24   [6]Institute of Neuroscience, CAS Center for Excellence in Brain Science and

25   Intelligence Technology, Chinese Academy of Sciences, 200031, Shanghai, China.

26   [7]Department of Anatomy and Physiology, Shanghai Jiao Tong University School of

27   Medicine, 200025, Shanghai, China.

28   [8]These authors contributed equally to this work.

29   Correspondence should be addressed to Y.-H. Z (email: zhangyh@mail.hust.edu.cn)

30   or F. X. (email: fuqiang.xu@wipm.ac.cn)

31

32

33

34

35

ABSTRACT

Mapping the detailed cell-type-specific input networks and neuronal projectomes are essential to understand brain function in normal and pathological states. However, several properties of current tracing systems, including labeling sensitivity, trans-synaptic efficiencies, reproducibility among different individuals and different Cre-driver animals, still remained unsatisfactory. Here, we developed MAP-ENVIVIDERS, a recombinase system-dependent vector mixing-based strategy for highly efficient neurocircuit tracing. MAP-ENVIVIDERS enhanced tracing efficiency of input networks across the whole brain, with over 10-fold improvement in diverse previously poor-labeled input brain regions and particularly, up to 70-fold enhancement in brainstem compared with the current standard rabies-virus-mediated systems. MAP-ENVIVIDERS was over 10-fold more sensitive for cell-type-specific labeling than previous strategies, enabling us to capture individual cell-type-specific neurons with extremely complex axonal branches and presynaptic axonal boutons, both about one order of magnitude than previously reported and considered. MAP-ENVIVIDERS provides powerful tools for deconstructing novel input/output circuitry towards functional studies and disorders-related mechanisms.

53

INTRODUCTION

Efficient mapping the input-output circuits of specific cell types is a central goal in neuroscience. Comprehensive tracing presynaptic partners to specific cell types is essential to understand how the input resources and strength received from other brain regions and other type of neurons guided the corresponding behaviors. For cell-type-specific input mapping, currently, rabies virus (RV, SAD B19 strain)-mediated monosynaptic tracing systems with the involvement of two or more recombinant adeno-associated viruses (rAAVs) helpers have been widely used for tracing the direct input network of a given type of neuron[1-6]. However, problems such as underestimated total input numbers, inefficient trans-synaptic abilities, particularly leading to rare labeling in brain regions which were far away from injection site or with weaker input strength, still hindered our further comprehensive characterization of neural circuits[7-9]. To solve this problem, extensive attention has been made via modifying the genome, including engineering of promoters for enhanced regulation strength or improvement of monosynaptic tracing efficiency with optimized glycoprotein (oG) to improve the efficiency of rabies glycopreotein (RG)-expressing helper rAAVs used in current RV-mediated monosynaptic tracing systems[5,10]. Though great achievements have been made with these modifications, strategies to achieve comprehensive improvement of tracing efficiencies across the whole brain, particularly in previously poor-labeled brain regions were still in urgent need.

On the other hand, obtaining detailed single-neuron projectomes at the whole brain level enhances our understanding of input-output relationship of neural circuits and facilitates identification of novel cell types[11]. Though great achievements have been made in full morphology reconstruction of individual neurons belonging to different cell types[11-14], fewer studies have focused on synaptic levels which still remained a great challenge due to the requirement of extremely higher labeling brightness (generally 3-fold higher) to distinguish the tiny-sized boutons (1-2 μm in diameter) from their resided thinner axons[15,16]. Remarkably, understanding detailed axonal projection patterns on synaptic levels facilitate the elucidation of how information flows across diverse brain regions, to what extent individual neurons exert effects on their postsynaptic targets and how synaptic plasticity affects function of individual neurons under the normal and pathological conditions[17,18]. To achieve neuronal sparse labeling with cell-type specificity, current strategy ultilized

87   combinatorial genetic (e.g. Cre-driver animals) and viral method (e.g. rAAVs) based

88   on intersectional gene expressions[19]. In these strategies, cell-type specificity was

89   controlled by Cre-driver animals, labeling sparseness and brightness were mainly

90   controlled by the mixtures of two or more rAAVs expressing essential elements for

91   recombination (e.g. Cre/lox-Flp/FRT or Cre/lox-tTA/TRE combinations) along with

92   the strength of Cre reombinase[13,20,21]. However, due to inhomogeneous strength of

93   Cre recombinase, these labeling systems suffered from varied labeling brightness

94   among different transgenic lines and rather low gene expression levels particularly in

95   transgenic lines with weaker strength of Cre recombinase[21-23]. Thus, to generate

96   detailed single-neuron projectomes of diverse cell types on synaptic levels, the

97   optimal cell-type-specific labeling strategies should be with adjustable sparseness

98   along with achievement of superb-bright labeling in diverse Cre-driver transgenic

99   lines.

100   Overall, almost all current neural circuit labeling strategy involving multiple

101   rAAV vectors focused on modifying viral genomes to improve vector properties of

102   each separately packaged rAAV. However, when used together via co-injections or

103   co-administrations, the labeling efficiencies or brightness of these multiple rAAV

104   vectors still remained unsatisfactory. The probable reason was that such individual,

105   separate improvements failed to consider interactions among different rAAVs. In fact,

106   previous studies indicated that mutual suppression is prevalent among different types

107   of viruses, e.g., AAV over herpes simplex virus[24], AAV over adenovirus[25], or even

108   among the same types of viruses (e.g., herpes simplex virus and pseudorabies virus)[26-

109   28]. Taken these facts, we reasoned that mutual suppression between different rAAVs,

110   though have not been previously reported (to the best of our knowledge), will also

111   significantly affect the gene expression levels. We further reasoned that altering viral

112   packaging strategy, i.e., replacing the package of each viral vector independently by

113   mixing multiple vectors in a single step on cellular level (i.e., copackaging

114   strategy)[29,30] would enhance multi-gene expression efficiencies in neural circuit

115   studies.

116   Based on this hypothesis, we developed MAP-ENVIVIDERS (**m**ultifaceted

117   **a**melioration **p**rocess to **e**nhance **n**eurocircuit **vi**sualization by **vi**ral vectors **de**pending

118   on **r**ecombinase **s**ystems), a recombinase system-dependent viral copackaging-based

119   strategy for highly efficient neural circuit tracing. With MAP-ENVIVIDERS, we

120 achieved: (i) 10- to 70-fold increased tracing efficiencies in 40% of all input brain

121 regions for trans-monosynaptic retrograde tracing with RV-mediated systems; (ii)

122 More than an order of magnitude of labeling brightness for cell-type-specific labeling

123 than previous strategies and unbiased, super-bright labeling among diverse transgenic

124 mice. Combined with whole-brain imaging systems, MAP-ENVIVIDERS enables

125 identification of novel projection patterns and capture presynaptic axonal boutons of

126 individual cell-type-specific neurons with extreme complexity. Finally, we

127 demonstrated that viral copackaging strategy significantly ameliorated mutual

128 suppression among different rAAVs and enhanced compatibility of multi-gene

129 expressions in the same cells, the probable reasons leading to the high sensitivity and

130 efficiency of MAP-ENVIVIDERS.

RESULTS

MAP-ENVIVIDERS substantially improves the efficiency of RV-mediated monosynaptic tracing systems

134 The current RV-mediated trans-monosynaptic tracing systems involve two different

135 processes: the entry of EnvA-pseudotyped, RG-deleted RV (EnvA-RVΔG) into the

136 cells through the interaction of EnvA with TVA receptor delivered by one rAAV, and

137 the assembly of infectious RV by providing RVΔG with the RG delivered by another

138 rAAV[1-6]. To investigate whether MAP-ENVIVIDERS, the recombinase system-

139 dependent viral copackaging strategy would improve the coherence between the

140 TVA-EnvA interaction and RVΔG-RG assembly, and thus leading to a significant

141 increase in the efficiency of trans-monosynaptic labeling with the prevalent rAAV-RV

142 system, we designed MAP-ENVIVIDERS with two Cre-dependent vectors, AAV-

143 DIO-EGFP-TVA (GT) and AAV-DIO-RG (**Fig. 1a**). As an example, we copackaged

144 AAV-DIO-GT and AAV-DIO-RG at a ratio of 1:2 to generate littermate virus, termed

145 lAAV-DIO-GT/RG for convenience (where l refers to littermate hereafter). For

146 comparisons, we packaged the two vectors independently and mixed them at a ratio of

147 1:2, the mixtures were abbreviated for sAAV-DIO-GT/RG (s refers to stranger

148 hereafter; **Fig. 1b**). Since genetically modified, EnvA-pseudotyped RV (EnvA-

149 SADΔG-DsRed) used in two systems were identical, comparisons of tracing

150 efficiencies between lAAV-DIO-GT/RG and sAAV-DIO-GT/RG represented the

151 difference between MAP-ENVIVIDERS and prevalent rAAV-RV system.

152

153
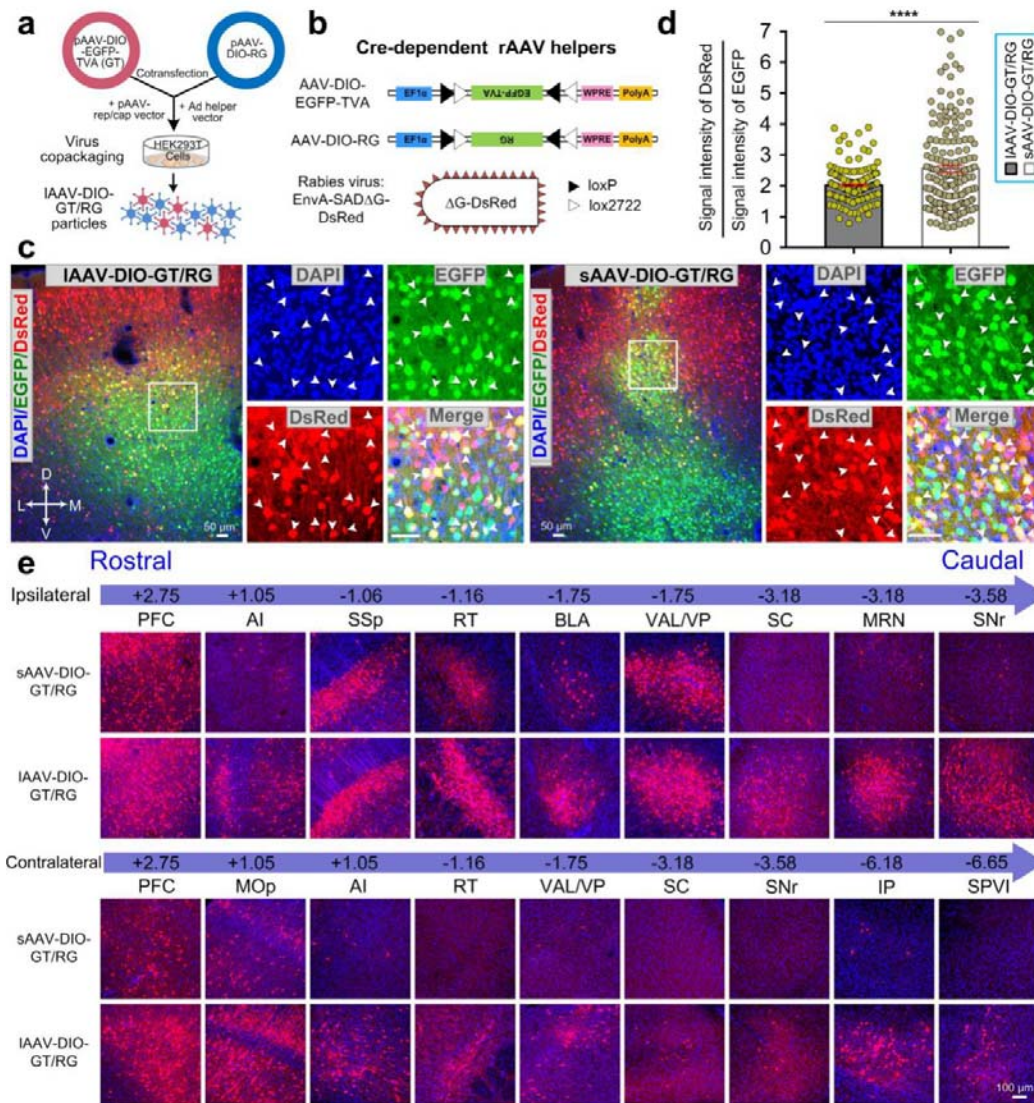
154

Fig. 1 | Demonstration of MAP-ENVIVDERS in tracing direct input networks in MOp. a, Schematic for generating copackaged rAAV helper by MAP-ENVIVDERS (lAAV-DIO-GT/RG). Briefly, two Cre-dependent AAV vectors for the respective expression of TVA and RG were premixed at a ratio of 1:2. **b**, Schematic of the two Cre-dependent rAAV helpers and the EnvA-pseudotyped rabies virus. **c**, Representative coronal sections showing the injection site in lAAV-DIO-GT/RG- and sAAV-DIO-GT/RG-labeled mice. Boxed regions showed colocalization of 4′,6-diamidino-2-phenylindole (DAPI, blue), EGFP (green), and DsRed (red). White arrowheads indicated triple-positive neurons. **d**, Comparison of the ratio between the signal intensity of DsRed and EGFP in starter cells labeled by lAAV-DIO-GT/RG and sAAV-DIO-GT/RG, n = 170 neurons from 3 mice for both groups. **e**, Representative images showing ipsi- and contralateral input neurons in different brain regions labeled by EnvA-pseudotyped rabies virus via lAAV-DIO-GT/RG or sAAV-DIO-GT/RG. Data are

165
166 presented as mean ± s.e.m.; two-tailed t-test, ****P < 0.0001. Abbreviations: see **Supplementary Table 2**.

167

168 We injected equal volume of lAAV-DIO-GT/RG or sAAV-DIO-GT/RG into the
169 primary motor cortex (MOp) of Thy1-Cre transgenic mice, followed by the injection
170 of EnvA-pseudotyped RV 21 days later. Nine days after the second injection, the mice
171 were sacrificed for analysis. We found that the numbers of EGFP[+]/DsRed[+] starter
172 cells in lAAV-DIO-GT/RG and sAAV-DIO-GT/RG groups were similar (2,386 ± 172
173 vs. 2,039 ± 127, n = 5 animals each; **Fig. 1c** and **Supplementary Table 1**) and the
174 value of the DsRed/EGFP ratio[31] closely matched the preset ratio of 2:1 for the lAAV-
175 DIO-GT/RG group but significantly deviated from 2:1 for the sAAV-DIO-GT/RG
176 group (**Fig. 1d** and **Supplementary Fig. 1a**, left panel; 2.01 ± 0.04 versus 2.67 ± 0.13;
177 mean ± s.e.m., unpaired t-test, P < 0.0001, n = 3 mice). Furthermore, the distribution
178 of ratios in individual neurons was significantly narrower for lAAV-DIO-GT/RG than
179 sAAV-DIO-GT/RG (**Fig. 1d**). We next examined the inputs of two labeling groups
180 qualitatively and fluorescent images showed that the improvement granted by the
181 MAP-ENVIVIDERS system was most prominent for highly underrepresented regions
182 far from the injection site, such as the reticular nucleus of the thalamus (RT), the
183 superior colliculus (SC), the midbrain reticular nucleus (MRN) and the substantia
184 nigra pars reticulata (SNr) in midbrain on the ipsilateral side and all regions on the
185 contralateral side, especially the interposed nucleus (IP) in cerebellum and the spinal
186 nucleus of the trigeminal nerve, subnucleus interpolaris (SPVI) in medulla.
187 Furthermore, MAP-ENVIVIDERS also improved the labeling moderately in the brain
188 regions that were well-labeled by the classical sAAV-DIO-GT/RG-RV combination,
189 such as the prefrontal cortex (PFC), the primary somatosensory area (SSp), and the
190 ventral anterior-lateral complex of the thalamus (VAL)/ventral posterior complex of
191 the thalamus (VP) (**Fig. 1e** and **Supplementary Fig. 2**,**3**).
192 To compare the global tracing efficiency of the two systems quantitatively, we
193 continued to divide the whole brain (+3.25 to -7.25 from the bregma) into 11 major
194 regions containing 44 subregions according to the Allen Mouse Brain Atlas and
195 registered the numbers of DsRed-labeled input cells in each subregion[32,33]. We
196 summarized the sparsely labeled input brain regions in sAAV-DIO-GT/RG labeling
197 groups across the whole brain and found that number of input neurons in most of
198 these areas were at least one order of magnitude enhanced by MAP-ENVIVIDERS

199   (lAAV-DIO-GT/RG) (**Fig. 2a**). Such improvements covered diverse levels: (i) from

200   hundreds to several thousands of neurons, such as visceral area (VISC) in cortical

201   subplate (CTXsp), CP and ventral posteromedial nucleus of the thalamus (VPM); (ii)

202   from dozens to several hundreds of neurons: such as central amygdalar nucleus (CEA)

203   in striatum, ventral posterolateral nucleus of the thalamus (VPL), zona incerta (ZI) in

204   hypothalamus, periaqueductal gray (PAG), pretectal region (PRT) and SNr in

205   midbrain; (iii) from dozens to more than one thousands of neurons: such as RT, MRN

206   and superior colliculus, motor related (SCm) in midbrain; (iv) from individuals to one

207   hundreds of neurons, such as parabrachial nucleus (PB) and pontine reticular nucleus,

208   caudal part (PRNc) in pons, gigantocellular reticular nucleus (GRN) and vestibular

209   nuclei (VNC) in medulla, or to several hundreds of neurons, such as substantia nigra,

210   compact part (SNc) in midbrain, IP and dentate nucleus (DN) in cerebellum.

211   To further obtain specific enhanced ratios in diverse major regions and

212   subregions achieved by MAP-ENVIVIDERS, the corresponding convergent index[8]

213   (the number of input cells divided by the number of starter cells) was calculated

214   initially. Then, the ratio between convergent index of lAAV-DIO-GT/RG and

215   convergent index of sAAV-DIO-GT/RG was plotted against the percentage of inputs

216   (input cells in each subregion relative to the total input cells across whole brain). The

217   relationship between the improvement and the labeling efficiency by MAP-

218   ENVIVIDERS is clear: the poorer the labeling with the original system, the greater

219   the improvement (**Fig. 2c**). We found that most of the originally underrepresented

220   regions ($< 1\%$) were enhanced by more than an order of magnitude and these regions

221   were distributed throughout the brain, such as CP (20-fold) in striatum, RT (17-fold)

222   in thalamus, ZI (14-fold) in hypothalamus. Brain regions with over 20-fold (20 to 60-

223   fold) enhanced tracing efficiencies were more frequently found in midbrain, hindbrain

224   and cerebellum, areas which were very far away from injection site, such as SNr (41-

225   fold) and SNc (40-fold) in midbrain; reticular nucleus (gigantocellular: 46.0-fold and

226   intermediate: 44-fold) in medulla; IP (56-fold) and DN (38-fold) in cerebellum,

227   corresponding to the results of fluorescent images in **Fig. 1e**. Particularly, several

228   brain regions in brain stem, including SCm, sensory related (MY-sen) and VNC in

229   medulla, motor related (MY-mot), showed particular improvements of up to 70-fold

230   (**Fig. 2b** and **Supplementary Fig. 4d**).

231   To examine whether brightness of input neurons could be enhanced by MAP-

232   ENVIVIDERS, we further compared the signal intensities of the input neurons traced

233   by lAAV-DIO-GT/RG and sAAV-DIO-GT/RG in the following brain regions: SSp,

234   supplemental somatosensory area (SSs) and RT (**Supplementary Fig. 1a**, right panel).

235   We found that the signal intensities of the input neurons were significantly enhanced

236   in lAAV-DIO-GT/RG labeling groups compared with sAAV-DIO-GT/RG labeling

237   groups (**Fig. 2d** and **Supplementary Fig. 4e**; 2.27-fold for RT, 1.94-fold for SSp and

238   2.19-fold for SSs; unpaired t-test, $P < 0.0001$, n = 3 mice). These data collectively

239   showed that MAP-ENVIVIDERS significantly enhanced not only the number but also

240   the brightness of the labeled input neurons. Taken the facts of similar number of

241   starter cells, significantly enhanced number and fluorescent intensity of input cells

242   suggested that many more RVs are produced by the starter cells in MAP-

243   ENVIVIDERS.

244

245
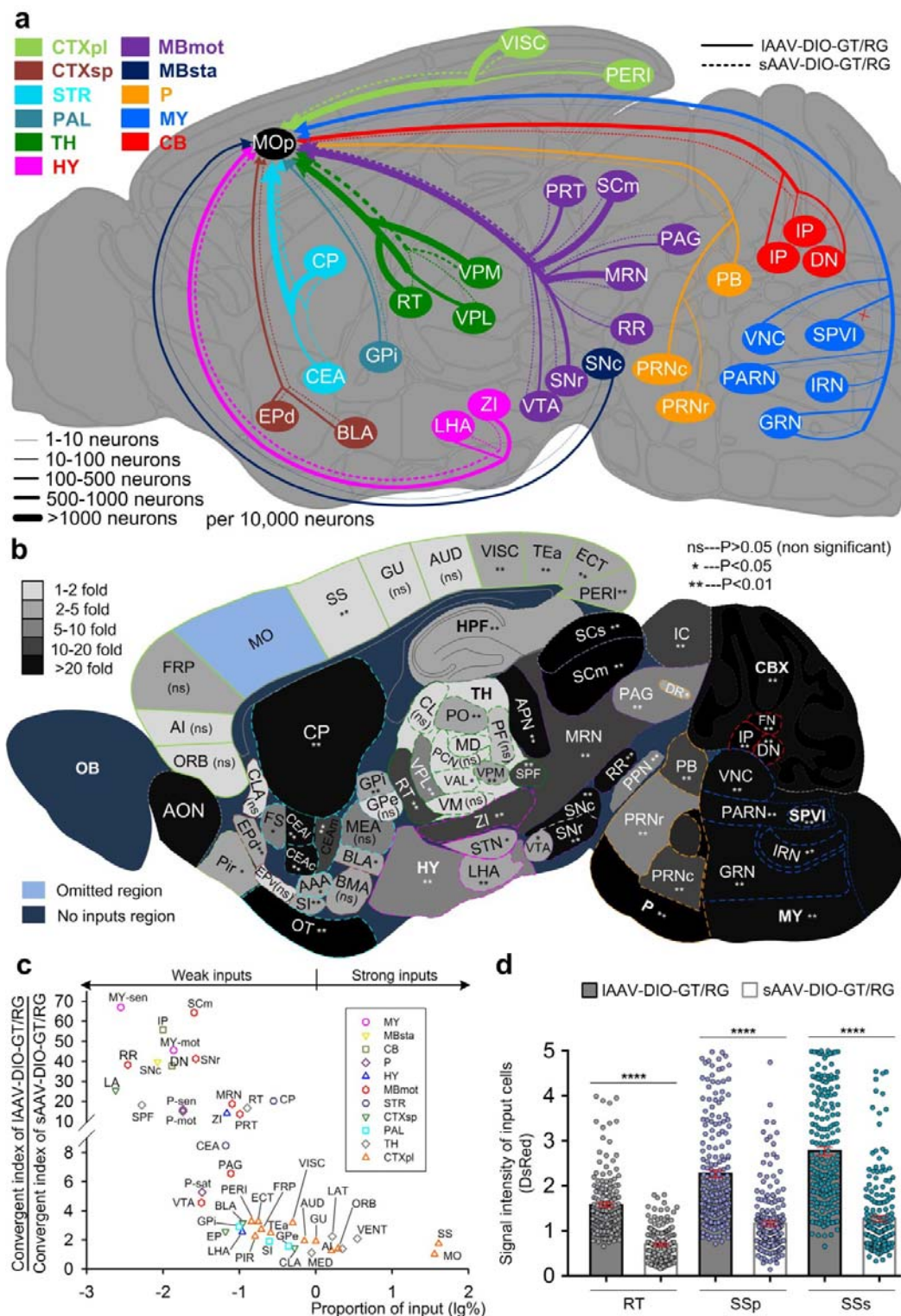
246
247
248
249

Fig. 2 | MAP-ENVIVDERS enables efficient tracing of input networks. a, Summary of representative sparsely traced input subregions with current RV-mediated trans-monosynaptic tracing systems (sAAV-DIO-GT/RG, dashed lines), which were significantly enhanced by MAP-ENVIVIDERS (lAAV-DIO-GT/RG, solid lines). The thickness of each colored lines represented the

average number of input neurons (n = 5 mice) in each subregions (per 10, 000 neurons). **b**, Summary of increased tracing efficiency in diverse brain regions with MAP-ENVIVDERS. n = 5 mice for each group. Mann-Whitney U test. n.s, non-significant (P > 0.05), *P < 0.05, **P < 0.01. **c**, Relationship between the proportion of inputs (input cells in each subregion relative to the total input cells across whole brain, which was denoted by logarithm to base 10 (lg %, x-axis) and the enhanced ratios provided by MAP-ENVIVIDERS (the ratio between convergent index of lAAV-DIO-GT/RG and convergent index of sAAV-DIO-GT/RG, y-axis). n = 5 mice for each group. **d**, Signal intensities of input neurons in reticular nucleus of the thalamus (RT), primary somatosensory area (SSp), and supplemental somatosensory area (SSs) labeled by lAAV-DIO-GT/RG-RV or sAAV-DIO-GT/RG-RV. n = 160 neurons for RT, n = 190 neurons for SSp and SSs, n = 3 mice for each group. two-tailed t-test ****P < 0.0001. All data are presented as mean ± s.e.m. Abbreviations: see **Supplementary Table 2**.

Demonstration of MAP-ENVIVIDERS for reliable, density-controllable super-bright neuronal labeling

Dissection of neurocircuits on individual neuron level is critical for understanding neuronal structure-function relationship and cell-type classification[11]. In previous studies, dual rAAV-based Cre-lox/Flp-FRT recombinase systems and the tTA/TRE transactivation system have been successfully developed to label limited or tunable numbers of neurons of specific cell types[13,20,21]. However, a viral copackaging strategy has never been explored in these systems. Therefore, we next explored whether MAP-ENVIVIDERS could improve the labeling brightness for mapping projectomes of individual neurons. We first validated MAP-ENVIVIDERS in wild-type mice with copackaging a Cre-expressing vector and a Cre-dependent vector (**Fig. 3a**). We generated three littermate rAAVs (abbreviated for lAAVs hereafter) with a CMV promoter-mediated Cre-expressing vector (AAV-CMV-Cre) and a Cre-inducible, double-floxed EYFP element (AAV-double floxed-EYFP)[34] at ratios of 1:20,000 (lAAV^{20,000}), 1:200,000 (lAAV^{200,000}) and 1:1,000,000 (lAAV^{1,000,000}). We found that these three lAAVs produced different labeling densities, but with similar brightness in the soma and long-range axonal projections when injected into MOp (**Fig. 3b** and **Supplementary Fig. 6**). The labeled somas were well separated, and the fine structures, including various types of spines[35] and boutons on local and long-range projecting arborizations[15], could be clearly visualized and identified (**Supplementary Fig. 5**).

To compare the differences in labeling efficiency and brightness between lAAVs and mixtures of independently packaged rAAVs (sAAVs), we performed parallel

285 experiments with mixtures of Cre-expressing rAAV and Cre-dependent rAAVs at
286 ratios of 1:20,000, 1:40,000, 1:80,000 and 1:1,000,000 based on previous methods[12]
287 (abbreviated for sAAV^{20,000}, sAAV^{40,000}, sAAV^{80,000} and sAAV^{1,000,000}, see Methods).
288 We selected Thy1-EYFP-H mice[36], one of widely used transgenic lines as reference.
289 Although density-controllable labeling could be achieved in both lAAVs and sAAVs-
290 based systems, labeling by lAAVs was significantly brighter and more efficient under
291 the same experimental conditions (**Fig. 3c** and **d**, left panel). Specifically, the
292 brightness of sparsely labeled neurons by lAAVs (**Supplementary Fig. 1c,d**) was
293 equivalent to Thy1-EYFP-H mice, but ~3 times stronger for lAAV^{200,000} compared
294 with sAAV^{20,000} and ~7 times for lAAV^{1,000,000} compared with sAAV^{1,000,000},
295 respectively (P < 0.001), demonstrating the sensitivity of MAP-ENVIVIDERS (**Fig.**
296 **3d**, right panel and **Supplementary Fig. 7**). In accordance with previous study[31], the
297 Cre titers of lAAVs and sAVVs were similar as measured by quantitative polymerase
298 chain reaction, however, the number of labeled neurons for lAAV^{20,000} was nearly 4-
299 fold that of sAAV^{20,000}, demonstrating the efficiency of MAP-ENVIVIDERS (**Fig. 3c**
300 and **Supplementary Table 3**). Similar results were also obtained in other brain
301 regions, such as CA1 and CA3, where the labeled neurons were significantly brighter
302 than those in the Thy1-EYFP-H mouse line (**Fig. 3e**, left and right panel;
303 **Supplementary Fig. 8**). However, the number of neurons labeled differed among the
304 brain regions for the same lAAV preparation (**Fig. 3e**, middle panel). These results
305 collectively showed that the MAP-ENVIVIDERS labeling strategy is significantly
306 more sensitive, efficient and reproducible than methods using mixtures of
307 independently packaged rAAVs for density-controllable neuron labeling.
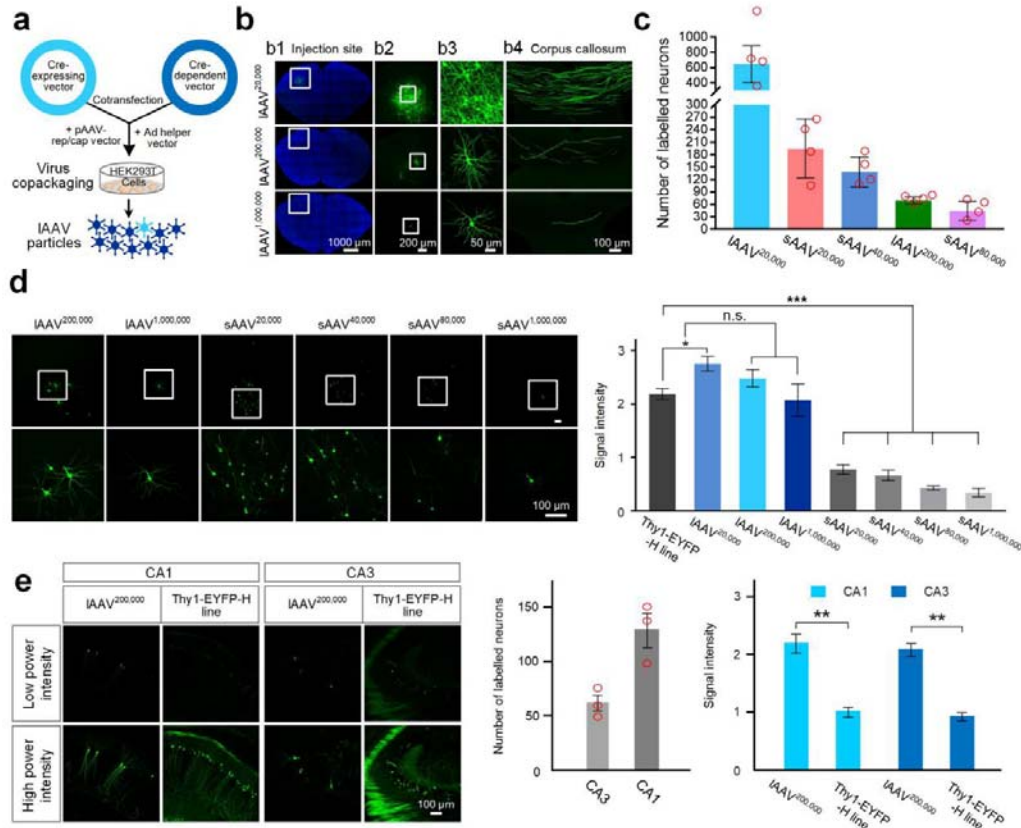
Fig. 3 | MAP-ENVIVIDERS enables density-controllable, super-bright neuron labeling in wild-type mice. a, Schematic for the production of lAAVs. Briefly, a Cre-expressing vector and a Cre-expressing vector were mixed at preset ratios on cellular level, generating lAAV particles. **b**, Representative confocal images of neurons from mice injected with 100 nl of lAAVs produced by copackaging pAAV-CMV-Cre and pAAV-EF1α-double floxed-EYFP at the indicated ratios. Images show neurons at the injection sites (**b1-b3**) and their long axonal projections in the corpus callosum (**b4**). **c**, Quantification of neurons labeled by different lAAVs and sAAVs (n = 4 mice each). **d,** Comparison of brightness between neurons labeled by different lAAVs and sAAVs. Upper panel: confocal images; lower panel: quantifications of signal intensities of the labeled somas. Neurons from the Thy1-EYFP-H mouse line were used as a reference (n = 40 cells for the Thy1-EYFP-H mouse line; n = 40 cells for lAAV^{20,000}, lAAV^{200,000}, sAAV^{20,000}, sAAV^{40,000}, and sAAV^{80,000} from 3 mice; n = 20 cells for lAAV^{1,000,000} and n = 17 cells for sAAV^{1,000,000}, from 4 mice). One-way ANOVA with Dunnett's post hoc test. **e**, Applications of lAAV^{200,000} in CA1 and CA3. Comparisons of brightness of lAAV^{200,000}-labeled neurons in CA1 and CA3 (n = 40 cells for each from 3 mice) with Thy1-EYFP-H mouse line (n = 40 cells) were shown with confocal images (left panel) and measurement of signal intensities (right panel) (n = 40 cells for each from 3 mice). Two-tailed t-test. Middle panel, quantifications of labeled neurons in CA1 and CA3 (n = 3 mice each). All data are presented as the mean ± s.e.m. n.s, non-significant (P > 0.05), *P < 0.05, **P < 0.01, ***P < 0.001. Abbreviations: see **Supplementary Table 2.**
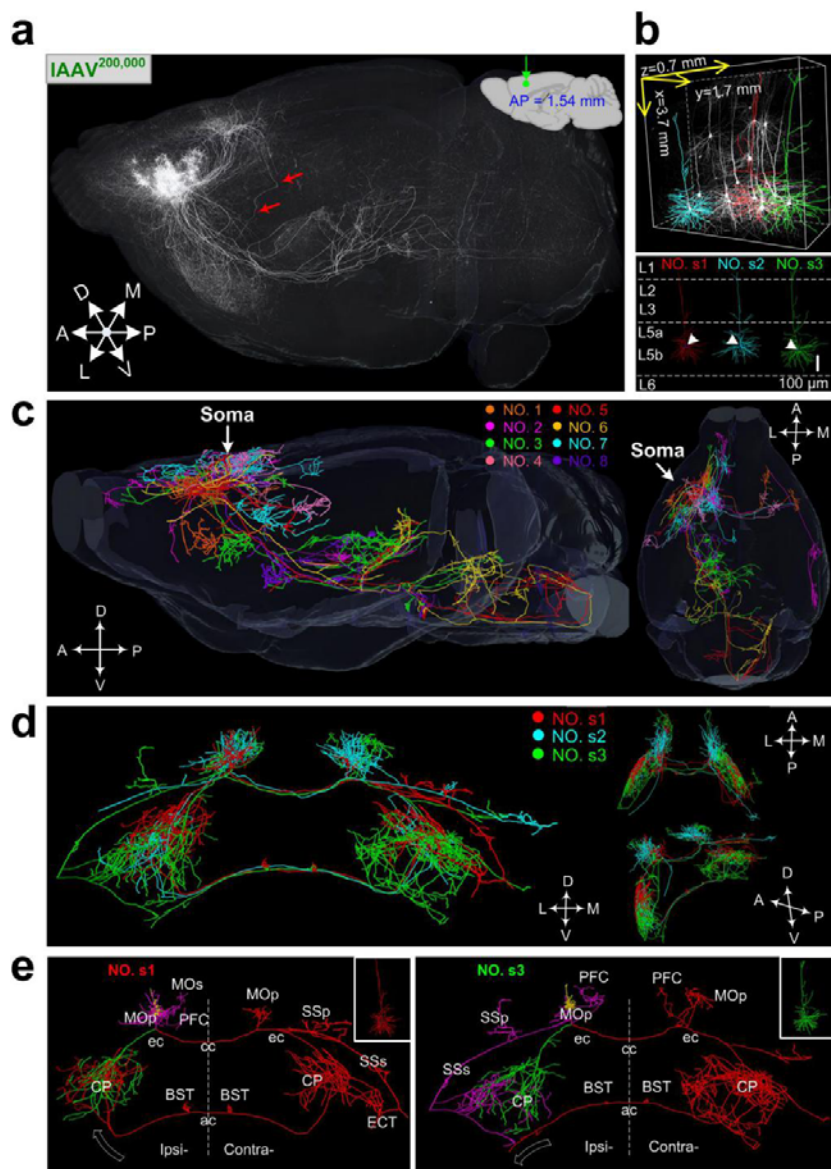
328 **MAP-ENVIVIDERS enables identification of novel type of neurons**

329 To further explore the potential of MAP-ENVIVIDERS in obtaining brain-wide long-

330 range projections, we used fluorescence micro-optical sectioning tomography

331 (TDI-fMOST)[37] to automatically image the brain sample injected with lAAV[200,000] in

332 the MOp of wild-type mouse. Imaging was conducted with a voxel size of $0.176 \times$

333 0.176×1 μm^3, generating 12,841 continuous coronal section across the whole brain

334 (**Fig. 4a** and **Supplementary Fig. 9**). Among the 11 reconstructed MOp pyramidal

335 neurons, four intratelencephalic neurons located in L2, L3, and L6a projected to the

336 ipsi- and contralateral striatum and cortex, and four pyramidal tract neurons located in

337 L5b projected to diverse subcortical brain regions, as previously reported[38-42] (**Fig. 4c**;

338 **Supplementary Fig. 10a,b** and **Supplementary Video 1**). Interestingly, the

339 remaining three neurons (No. **s1**-**s3**) formed a novel type of pyramidal neuron located

340 in L5b (**Fig. 4b** and **Supplementary Fig. 10c**). We termed these "boomerang neurons"

341 because they send a collateral axonal branch to the contralateral MOp and dorsal

342 caudoputamen (CP) via the corpus callosum, which then returns to the ipsilateral side

343 via the anterior commissure, innervating the ipsilateral CP region via a collateral on

344 the ipsilateral side, thus forming a symmetrical track (**Fig. 4d,e**; **Supplementary Fig.**

345 **10d** and **Supplementary Video 2-4**). All of these reconstructed boomerang neurons

346 had complex axonal projections, with over axonal 1,200 branches totaled at ~22 cm

347 long on average (**Supplementary Fig. 14**). Therefore, the use of MAP-ENVIVIDERS

348 together with TDI-fMOST allowed us to document the projectome of individual

349 neurons in great detail as well as to identify novel type of neurons.

350

Fig. 4 | MAP-ENVIVIDERS enables identification of a novel type of neuron in MOp. a, Sagittal view showing lAAV^{200,000}-labeled MOp whole-brain dataset. The red arrows indicate axon pathway of boomerang neurons. **b**, Raw signals (top) and reconstructed dendritic morphologies (bottom) of three boomerang neurons (No. **s1-s3**). **c**, Summary of axonal morphologies of the eight reconstructed pyramidal neurons (**No. 1-8**) in sagittal (left panel) and horizontal (right panel) views. **d**, Coronal (left), horizontal (upper right), and sagittal (with a rotated angle, lower right) views showing axonal morphologies of three boomerang neurons. **e**, Localization of the brain-wide axonal projections of neurons **s1** and **s3** (dendrites: yellow; local axons: magenta; the left and right branches originating from the ipsilateral external capsule are shown in green and red, respectively). Dashed white arrows indicate the termination directions of the main axons. Abbreviations: see **Supplementary Table 2.**

MAP-ENVIVIDERS enables unbiased, cell-type-specific, sparse and super-bright labeling among diverse transgenic mice

Cell-type-specific labeling is crucial for dissecting the functional role and circuitry of a given type of cell[21]. To demonstrate the potential of MAP-ENVIVIDERS for efficient cell-type-specific and density-controllable labeling with multiple Cre-driver lines, we next redesigned MAP-ENVIVIDERS with an Flp-expressing vector (e.g., AAV-EF1α-Flp) and an both Flp- and Cre-dependent vector (e.g., AAV-hSyn Con/Fon EYFP[43]) and copackaged two vectors at different ratios to generate cslAAV^{2,000} and cslAAV^{20,000} (cs refers to cell-type-specific hereafter, **Fig. 5a**). For validations, we injected the resulted two cslAAVs into MOp of Thy1-Cre transgenic mice and found that tunable neuron labeling was achieved with different ratios (**Supplementary Fig. 11a,b**), indicating the functionality of MAP-ENVIVIDERS with Cre-driver transgenic lines.

To achieve cell-type-specific sparse and super-bright labeling of cholinergic neurons, we next applied one of cslAAVs, cslAAV^{20,000} into the basal forebrain (BF) of choline acetyltransferase (ChAT)-Cre transgenic mice[23] (**Fig. 5b**). Among 54 ± 4 well-separated neurons labeled with cslAAV^{20,000} (n = 4 mice), $97.6 \pm 1.6\%$ of which were ChAT positive (**Fig. 5c**, **Supplementary Fig. 12** and **Supplementary Table 3**). Fine structures of these sparsely neurons, both near and far from the somas, could be visualized clearly (**Fig. 5d-h**) and their fine long-range projections covered diverse brain regions as previously reported[44] (**Supplementary Fig. 13**). Parallel experiments with wild-type mice did not label any cells (n = 4 mice; **Supplementary Fig. 11c**), confirming the cell-type specificity of the method. In another set of parallel experiments in which cssAAV^{2,000} and cssAAV^{20,000}, mixtures of the corresponding independently packaged rAAVs (see Methods) were injected into BF of ChAT-Cre transgenic mice. We found that no neurons were labeled with cssAAV^{20,000} and only a few faintly labeled with cssAAV^{2,000} (n = 5 mice each; **Supplementary Fig. 11d,e**). These results demonstrated that the MAP-ENVIVIDERS strategy was significantly more sensitive and efficient for cell-type-specific neuron labeling.

The strength and abundance of Cre recombinase varied greatly among diverse Cre-driver transgenic lines[22,23]. To examine the labeling efficiencies in different Cre-driver mice, we measured the fluorescent intensity of individual neurons labeled by

395 cslAAVs with different labeling densities in three Cre-driver lines under the control of

396 different promoters, including Thy1 promoter (Thy1-Cre), dopamine

397 transporter promoter (DAT-Cre)[45] and choline acetyltransferase promoter (ChAT-Cre)

398 (**Supplementary Fig. 1c** and **Supplementary Table 3**). We found that averaged

399 fluorescent intensity of individual neurons in showed no apparent difference among

400 these three different types of Cre-driver transgenic mice (**Fig. 5i,j**). These results

401 showed that the MAP-ENVIVIDERS labeling strategy enables unbiased, cell-type-

402 specific, sparse and super-bright labeling among diverse transgenic mice.
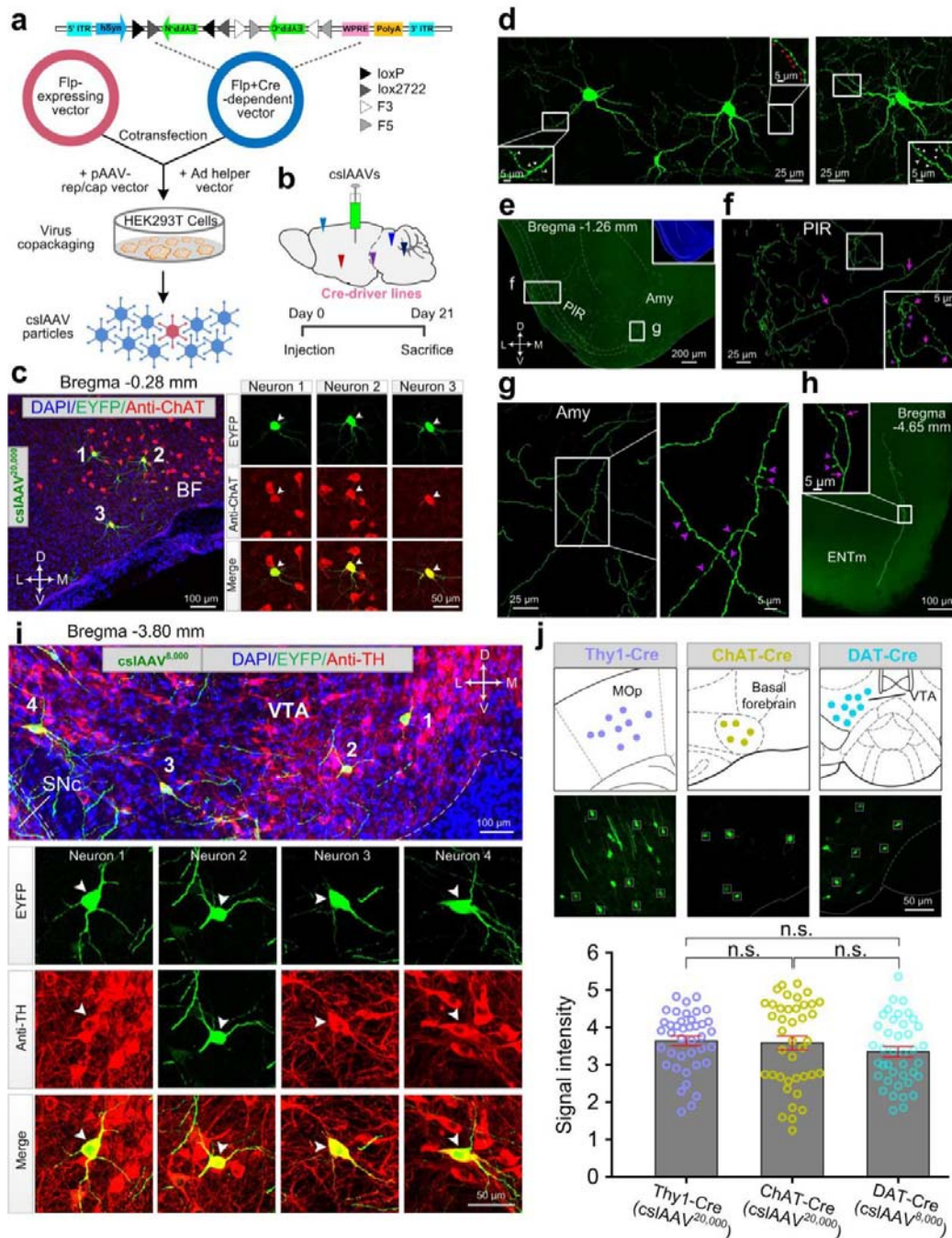
Fig. 5 | MAP-ENVIVIDERS enables unbiased, cell-type-specific, sparse and super-bright labeling among diverse transgenic mice. a, Schematic showing the generation of cslAAVs and the Cre- and Flp-dependent AAV vector. ITR, inverted terminal repeat; hSyn, human synapsin promoter; WPRE, woodchuck hepatitis virus post transcriptional regulatory element. **b**, Schematic of the experiment for the data in **c-i**. **c**, Low-magnification (left) and high-magnification (right) images showing colocalization of three cssAAV^{20,000}-labeled basal forebrain cholinergic neurons (neurons 1 to 3, green) with anti-choline acetyltransferase (ChAT) antibody staining (red). **d**, Fine structure of three cholinergic neurons in **c**. Insets are enlargements of the corresponding boxes, white arrowheads

412
413 indicate spines, and red arrowheads indicate boutons. **e-h**, Representative images showing long-range
414 axonal projections in the piriform area (PIR, **f**), amygdala (Amy, **g**), and entorhinal area, medial part,
415 dorsal zone (ENTm, **h**). **i**, low-magnification (upper panel) and high-magnification (lower panel)
416 images showing immunostaing of four cssAAV^{8,000}-labeled dopaminergic neurons (neurons 1 to 4,
417 green) in ventral tegmental area (VTA). Anti-tyrosine hydroxylase (TH) antibody staining, the
418 definitive marker for dopaminergic neurons, were shown in red. **j**, pper panel, schematic for
419 measurement (upper panel) and comparisons (lower panel) of signal intensities of individual neurons
420 labeled by different cslAAVs in multiple Cre-driver transgenic lines, including cssAAV^{20,000}-labeled
421 Thy1-Cre mice, cssAAV^{20,000}-labeled ChAT-Cre mice and cssAAV^{8,000}-labeled DAT-Cre mice. (n = 40
422 cells from 3 mice for each). One-way ANOVA with Turkey's post hoc test. All data are presented as
423 the mean ± s.e.m. n.s, non-significant ($P > 0.05$). Abbreviations: see **Supplementary Table 2.**

424 **MAP-ENVIVIDERS enables identifying presynapses of individual cell-type-**
425 **specific neurons**.

426 To reveal fine morphologies of individual cholinergic neurons, we also performed
427 whole-brain mapping of BF-injected brains of ChAT-Cre mice (**Fig. 6a**). Based on
428 cell-type-specific, sparse but super-bright labeling, four cholinergic neurons we
429 reconstructed showed distinctive projectomes but all shared with extremely complex
430 axonal aborizations, with an average of 4,059 axonal branches (**Fig. 6b**;
431 **Supplementary Fig. 14** and **Supplementary Video 5**). Remarkably, we obtained an
432 individual cholinergic neuron (No. **c2**) containing incredible ~9,500 axonal branches,
433 which were nearly 9-times more than previously reconstructed individual cholinergic
434 neuron by the combination of drug and transgenic mice strategy[46]. Particularly, this
435 neuron contained two major axonal branches with one of them send massive
436 arborizations dominating layer 2 to layer 4 of the ipsilateral anterolateral/lateral visual
437 area (VISal/l, ~7,840 axonal branches), a critical region for visual processing[47], and
438 the other terminated in ipsilateral subiculum (SUB) (**Fig. 6e**,**f** and **Supplementary**
439 **Video 6**). Projections of cholinergic neurons to hippocampus have long been known
440 as a key player in the formation of learning and memory[48]. To this end, we
441 reconstructed two BF cholinergic neurons (No. **c3** and No. **c4**) which send projections
442 covering entire hippocampus (-1.0 to -3.8 mm from the bregma; **Fig. 6c**). Specifically,
443 the former (No. **c3**) exhibited a point to point projection mode with sole projections to
444 contralateral dorsal and ventral hippocampal region (HIP) from BF, whereas the latter
445 (No. **c4**) projected to several cortical regions successively, including ipsilateral
446 anterior piriform area, prefrontal cortex, motor areas and somatosensory areas and

447   finally terminated in ipsilateral hippocampus with massive massive arborizations in

448   ventral HIP followed by less axonal branches in dorsal HIP and a single axonal

449   branch regulating both ipsilateral and contralateral dorsal HIP (**Fig. 6b,c**). Similar to

450   No. **c3**, the fourth neuron (No. **c4**) also exhibited a point to point projection mode

451   with projections from BF to ipsilateral CP (BF→CP) in a fanwise manner (-1.1 to -2.1

452   mm from the bregma; **Fig. 6d**). These results demonstrate that the MAP-

453   ENVIVIDERS could capture morphological details of individual neurons with cell-

454   type specificity to a great extent.

455   Plasticity of presynaptic axonal boutons served as key elements for the

456   maintenance of neural circuit functions and loss of bouton density has been associated

457   with several neurodegenerative disorders[49,50]. To assess the total number of individual

458   cholinergic neurons, we randomly selected ten regions of interest (ROIs) from raw

459   signal of each cholinergic neuron and counted the boutons along the axon shafts

460   manually (lower right panel in **Fig. 6d** and **Supplementary Fig. 15**; also see

461   methods). The averaged bouton density (defined as bouton numbers over axonal

462   length) of four cholinergic neurons was estimated to be 0.303 ± 0.016 bouton/μm (No.

463   **c1**: 0.320 ± 0.016 bouton/μm; No. **c2**: 0.302 ± 0.020 bouton/μm; No. **c3**: $0.279 \pm$

464   0.011 bouton/μm; No. **c4**: 0.312 ± 0.015 bouton/μm; n = 10 ROIs for each neuron; left

465   panel in **Fig. 6g** and **Supplementary Table 4**). Based on these results, we thus

466   estimated that averaged total number of four cholinergic neurons was $98,496 \pm 5,230$

467   (No. **c1**: $64,295 \pm 3,174$; No. **c2**: $147,858 \pm 9,668$; No. **c3**: $56,592 \pm 2,151$; No. **c4**:

468    $125,138 \pm 5,928$; right panel in **Fig. 6g** and **Supplementary Table 3**), which (to the

469   best of our knowledge) has not been reported previously. Such huge number of

470   boutons obtained by MAP-ENVIVIDERS indicated that an individual cholinergic

471   neuron enjoyed a wide range of modulation coverage.

472
473
474
475
476
477
478
479
480
481
482
483
484
485
486
487
488
489
490
491
492
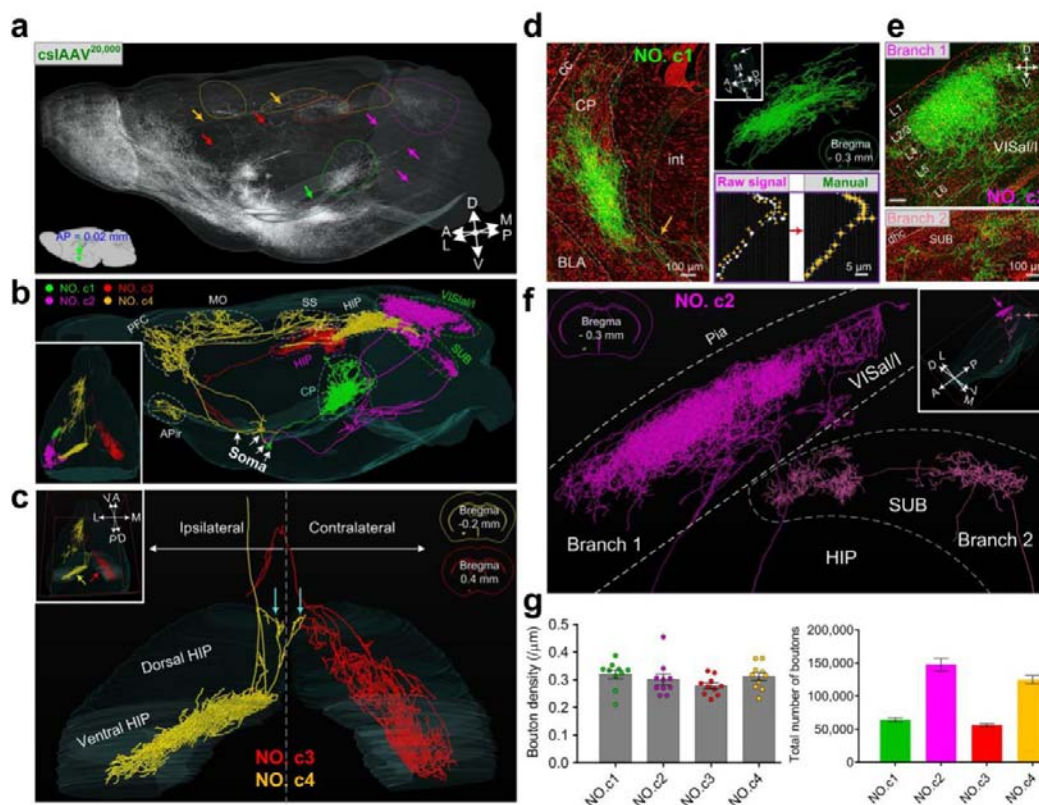
Fig. 6 | MAP-ENVIVIDERS enables identification of presynapses of individual cell-type-specific neurons. a, Sagittal view showing whole-brain labeling after injection of cslAAV[20,000] into the basal forebrain. Arrows indicate the main axons and colored circles indicate the terminal arborizations of each reconstructed neuron. **j,** Summary of the axonal morphologies of four reconstructed cholinergic neurons (**No. c1-c4**) in sagittal and the horizontal view (insets). **c,** Three dimensional view showing terminal arborizations (indicated by arrows in upper left insets) in dorsal and ventral hippocampal region (HIP) of two cholinergic neurons (**No. c3**: red; **No. c4**: yellow). Cyan arrows indicated a single axonal branch of **No. c4** with concomitant regulation of both ipsilateral and contralateral dorsal HIP. **d,** Left panel, raw signal with propidium iodide (PI)-stained cytoarchitecture reference of neurons c1 (green: maximum intensity projection of 1,000 coronal sections; Red: 5 µm thickness). Yellow arrow indicated the main axon. Upper right panel: reconstructions of complex axonal arborizations in CP. Lower right panel: enlargements of box region in upper left panel demonstrating schematic for manual bouton counting in **g**. **e,** Raw signal with PI-stained cytoarchitecture reference showing complex axonal arborizations in the anterolateral/lateral visual area (VISal/l; branch 1; upper) and subiculum (SUB; branch 2; lower) of neurons **c2**. Branch 1 and branch 2 were maximum intensity projection of 1,800 and 400 coronal sections (green signal), respectively. Red signals were 5 µm thickness for both. **f,** Reconstructions of branch 1 and branch 2 in **e**. Brain outlines in **c,d,f** depicted approximate somal locations of respective neurons. **g,** Averaged bouton density (left panel, n = 10 ROIs for each neuron) and estimated total number of boutons (right panel) of four reconstructed cholinergic neurons. Each circle represents one ROI. Abbreviations: see Supplementary Table 2.

Copackaging of rAAVs significantly reduces their mutual suppression

493

494 Since we demonstrated that MAP-ENVIVIDERS significantly improved the tracing
495 efficiencies of input networks as well as enhanced the labeling brightness of output
496 networks, we next made initial attempts to investigate probable mechanisms for the
497 powerfulness of this viral copackaging-based labeling strategy. Previous studies have
498 indicated that the interactions among different viral vectors, such as AAV over herpes
499 simplex virus[24], AAV over adenovirus[25], or even among the same types of viruses
500 (e.g., herpes simplex virus and pseudorabies virus)[26-28], can severely affect their gene
501 expressions. We next evaluated the degree of interaction between two different
502 rAAVs. To eliminate the effects of other factors, we used two independently
503 packaged, highly similar rAAVs, which were same serotyped (rAAV2/9) under the
504 control of the same ubiquitous promoter (EF1α) but only expressing different
505 fluorescent proteins (EYFP or mCherry). We injected equal ratio mixture of two
506 rAAVs (abbreviated for sAAV-EYFP/mCherry for convenience, s refers to stranger
507 hereafter) into the MOp of wild-type mice. For the controls, a parallel procedure was
508 followed but with rAAV2/9-EYFP or rAAV2/9-mCherry mixed equally with
509 phosphate-buffered saline (PBS). The fluorescence intensity was significantly lower
510 for both EYFP and mCherry when the vectors were used in combination than when
511 used separately (**Fig. 7a**,**b**), by a factor of 2.4 for EYFP and 1.4 for mCherry (**Fig. 7c**),
512 demonstrating significant mutual suppression among different rAAVs.

513 Previous studies have employed viral copackaging strategy for cost- and time-
514 effective AAV manufacturing[29,30]. We next examined whether viral copackaging
515 strategy could increase homogeneity over independently packaged rAAVs. To
516 achieve this, we copackaged the two corresponding plasmids at a 1:1 ratio and then
517 injected the resulting rAAVs (abbreviated as lAAV-EYFP/mCherry, where l refers to
518 littermate hereafter) into MOp as described above. Equivalent expressions of EYFP
519 and mCherry within individual cells were observed more frequently in neurons co-
520 infected by lAAV-EYFP/mCherry than in neurons coinfected by sAAV-
521 EYFP/mCherry, which instead tended to produce unbalanced expression of EYFP and
522 mCherry (**Fig. 7d**,**e**, top vs. bottom rows). For neurons with unbalanced expressions
523 (arrows in **Fig. 7e**), The ratio of mCherry/EYFP and EYFP/mCherry fluorescence
524 intensity with higher mCherry and EYFP signals, respectively, was significantly
525 higher in neurons injected with sAAV-EYFP/mCherry than in those injected with

526   lAAV-EYFP/mCherry (mCherry/EYFP ratio (pink arrows): 3.44 ± 0.76 vs. 1.46 ±

527   0.20, respectively, and EYFP/mCherry ratio (cyan arrows): 2.50 ± 0.37 vs. 1.48 ±

528   0.12, respectively; mean ± s.e.m, unpaired t-test, P < 0.0001, n = 3 mice, **Fig. 7f**).

529   These results indicated that copackaging rAAVs can substantially reduce mutual

530   suppression and significantly enhance compatibility among different rAAVs.
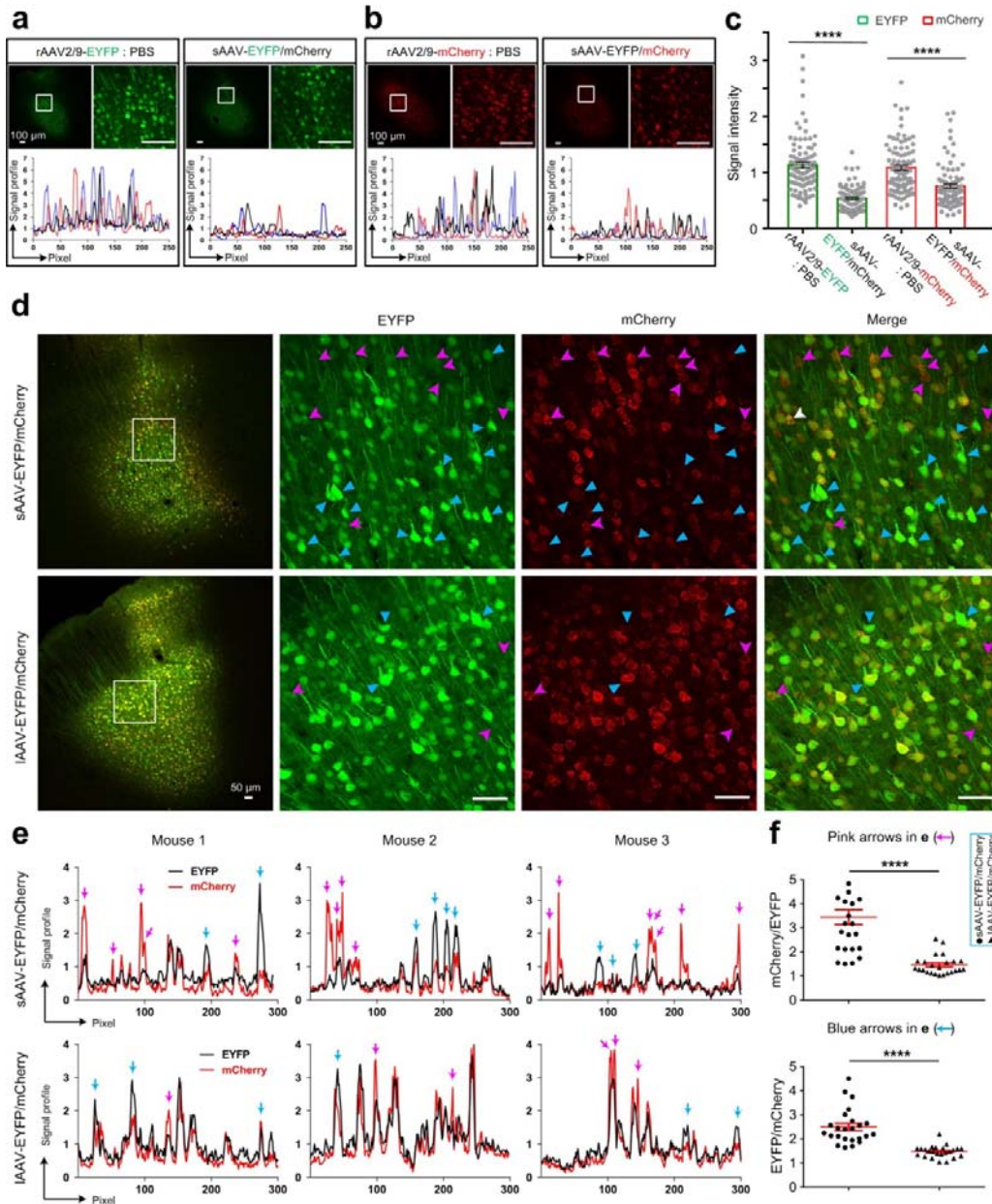
531

532   **Fig. 7 | Viral copackaging reduces rAAV suppression. a-b**, Representative confocal images and

533   signal profiles of EYFP and mCherry in neurons of the MOp of wild-type mice injected with 100nl 1:1

534   mixtures of rAAV2/9-EYFP : PBS, rAAV2/9-mCherry : PBS and rAAV2/9-EYFP : rAAV2/9-

535   mCherry (sAAV-EFYP/mCherry). **c**, Fluorescence intensity quantified in 90 neurons (n = 3 animals)

536 from **a** and **b**. **d**, Representative confocal images showing expression of EYFP and mCherry in neurons
537 of MOp of wild-type mice injected with 100nl sAAV-EFYP/mCherry (upper panel) or lAAV-
538 EFYP/mCherry (lower panel). Pink and cyan arrowheads indicate neurons with higher EYFP and
539 mCherry signals, respectively. **e**, Representative signal profiles of mCherry and EYFP in three mice
540 injected with sAAV-EFYP/mCherry (upper panel) or lAAV-EFYP/mCherry (lower panel). Pink and
541 cyan arrows indicate neurons with higher EYFP and mCherry signals, respectively. **f**, Ratio of
542 mCherry/EYFP (pink arrows) and EYFP/mCherry (cyan arrows) fluorescence intensity in **e**. All data
543 are presented as the mean ± s.e.m., n = 3 animals for each group in **a-f**. Two-tailed t-test, ****$P <$
544 0.0001.

545
546

DISCUSSION

547 In the present study, we developed MAP-ENVIVIDERS and generated series of
548 vector mixing-based rAAV cocktail providing more efficient cell-type-specific
549 whole-brain input mapping and improved super-bright and sparse labeling for certain
550 types of neurons. We then found that strong mutual suppression existed among
551 independently packaged rAAVs and copackaging of rAAV-producing plasmids
552 enhanced co-expression of genes among multiple rAAVs.

553 Based on our results, we concluded that MAP-ENVIVIDERS were more
554 prominent in complicated systems requiring co-expression of multiple rAAVs
555 compared with previous strategy achieved by co-injections or co-administrations of
556 several seperately packaged rAAVs. For non-cell-type-specific super-bright and
557 sparse labeling (co-expression of Cre and Cre-dependent fluorescent protein), MAP-
558 ENVIVIDERS provided ~3-fold more labeled neurons and ~5-fold more bright
559 fluorescent intensity (**Fig. 3c,d**). For cell-type-specific super-bright and sparse
560 labeling (co-expression of Flp, Cre and Flp-/Cre-dependent fluorescent protein),
561 MAP-ENVIVIDERS provided more than 10-fold increase of labeling efficiency (**Fig.**
562 **5c** and **Supplementary Fig. 11d,e**). Thus, MAP-ENVIVIDERS could achieve the
563 same efficiency with much lower dose of virus, which may reduce cytotoxicity and
564 experimental cost. Notably, since MAP-ENVIVIDERS is very sensitive, careful
565 consideration of mixing ratios for viral copackaging was needed to label desired
566 number of neurons. For cell-type-specific super-bright/sparse labeling, the strength
567 and abundance of Cre recombinase varies greatly among different cell types and brain

568 regions[22,23], thus the mixing ratio of Flp and Flp-/Cre-dependent fluorescent protein

569 need to be carefully tested.

570   Moreover, when MAP-ENVIVIDERS was applied for circuit tracing which

571 involves not only compatibility two different rAAVs but coherence between two

572 labeling systems (i.e., rAAVs-RV combination), labeling efficiency was dramatically

573 increased (10- to 70-fold) for 40% of the input brain regions, which were sparsely

574 labeled by previous strategies (**Fig. 1**,**2**). The much stronger DsRed signals and the

575 larger number of total input neurons suggested that more RVs may be produced with

576 the MAP-ENVIVIDERS strategy. This is probably due to the reduction of mutual

577 suppression between the rAAVs expressing TVA and RG. The AAVs in the starter

578 cells expressed more TVA and RG, leading to more entry and assemble of infectious

579 RVs and eventually higher transsynaptic tracing efficiency (convergent index from

580 averaged 32 to 52, **Supplementary Table 1**). Moreover, it is feasible to combine

581 MAP-ENVIVIDERS with optimized RG (oG)[10] and other RV strains (e.g., the CVS-

582 N2c$^{\Delta G}$ strain)[9] to further improve the tracing efficiency. Further efforts towards these

583 largely enhanced input neurons in diverse brain regions labeled by MAP-

584 ENVIVIDERS including identifications the components of cell types with the aid of

585 immunochemistry (homogeneous to the cell types labeled with current RV-mediated

586 trans-monosynaptic tracing systems or not) and electrophysiology- or optogenetics-

587 assisted functional studies.

588   Among diverse Cre-driver transgenic line for cell-type-specific neuronal labeling,

589 Thy1 promoters-mediated lines exhibited the most robust gene expression levels[37].

590 With MAP-ENVIVIDERS, the fluorescent intensity of sparsely labeled neurons in

591 choline acetyltransferase promoter- and dopamine transporter promoter-mediated lines

592 approaching that achieved by Thy1 promoters (**Fig. 5j**). This unbiased property for

593 cell-type-specific, sparse and super-bright labeling highlights the great sensitivity of

594 MAP-ENVIVIDERS strategy. Combined with whole-brain imaging systems, MAP-

595 ENVIVIDERS demonstrated great advantages for capturing more details of individual

596 cell-type-specific neurons (e.g. an individual cholinergic neuron with ~9,500+ axonal

597 branches and averaged 148,000 presynaptic axonal boutons) (**Fig. 6**). To obtain exact

598 number of boutons of specific individual neurons faithfully, further efforts are needed

599 including co-expressing fluorescent proteins with bouton indicative marker, such as

600 well-known synapophysin[51] along the axons, as well as developing automatic or semi-
601 automatic softwares for bouton identification[52].

602   Though further efforts are needed to explore the deeper mechanisms leading to
603 the high sensitivity and efficiency of MAP-ENVIVIDERS, our initial attempts
604 indicated that strong mutual suppression existed among different rAAVs, a
605 phenomenon similar to other kinds of viruses, such as herpes simplex virus, hepatitis
606 C virus and influenza A virus[53,54] (**Fig. 7a-c**). We further found that viral copackaging
607 strategy significantly ameliorated this suppression and enhanced compatibility of
608 multi-gene expressions in the same cells (**Fig. 7d-f**), the probable reasons for which
609 were explained as follows: (i) Previous studies have demonstrated that the purities of
610 rAAVs was a key determinant for their infection efficiency[55-57]. Viral copackaging
611 strategy will reduce the heterogeneity of impurities, including cyto-toxins, cellular
612 fragments and proteins, and culture media residues deprived from viral preparations
613 of independently packaged rAAVs, thus reduce effect of strong immune responses on
614 the state of the host cells near the injection site. (ii) Gene cassettes delivered by
615 cocktails of rAAVs with different serotypes may elicit different immune responses,
616 leading to varying reductions in gene expression[58,59], which could also be avoided by
617 viral copackaging. Thus, the amplification of signals by recombinase systems
618 combined with effects of (i) and (ii) reasonably leads to significant improvements of
619 efficiency.

620   Besides the anatomical studies, MAP-ENVIVIDERS is suitable for functional
621 studies of neural circuitry[60,61] and may even be used in other organs beyond mammal
622 brain. Furthermore, MAP-ENVIVIDERS also provides great potential to facilitate the
623 co-expression of multiple genes and reduce the harmful effects for clinical gene
624 therapy[61].

625 **References**

626 1. Watabe-Uchida, M., Zhu, L., Ogawa, S. K., Vamanrao, A. & Uchida, N. Whole-brain mapping
627 of direct inputs to midbrain dopamine neurons. *Neuron* **74**, 858–873 (2012).
628 2. Schwarz, L. A. *et al*. Viral-genetic tracing of the input-output organization of a central
629 noradrenaline circuit. *Nature* **524**, 88–92 (2015).
630 3. Miyamichi, K. *et al*. Dissecting local circuits: parvalbumin interneurons underlie broad feedback
631 control of olfactory bulb output. *Neuron* **80**, 1232–1245 (2013).

632   4. Ogawa, S. K., Cohen, J. Y., Hwang, D., Uchida, N. & Watabe-Uchida, M. Organization of
633   monosynaptic inputs to the serotonin and dopamine neuromodulatory systems. *Cell Rep.* **8**, 1105–1118
634   (2014).

635   5. Miyamichi, K. *et al.* Dissecting local circuits: parvalbumin interneurons underlie broad feedback
636   control of olfactory bulb output. *Neuron* **80**, 1232–1245 (2013).

637   6. Weissbourd, B. *et al.* Presynaptic partners of dorsal raphe serotonergic and GABAergic
638   neurons. *Neuron* **83**, 645–662 (2014).

639   7. Callaway, E. M. & Luo, L. Monosynaptic circuit tracing with glycoprotein-deleted rabies
640   viruses. *J. Neurosci.* **35**, 8979–8985 (2015).

641   8. Miyamichi, K. *et al.* Cortical representations of olfactory input by trans-synaptic tracing.
642   *Nature* **472**, 191–196 (2011).

643   9. Reardon, T. R. *et al.* Rabies virus CVS-N2c strain enhances retrograde synaptic transfer and
644   neuronal viability. *Neuron* **89**, 711–724 (2016).

645   10. Kim, E. J., Jacobs, M. W., Ito-Cole, T. & Callaway, E. M. Improved monosynaptic neural circuit
646   tracing using engineered rabies virus glycoproteins. *Cell Rep.* **15**, 692–699 (2016).

647   11. Winnubst, J. *et al.* Reconstruction of 1,000 projection neurons reveals new cell types and
648   organization of long-range connectivity in the mouse brain. *Cell* **179**, 268–281 (2019).

649   12. Economo, M. N. *et al.* A platform for brain-wide imaging and reconstruction of individual
650   neurons. *eLife* **5**, e10566 (2016).

651   13. Lin, R. *et al.* Cell-type-specific and projection-specific brain-wide reconstruction of single neurons.
652   *Nat. Methods* **15**, 1033–1036 (2018).

653   14. Ren, J. *et al.* Single-cell transcriptomes and whole-brain projections of serotonin neurons in the
654   mouse dorsal and median raphe nuclei. *eLife* **8**, e49424 (2019).

655   15. De Paola, V. *et al.* Cell type-specific structural plasticity of axonal branches and boutons in the
656   adult neocortex. *Neuron* **49**, 861–875 (2006).

657   16. Stettler, D. D., Yamahachi, H., Li, W., Denk, W. & Gilbert, C. D. Axons and synaptic boutons are
658   highly dynamic in adult visual cortex. *Neuron* **49**, 877–887 (2006).

659   17. Grillo, F. W. *et al.* A distance-dependent distribution of presynaptic boutons tunes frequency-
660   dependent dendritic integration. *Neuron* **99**, 275-282 (2018).

661   18. Grillo, F. W. *et al.* Increased axonal bouton dynamics in the aging mouse cortex. *Proc. Natl. Acad.*
662   *Sci. USA* **110**, E1514–E1523 (2013).

663   19. Fenno, L. E. *et al.* Targeting cells with single vectors using multiple-feature Boolean logic. *Nat.*
664   *Methods* **11**, 763–772 (2014).

665   20. Luo, L., Callaway, E. M. & Svoboda, K. Genetic dissection of neural circuits: a decade of
666   progress. *Neuron* **98**, 256–281 (2018).

667   21. Huang, Z. J. & Zeng, H. Genetic approaches to neural circuits in the mouse. *Annu. Rev.*
668   *Neurosci.* **36**, 183–215 (2013).

669   22. Gerfen, C. R., Paletzki, R. & Heintz, N. GENSAT BAC cre-recombinase driver lines to study the
670   functional organization of cerebral cortical and basal ganglia circuits. *Neuron* **80**, 1368–1383 (2013).

671   23. Gong, S. *et al.* Targeting Cre recombinase to specific neuron populations with bacterial

672   artificial chromosome constructs. *J. Neurosci.* **27**, 9817–9823 (2007).

673   24. Bantel-Schaal, U. & H, zur Hausen. Adeno-associated viruses inhibit SV40 DNA amplification and

674   herpes simplex virus replication in SV40-transformed hamster cells. *Virology* **164**, 64–74 (1988).

675   25. Timpe, J. M., Verrill, K. C. & Trempe, J. P. Effects of adeno-associated virus on adenovirus

676   replication and gene expression during coinfection. *J. Virol.* **80**, 7807–7815 (2006).

677   26. Criddle, A., Thornburg, T., Kochetkova, I., DePartee, M. & Taylor, M. P. gD-independent

678   superinfection exclusion of alphaherpesviruses. *J. Virol.* **90**, 4049–4058 (2016).

679   27. Kim, J. S., Enquist, L. W. & Card, J. P. Circuit-specific coinfection of neurons in the rat central

680   nervous system with two pseudorabies virus recombinants. *J. Virol.* **73**, 9521–9531 (1999).

681   28. Kobiler, O., Lipman, Y., Therkelsen, K., Daubechies, I. & Enquist, L.W. Herpesviruses carrying a

682   Brainbow cassette reveal replication and expression of limited numbers of incoming genomes. *Nat.*

683   *Commun.* **1**, 146 (2010).

684   29. Doerfler, P. A., Byrne, B. J. & Cle´ment, N. Copackaging of Multiple Adeno-Associated Viral

685   Vectors in a Single Production Step. *Hum. Gene Ther. Methods* **25**, 269–276 (2014).

686   30. Wang, Q. *et al.* Efficient production of dual recombinant adeno-associated viral vectors for

687   factor VIII delivery. *Hum Gene Ther. Methods* **25**, 261–268 (2014).

688   31. Pan, C. *et al.* Shrinkage-mediated imaging of entire organs and organisms using uDISCO. *Nat.*

689   *Methods* **13**, 859–867 (2016).
690

691   32. Zhang, S. *et al.* Organization of long-range inputs and outputs of frontal cortex for top-down

       control. *Nat. Neurosci.* **19**, 1733–1742 (2016).
692

693   33. Do, J. P. *et al.* Cell type-specific long-range connections of basal forebrain circuit. *eLife* **5**,

       e13214 (2016).

694   34. Sohal, V. S., Zhang, F., Yizhar, O. & Deisseroth, K. Parvalbumin neurons and gamma rhythms

695   enhance cortical circuit performance. *Nature* **459**, 698–702 (2009).

696   35. Holtmaat, A. & Svoboda, K. Experience-dependent structural synaptic plasticity in the

697   mammalian brain. *Nat. Rev. Neurosci.* **10**, 647–658 (2009).

698   36. Feng, G. *et al.* Imaging neuronal subsets in transgenic mice expressing multiple spectral

699   variants of GFP. *Neuron* **28**, 41–51 (2000).

700   37. Xiong, H. *et al.* Whole mouse brain fluorescence imaging at synaptic resolution (in

701   preparations).
702

703   38. Mao, T. *et al.* Long-range neuronal circuits underlying the interaction between sensory and

       motor cortex. *Neuron* **72**, 111–123 (2011).
704

705   39. Kita, T. & Kita, H. The subthalamic nucleus is one of multiple innervation sites for long-range

       corticofugal axons: a single-axon tracing study in the rat. *J. Neurosci.* **32**, 5990–5999 (2012).
706

707   40. Jeong, M. *et al.* Comparative three-dimensional connectome map of motor cortical projections

       in the mouse brain. *Sci. Rep.* **6**, 20072 (2016).
708

709   41. Shepherd, G. M. Corticostriatal connectivity and its role in disease. *Nat. Rev. Neurosci.* **14**,

       278–291 (2013).
710

711   42. Harris, K. D. & Shepherd, G. M. The neocortical circuit: themes and variations. *Nat.*

       Neurosci. **18**, 170–181 (2015).

712
713   43. Fenno, L. E., Mattis, J., Ramakrishnan, C. & Deisseroth, K. A guide to creating and testing new
714   INTRSECT constructs. *Curr. Protoc. Neurosci.* **80**, 4.39.1–4.39.24 (2017).

715   44. Li, X. *et al.* Generation of a whole-brain atlas for the cholinergic system and mesoscopic
716   projectome analysis of basal forebrain cholinergic neurons. *Proc. Natl Acad. Sci. USA* **115**, 415–420
       (2018).

717   45. Lammel, S. *et al.* Diversity of transgenic mouse models for selective targeting of midbrain
718   dopamine neurons. *Neuron* **85**, 429–438 (2015).

719
720   46. Wu, H., Williams, J., & Nathans, J. Complete morphologies of basal forebrain cholinergic neurons
721   in the mouse. *eLife* **3**, e02444 (2014).

722   47. Pinto, L. *et al.* Fast modulation of visual perception by basal forebrain cholinergic neurons. *Nat.*
723   *Neurosci.* **16**, 1857–1863 (2013).

724   48. Ballinger, E. C., Ananth, M., Talmage, D. A. & Role, L. W. Basal forebrain cholinergic circuits and
725   signaling in cognition and cognitive decline. *Neuron* **91**, 1199–1218 (2016).

726   49. Schmid, L. C. *et al.* Dysfunction of somatostatin-positive interneurons associated with memory
727   deficits in an Alzheimer's disease model. *Neuron* **92**, 114–125 (2016).

728   50. Chen, S. X., Kim, A. N., Peters, A. J. & Komiyama, T. Subtype-specific plasticity of inhibitory
729   circuits in motor cortex during motor learning. *Nat. Neurosci.* **18**, 1109–1115 (2015).

730   51. Wiedenmann, B. & Franke, W. W. Identification and localization of synaptophysin, an integral
       membrane glycoprotein of Mr 38,000 characteristic of presynaptic vesicles. *Cell* **41**, 1017–1028 (1985).

731   52. Cheng, S. *et al.* DeepBouton: Automated identification of single-neuron axonal boutons at the
732   brain-wide scale. *Front Neuroinform.* **13**, 25 (2019).

733   53. Schaller, T. *et al.* Analysis of hepatitis C virus superinfection exclusion by using novel
734   fluorochrome gene-tagged viral genomes. *J. Virol.* **81**, 4591–4603 (2007).

735   54. Huang, I. C. *et al.* Influenza A virus neuraminidase limits viral superinfection. *J. Virol.* **82**, 4834–
736   4843 (2008).

737   55. Zolotukhin, S. *et al.* Recombinant adeno-associated virus purification using novel methods
738   improves infectious titer and yield. *Gene Ther.* **6**, 973–985 (1999).

739   56. Ayuso, E. *et al.* High AAV vector purity results in serotype- and tissue-independent enhancement
740   of transduction efficiency. *Gene Ther.* **17**, 503–510 (2010).

741   57. Schnodt, M. & Buning, H. Improving the quality of adeno-associated viral vector preparations:
742   the challenge of product-related impurities. *Hum. Gene Ther. Methods* **28**, 101–108 (2017).

743   58. Kotterman, M. A., Chalberg, T. W. & Schaffer, D. V. Viral vectors for gene therapy: translational
744   and clinical outlook. *Annu. Rev. Biomed. Eng.* **17**, 63–89 (2015).

745   59. Naso, M. F., Tomkowicz, B., Perry, W. L., III, & Strohl, W. R. Adeno-associated virus (AAV) as a
746   vector for gene therapy. *BioDrugs* **31**, 317–334 (2017).

747   60. Wang, W. *et al.* A light- and calcium-gated transcription factor for imaging and manipulating
748   activated neurons. *Nat. Biotechnol.* **35**, 864–871 (2017).

749   61. Lee, D., Hyun, J. H., Jung, K., Hannan, P. & Kwon, H. B. A calcium and light-gated switch to
750   induce gene expression in activated neurons. *Nat. Biotechnol.* **35**, 858–863 (2017).

62. Kotterman, M. A. & Schaffer, D. V. Engineering adeno-associated viruses for clinical gene therapy. *Nat. Rev. Genet.* **15**, 445–451 (2014).

63. Grieger, J. C., Choi, V. W. & Samulski, R. J. Production and characterization of adeno-associated viral vectors. *Nat. Protoc.* **1**, 1412–1428 (2006).

64. Osakada, F. & Callaway, E. M. Design and generation of recombinant rabies virus vectors. *Nat. Protoc.* **8**, 1583–1601 (2013).

65. Paxinos, G. & Franklin, K. B. J. The Mouse Brain in Stereotaxic Coordinates (Academic Press, 2001).

66. Xiong, H. *et al.* Chemical reactivation of quenched fluorescent protein molecules enables resin-embedded fluorescence microimaging. *Nat. Commun.* **5**, 3992 (2014).

67. Gong, H. *et al.* High-throughput dual-colour precision imaging for brain-wide connectome with cytoarchitectonic landmarks at the cellular level. *Nat. Commun.* **7**, 12142 (2016).

METHODS

Animals. All animal experimental procedures were approved by the Institutional Animal Ethics Committee of Huazhong University of Science and Technology (HUST) and Wuhan Institute of Physics and Mathematics (WIPM). All mice used in this study were 2-month-old male mice, including C57BL/6J mice, Thy1-EYFP-H line transgenic mice (Jackson Laboratory, stock number 003782, USA), Thy1-Cre transgenic mice (Jackson Laboratory, stock number 006143, USA), ChAT-Cre transgenic mice (Jackson Laboratory, stock number 006410, USA) and DAT-Cre transgenic mice (Jackson Laboratory, stock number 006660, USA).

Virus preparations. All viruses used in this study were customized or commercially provided by BrainVTA Science and Technology Company (Wuhan, China). Three general types of viruses were used: copackaged littermate AAVs (lAAVs, l refers to littermate) for enhancing viral compatibility and coherence among different viruses, independently packaged stranger AAVs (sAAVs, s refers to stranger) as control, and genetically modified RV (EnvA-SADΔG-DsRed) for retrograde trans-monosynaptic labeling. Production of rAAVs and genetically modified RV were prepared as previously described[63,64].

Both general types of AAVs were serotype 2/9. They were used for four purposes: (i) non-cell-type-specific; (iii) cell-type-specific neuronal labeling; (iii) trans-monosynaptic labeling of the direct input network of specific type of starter cells as well as (v) verification of viral interactions, enhancing infection and exogenous gene expression efficiency.

786   For purpose (i), the plasmids were AAV-EF1α-double floxed-EYFP-WPRE-

787   HGHpA[34] (Addgene #20296, a generous gift from Dr. Karl Deisseroth, Stanford

788   University) and AAV-CMV-Cre. The littermate rAAVs were lAAV^{20,000}, lAAV^{200,000}

789   and lAAV^{1,000,000}. As controls, one of the two stranger rAAVs, rAAV2/9-CMV-Cre,

790   was initially diluted to ratios of 1:20,000, 1:40,000, 1:80,000 and 1:1,000,000 in

791   phosphate-buffered saline (PBS) before mixed equally with the other stranger rAAV,

792   rAAV2/9-EF1α-double floxed-EYFP based on previous methods[12] (the resulting

793   rAAVs were abbreviated for sAAV^{20,000}, sAAV^{40,000}, sAAV^{80,000} and sAAV^{1,000,000},

794   respectively).

795   For purpose (ii), the plasmids were AAV-hSyn Con/Fon EYFP[43] (Addgene

796   #55650, a generous gift from Dr. Karl Deisseroth, Stanford University) and AAV-

797   EF1α-Flp. The littermate rAAVs were cslAAV^{2,000}, cslAAV^{8,000} and cslAAV^{20,000} (cs

798   refers cell-type-specific). Similarly, one of the two stranger rAAVs, rAAV2/9-EF1α-

799   Flp, was diluted to ratios of 1:2,000 and 1:20,000 in PBS, followed by equal mixing

800   with the other stranger rAAV, rAAV2/9-hSyn Con/Fon EYFP (the resulting rAAVs

801   were abbreviated for cssAAV^{2,000} and cssAAV^{20,000}, respectively).

802   For purpose (iii), the plasmids were AAV-EF1α-DIO-EGFP-TVA (GT) and

803   AAV-EF1α-DIO-RG, and the littermate rAAVs, lAAV-DIO-GT/RG, had a ratio of

804   1:2. For the preparation of stranger rAAVs (sAAV-DIO-GT/RG), rAAV2/9-EF1α-

805   DIO-GT and rAAV2/9-EF1α-DIO-RG were mixed at a ratio of 1:2.

806   For purpose (v), plasmids AAV-EF1α-EYFP and AAV-EF1α-mCherry were

807   copackaged at a 1:1 ratio or independently packaged in HEK293T cells, generating

808   the corresponding littermate rAAV2/9-EF1α-EYFP/mCherry (abbreviated for lAAV-

809   EFYP/mCherry for convenience). As controls, the two stranger rAAVs, rAAV2/9-

810   EF1α-EYFP and rAAV2/9-EF1α-mCherry, were mixed at a 1:1 ratio before

811   experiments (abbreviated for sAAV-EFYP/mCherry).

812   The concentrations of the plasmids and the titers of all viruses are listed in

813   **Supplementary Table 5**.

814   **Virus injections.** All virus injection experiments were performed in Biosafety level 2

815   (BSL-2) environments. Mice were placed into a stereotaxic apparatus (#68030, RWD

816   Life Science, China) and fixed with a nose clamp and ear bars after being deeply

817   anesthetized by isoflurane. A small hole was made over the skull via a dental drill

818   following the incision of the scalp along the midline of the brain. The coordinates for

819   the injections were as follows based on *The Mouse Brain in Stereotaxic Coordinates*[65]:

820 MOp (AP: 1.54 mm; ML: -1.6 mm; DV: -1.6 mm); CA3 (AP: -1.7 mm; ML: -2.0 mm;

821 DV: -2.0 mm); CA1 (AP: -1.7 mm; ML: -1.0 mm; DV: -1.5 mm); basal forebrain: (AP:

822 0.21 mm; ML: -1.5 mm; DV: -5.5 mm) and VTA (AP: -3.4 mm; ML: -1.6 mm; DV: -

823 1.6 mm).

824 For comparisons of transsynaptic spreading efficiency (**Figs. 1**,**2** and

825 **Supplementary Figs. 2-4**), the procedures for MAP-ENVIVIDERS and the classical

826 rAAV-RV systems were similar to the reported[32,33], with injected volume as 80 nl for

827 both lAAV-DIO-GT/RG and sAAV-DIO-GT/RG. Three weeks later, 150 nl EnvA-

828 SADΔG-DsRed was injected into the same site of Thy1-Cre transgenic mice.

829 For non-cell-type-specific and cell-type-specific neuronal labeling, 100 nl

830 littermate rAAVs (lAAVs and cslAAVs) and stranger rAAVs (sAAVs and cssAAVs)

831 were injected for C57BL/6J mice (**Fig. 3**,**4** and **Supplementary Figs. 5-10**,**11c**,**14**)

832 and Cre-driver transgenic lines (**Fig. 5**,**6** and **Supplementary Figs. 11a**,**b**,**d**,**e**,**12-15**).

833 For comparisons of sAAV-EFYP/mCherry with pure rAAVs (**Fig. 7a-c**) and

834 sAAV-EFYP/mCherry with lAAV-EFYP/mCherry (**Fig. 7d-f**), similar titers of sAAV-

835 EFYP/mCherry, rAAV2/9-EF1α-EYFP/PBS mixture (ratio of 1:1) and rAAV2/9-

836 EF1α-mCherry/PBS mixture with a volume of 100 nl were injected into the MOp of

837 C57BL/6J mice.

838 All virus solutions used were injected with a pulled glass micropipette at a rate of

839 20 nl/ min. The micropipette remained in place for at least 5 min before withdrawal

840 from the brain. After recovery, the mice were housed carefully until perfusion.

841 **Perfusion and slicing.** Three weeks after AAV injections and nine days after rabies

842 virus injections, mice were perfused transcardially with 0.01 M PBS followed by 4%

843 paraformaldehyde (PFA) in 0.01 M PBS. The extracted intact brains were postfixed

844 overnight at 4°C and placed in 30% sucrose for 48-72 h, and 50-μm frozen sections

845 were maintained across the whole brain (except that one mouse of lAAV[1,000,000] where

846 sections of injection site were cut into 100-μm to maintain the structures of local

847 axons, **Supplementary Fig. 5a**) with a freezing microtome (CryoStar NX50 cryostat,

848 Thermo Scientific, San Jose, CA). All brain slices were stored in a 24-well plate with

849 PBS, and representative slices with labeled neurons in the injection site and long-

850 range projections away from the injection site were identified with a Slide-scanning

851 Microscope (Nikon Ni-E, Japan) for further analysis.

852 **Immunohistochemistry.** Brain slices at the injection site of cslAAV[20,000]-labeled

853 ChAT-Cre transgenic mice (**Fig. 5c** and **Supplementary Fig. 7**) and cslAAV[8,000]-

854 labeled DAT-Cre transgenic mice were selected for immunostaining. The following
855 antibodies: (i) Primary antibody, including goat anti-choline acetyltransferase
856 (Millipore, AB144p, 1:200) and Rabbit anti-TH (abcam, ab112, 1:500); (ii) Secondary
857 antibody, rabbit anti-Goat cy3 (Jackson Immunoresearch, 305-165-003, 1:500), Goat
858 anti-rabbit Alexa 555 (Invitrogen, A21429, 1:500) were used in this study. Breifly, the
859 selected 50-μm floating sections were initially blocked in 10% rabbit serum in PBS
860 with 0.3% Triton X-100 (PBST) for 1 h at 37℃ and then washed with 0.3% PBST 10
861 min three times. Subsequently, sections were incubated in corresponding primary
862 antibodies at 4℃ for 48-72 h followed by washes with 0.3% PBST 10 min three times
863 and incubation in corresponding secondary antibodies at room temperature for 2 h.

864 **Image Acquisition.** All brain slices were counterstained with 4′,6-diamidino-2-
865 phenylindole (DAPI) to determine the cortical and laminar borders, coverslipped with
866 Anti-fade Fluorescence Mounting Medium (Beyotime Biotechnology, China) and
867 sealed with nail polish for imaging.

868 To quantify the whole-brain direct input neurons (**Fig. 2**, **Supplementary Fig. 4**
869 and **Supplementary Table 1**), all coronal sections throughout ten brains labeled by
870 MAP-ENVIVIDERS and classical rAAV-RV system were obtained through Nikon
871 VS120 (Japan) with two (one for DAPI, one for DsRed) or three channels (the third
872 for EGFP in injection site).

873 Except for images for input cells counting, all the other fluorescent images
874 presented were acquired with a confocal laser scanning microscope (LSM710; Carl
875 Zeiss, Germany) equipped with 405/488/514/561/633 excitation laser lines. 10x
876 objectives (NA0.5) with a step size of 2 μm, 20x (NA0.8) with a step size of 1 μm,
877 and 40x oil (NA1.4) with a step size of 0.39 μm were used. Generally, whole coronal
878 sections containing the injection site were acquired at 10x (NA0.5) with a zoom of 1
879 or at 20x (NA0.8) with a zoom of 0.6. Regions of labeled somas were imaged and
880 obtained in z-stacks with 10x (step size: 2 μm) or 20x objectives (step size: 1 μm). To
881 obtain fine structures such as dendrite and axonal arborizations, 40x oil (step size:
882 0.39 μm) with a zoom of 1 was used for most images except for proximal spines of
883 CA3 pyramidal neurons, where a zoom of 2 or 3 with the same objective was used
884 (**Supplementary Fig. 8d**).

885 To faithfully compare the signal intensities among different labeling conditions
886 (single virus vs. mixed viruses, littermate vs. stranger mixture, and littermate mixture
887 vs. Thy1-EYFP-H line transgenic mice), parameters were adjusted low enough to

888   ensure the fluorescent signal unsaturated, and then the same set of parameters was

889   applied to all samples. The acquired z-stacks were stored in 16-bit depth TIFF format.

890   **Resin Embedding.** For whole-brain imaging with the TDI-fMOST system, a

891   lAAV^{200,000}-labeled MOp mouse sample and a cslAAV^{20,000}-labeled basal forebrain

892   mouse sample were embedded with Technovit 9100 Methyl Methacrylate (MMA,

893   Electron Microscopy Sciences, USA) according to previous procedures with minor

894   optimizations[66]. Briefly, the removed PFA postfixed mouse brains were first rinsed in

895   0.01 M PBS for 12 h followed by complete dehydration in a series of alcohol (50%,

896   75%, 95%, 100%, and 100% ethanol, 2 h for each) and then xylene solution (twice, 2

897   h for each) for transparentization. The transparent brain was treated with sequential

898   infiltration solutions (50%, 75%, 100%, and 100% resin in 100% ethanol, 2 h each for

899   the first three solutions and 48 h for the final solution). Finally, the infiltrated brain

900   was placed into a gelatin capsule filled with polymerization solution and kept in a dry

901   chamber at -4°C in the dark for 72 h for polymerization before whole-brain sectioning.

902   **Dual-color, whole-brain imaging with the TDI-fMOST system.** Brain-wide images

903   of the embedded mouse brain were acquired with the TDI-fMOST system at a voxel

904   size of $0.176 \times 0.176 \times 1$ μm^3 (unpublished data)[37]. Dual-color, whole-brain imaging

905   with real-time propidium iodide (PI) staining was performed as previously described[67].

906   The embedded mouse brain was immersed in 0.05 M Na$_2$CO$_3$ solution to enhance the

907   EYFP signal and decrease the fluorescence background during the process of imaging

908   and sectioning[66]. A 60x water-immersed objective (NA 1.0) was used to image the

909   surface layer of the brain sample with an axial step size of 1 μm each cycle prior to

910   sectioning with a diamond knife. Each coronal section was acquired with 16-bit and

911   8-bit depth for the green and PI channels, respectively. After ten to twelve days of

912   uninterrupted imaging and sectioning, we eventually obtained whole-brain raw data

913   with a total of 12,841 continuous coronal sections for the MOp brain sample (70.2 TB

914   with 46.4 TB for green and 23.8 TB for red channels) and 10,781 continuous coronal

915   sections for the BF brain sample (54.7 TB with 36.8 TB for green and 17.9 TB red

916   channels), respectively.

917   **Image processing.** Raw data acquired with the dual-color TDI-fMOST system were

918   preprocessed based on reported methods[67], including seamless stitch and image

919   registration for two channels. The preprocessed images were stored in an LZW

920   compression TIFF format, with 16-bit depth for the green channel and 8-bit depth for

921   the PI channel. For the generation of 3D reconstructions of brain-wide long-range

922   projections of the MOp and basal forebrain mouse sample, we selected 12,740 and
923   10,780 continuous coronal sections from the respective green-channel data set and
924   resampled to $2 \times 2 \times 4$ μm^3 before loading them into the Amira software (Visage
925   Software, San Diego, CA). For the presentation of the MOp whole-brain dataset
926   (**Supplementary Fig. 9**), coronal sections with maximum intensity projections
927   (**Supplementary Fig. 9a-m**) were resampled to 0.6×0.6 μm^2 due to the large image
928   size, and images to display fine structures, including somas, axonal branches and
929   axonal arborizations (residual images in **Supplementary Fig. 9**) were all selected
930   from corresponding coronal sections of original resolution (0.176×0.176 μm^2).

931   Raw data acquired with Nikon VS120 for whole-brain cell counting of input
932   networks were transformed into JPG formats suitable for the following analysis. All
933   confocal images were stored in lossless TIFF format. Image processing, including
934   maximum intensity projection of serial z-stacks, adjusting brightness, and contrast of
935   the composite images and selection of regions of interest, were performed with
936   ImageJ (National Institutes of Health, USA). In addition, images imported from the
937   Amira software were also processed as mentioned.

938   **Morphology reconstructions of individual neurons in MOp and BF.** These
939   reconstructions were performed in the Filament Editor module of the Amira software
940   (Mercury Computer Systems, San Diego, CA, USA) via a human-machine interaction
941   pattern. For the reconstructions of neurons 1-8, we randomly chose two neurons in L2,
942   one neuron in L3, one neuron in L6a and four neurons in L5b and started neuronal
943   tracing from the soma. We first traced local axons projecting from the main axons,
944   followed by the tracing of main axons projecting to contralateral parts or subcortical
945   regions. For the reconstructions of neurons **s1-s3**, we selected axons in the anterior
946   commissure (ac) as a start point and traced in two opposite directions, with one
947   towards the ipsilateral part and the other towards the contralateral part. For the
948   reconstructions of neurons **c1-c4**, we selected complex axonal arborizations in the
949   ipsilateral anterolateral/lateral visual area (VISal/l), ipsilateral caudoputamen (CP),
950   ipsilateral and contralateral hippocampus as the start point and traced retrogradely.
951   Because the axonal arborizations of most neurons were extremely complex and
952   intermingled with each other, we made detailed registrations of the number and
953   projection directions of all the branches to avoid negligence. For better differentiation,
954   each part of the neuron, including the local axons, ipsilateral branches, and
955   contralateral branches, were reconstructed separately. A constant $1000 \times 1000 \times 400$

956   μm^3 data block was imported into the Amira software in each cycle of tracing. After
957   complete reconstructions of all arborizations of one branch, we moved to the next
958   branch and repeated the tracing steps until all the branches projecting from the main
959   axons were reconstructed. During the process of tracing, two tracing modules, thin
960   structure and linear options were used alternatively according to the sparseness of the
961   axonal projections. For example, if the axonal projections were sparse and not
962   interfered by other axons, the thin structure module was used to depict the axonal
963   projection path from the start point to the end; otherwise, the linear module was
964   utilized to gradually trace the path. The brightness and thickness of the data block
965   were adjusted from time to time in the process of tracing based on the different
966   conditions of the axonal projections. The dendrite morphologies of all neurons were
967   reconstructed in the same way as axonal tracing but separately for convenient
968   subsequent analysis. The tracing results for each neuron, including the axonal
969   projections and dendrite morphologies, were rechecked by different skilled
970   technicians, and neurons with uncertainties were excluded from the final results. The
971   locations of nuclei were based on the Allen Brain Atlas (http://mouse.brain-
972   map.org/static/atlas) with the aid of PI-staining signals.

973   The reconstructed axons and dendrites of neurons **s1-s3** and **c1-c4** were saved in SWC
974   files for the quantitative analysis of the branches and length in the software
975   Neurolucida Explorer (MicroBrightField, USA).

976   **Axonal bouton counting.**   To make faithful manual counting of axonal boutons, we
977   initially processed the raw signal of cslAAV[20,000]-labeled basal forebrain mouse
978   sample with 20- to 100 μm-thickness maximum-intensity projections depend on the
979   sparseness of axons. Subsequently, we randomly selected ten regions of interest
980   (ROIs) from respective coronal sections of four cholinergic neurons (No. c1-c4).
981   Counting of axonal boutons along the axonal shaft in each ROI were performed
982   manually using multi-point tool in ImageJ according to the previously published
983   cirteria[15,16] (**Figs. 6d** and **Supplementary Fig. 15**). The axonal pathway in each ROI
984   was depicted in Amira software as mentioned above. The averaged bouton density
985   (bouton/μm) in each ROI was defined as the ratio of total number of boutons over
986   axonal length (**Figs. 6g** left). Based on the averaged bouton density of ten ROIs and
987   total axonal length of reconstructed neurons, estimated total number of boutons of
988   each cholinergic neuron was thus obtained (**Figs. 6g** right).

989   **Statistical analysis.** Measurements of the signal profile (**Figs. 7a**,**b**,**e** and

990   **Supplementary Figs. 4a**,**7b**) and relative fluorescence intensity (**1d**,**2f**,**3d**,**e**,**5i**,**6c**,**f**

991   and **Supplementary Figs. 1**) were based on previously published methods with

992   ImageJ[31]. Briefly, the signal profile of each pixel was calculated by subtracting the

993   total signal value from the mean gray value of the background. We first measured the

994   total signal value by a straight line drawn across the signal area (somas in the

995   injection site or long-range axons) followed by measuring the mean gray value of the

996   background by another straight line drawn across the background area close to the

997   signal spot. For the measurement of relative fluorescence intensity, a rectangular

998   selection (white dashed boxes) covering the signal spot (neuronal cell bodies) was

999   made followed by the recording of the area of the boxes and the integrated density

1000   (IntDen) of the signal. To calculate the mean background, a straight line (yellow lines)

1001   was drawn across the background area close to the signal spot, and the mean gray

1002   value of the background was measured. The relative fluorescence intensity of each

1003   pixel was calculated by the relative signal values (resulting from subtraction of the

1004   total signal value from the total gray value of the background) over the pixel number

1005   of the area.

1006   For comparison of the ratio between the signal intensity of DsRed and EGFP in

1007   starter cells labeled by lAAV-DIO-GT/RG and sAAV-DIO-GT/RG, a total of 170

1008   starter neurons were selected randomly from 3 mice for both groups (**Fig. 1c** and

1009   **Supplementary Fig. 1a**, left panel. For comparisons of the signal intensity of DsRed

1010   in input cells within the lAAV-DIO-GT/RG- and sAAV-DIO-GT/RG labeling groups

1011   (**Fig. 2f** and **Supplementary Fig. 1a**, right panel), 160 input neurons for RT, 190

1012   input neurons for SSp and SSs were selected randomly from 3 independent

1013   experimental mice for both groups.

1014   For comparisons of the signal intensity of sparsely labeled neurons with non-cell-

1015   type-specific in wild-type mice (**Fig. 2d**,**e** and **Supplementary Fig. 1b**,**c**), 40 neurons

1016   from 2-5 brain slice of the injection site were selected randomly from three

1017   independent experimental mice for lAAV[20,000], lAAV[200,000], sAAV[20,000], sAAV[40,000] and

1018   sAAV[80,000], and 20 out of 24 neurons were selected from lAAV[1,000,000,] and 17 out of

1019   26 neurons were selected from sAAV[1,000,000] (the other 9 neurons were hardly captured

1020   under low imaging parameters). As comparisons, 40 neurons of MOp, CA1 and CA3

1021   regions were selected randomly from brain slices of Thy1-EYFP-H transgenic mice

1022   with similar bregma.

1023   For comparisons of the signal intensity of sparsely labeled cell-type-specific

1024   neurons (**Fig. 5i**), 40 neurons from 2-4 brain slices of the injection site were selected

1025   randomly from three independent cssAAV^{20,000}-labeled Thy1-Cre mice, cssAAV^{20,000}-

1026   labeled ChAT-Cre mice and cssAAV^{8,000}-labeled DAT-Cre mice.

1027   For comparisons of signal intensity of EYFP and mCherry (**Fig. 7c**), 90 neurons

1028   from brain slices of the injection site were selected randomly from 3 independent

1029   experimental mice for the sAAV-EYFP/mCherry, rAAV2/9-EF1α-EYFP/PBS mixture

1030   (ratio of 1:1) and rAAV2/9-EF1α-mCherry/PBS mixture (ratio of 1:1).

1031   Whole-brain counting of input cells was performed following previously

1032   published methods[32,33]. Briefly, input cells in each coronal section were identified

1033   manually, followed by registration of each coronal section to the Allen Brain Atlas

1034   (ABA, http://mouse.brain-map.org/). We summed the total number of input neurons

1035   and calculated the convergent index (ratio between input cells and starter cells)[8] in

1036   diverse gross regions and subregions. For the demonstration of relationship between

1037   proportion of inputs and enhanced ratios of tracing efficiency provided by MAP-

1038   ENVIVIDERS (**Fig. 2e**), we calculated selected 44 representative subregions from 11

1039   major regions from sAAV-DIO-GT/RG labeling groups and calculated proportion of

1040   inputs, i.e. inputs in these subregions against total inputs (for better demonstration,

1041   proportion of inputs in x-axis were listed by logarithm to base 10, denoted by lg %).

1042   Enhanced ratios of tracing efficiency provided by MAP-ENVIVIDERS (y-axis) were

1043   denoted by convergent index of lAAV-DIO-GT/RG dividing by convergent index of

1044   sAAV-DIO-GT/RG in diverse subregions.

1045   All quantitative data, including cell numbers and measurement of relative signal

1046   intensity, convergent index and proportion of inputs, were all presented as the mean ±

1047   s.e.m. Significance was analyzed using one-way ANOVA with Dunnett's post hoc test

1048   (**Fig. 3d**), Turkey's post hoc test (**Fig. 5i**), Student's t-test (**Figs. 1d**,2**f**,3**e**,7**c**,**f**) and

1049   Mann-Whitney U test (**Figs. 2a-d** and **Supplementary Fig. 4**) in GraphPad Prism

1050   version 6.0 (GraphPad Software Inc., San Diego, CA, USA).

1051

1052

1053

1054

1055

1056 # Supplementary Information

1057 ## Supplementary Figure 1
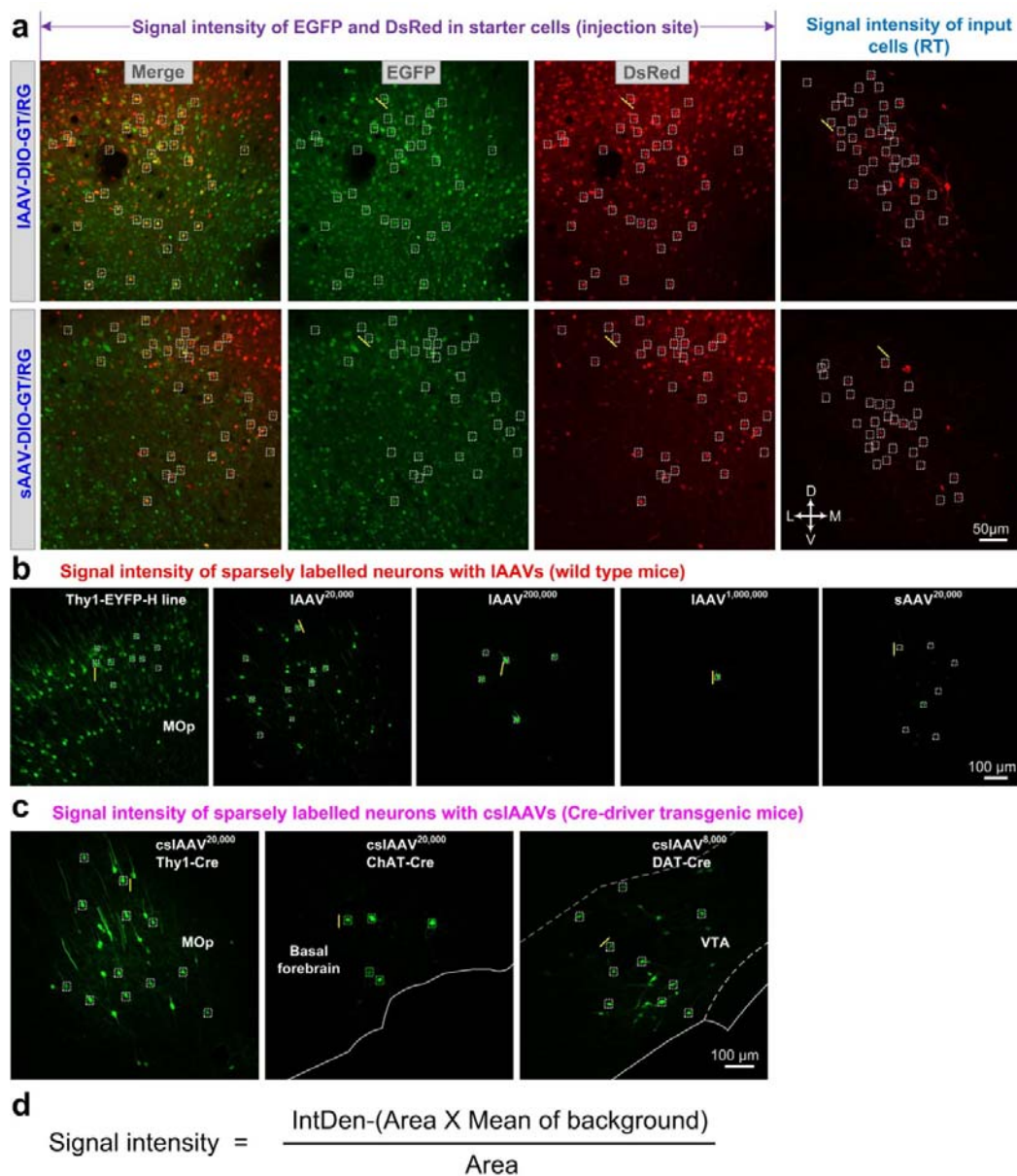
1058

1059 **Supplementary figure 1**

1060 **Schematic of measuring fluorescence intensity of individual neurons.**

1061 **(a)** Representative confocal images showing the measurement of signal intensity of
1062 EGFP and DsRed in starter cells and DsRed-labeled input cells in lAAV-DIO-
1063 GT/RG- and sAAV-DIO-GT/RG-treated mice. All of the images were obtained under
1064 the same imaging conditions (low laser intensity was used to avoid over-exposure of
1065 the cell bodies).

1066   **(b)** Representative confocal images showing the measurement of signal intensity of
1067   neurons in Thy1-EYFP-H line transgenic mice and sparsely labeled neurons with
1068   diverse lAAVs and sAAVs in MOp region.

1069   **(c)** Representative confocal images showing the measurement of signal intensity of
1070   neurons in cssAAV^{20,000}-labeled Thy1-Cre mice (MOp), cssAAV^{20,000}-labeled ChAT-
1071   Cre mice (basal forebrain) and cssAAV^{8,000}-labeled DAT-Cre mice (VTA).

1072   **(d)** The signal intensities were calculated in ImageJ according to the formula in **d** and
1073   the method in the previous report[31]. Briefly, a rectangular selection (white dashed
1074   boxes) covering the signal spot (neuronal cell bodies) was made, and then the area of
1075   the boxes and the integrated density (IntDen) of the signal were recorded. To calculate
1076   the mean background, a straight line (yellow lines) was drawn across the background
1077   area close to the signal spot and the mean gray value of the background was measured.
1078   This method was applied to calculate the signal intensities in **Figs 1d**,**2d**,**3d**,**e**,**5j**,**7c**.

1079   Abbreviations: MOp, primary motor area; RT, reticular nucleus of the thalamus; VTA,
1080   ventral tegmental area.
1081

1082

1083

1084

1085

1086

1087

1088

1089

1090

1091

1092

1093

1094

1095

1096 **Supplementary Figure 2**
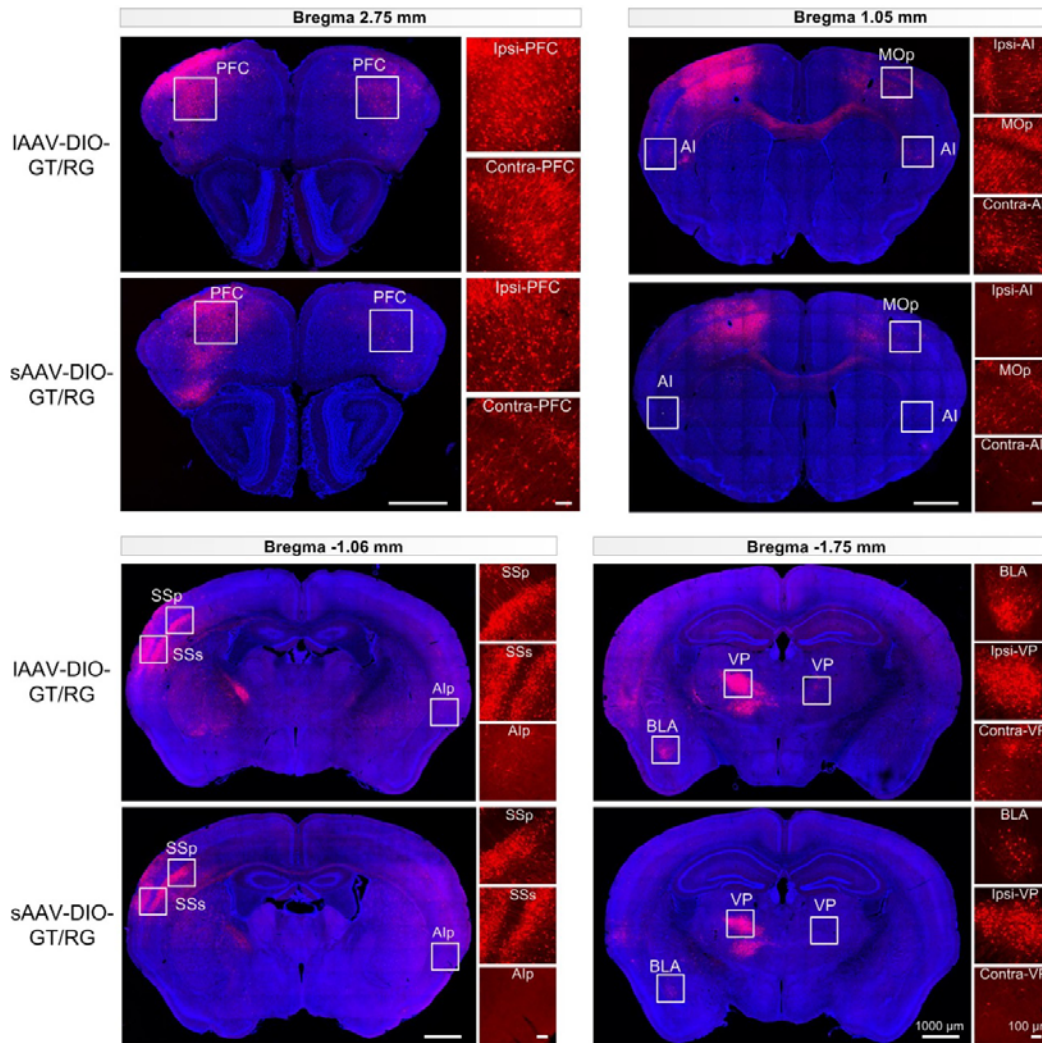
1097
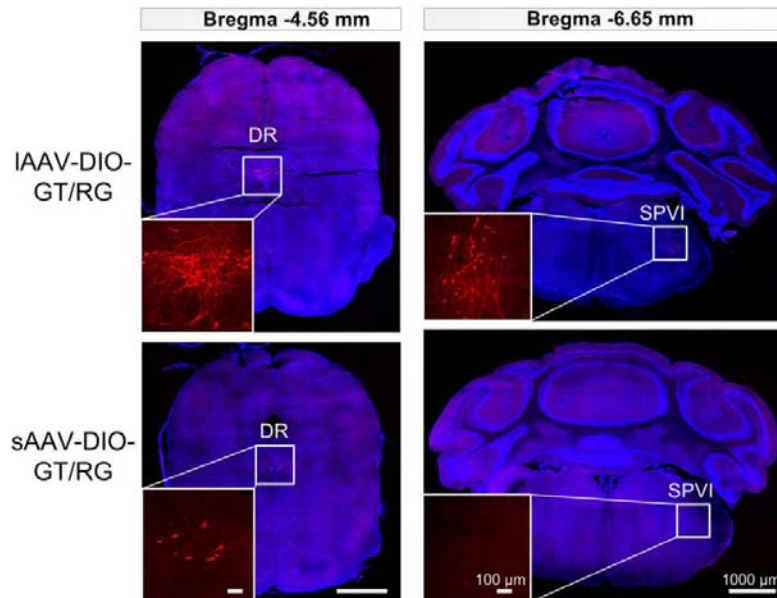
1098

1099 **Supplementary figure 2**

1100 **Localization of nuclei demonstrated in Fig. 6e with the aid of DAPI (4',6-**
1101 **diamidino-2-phenylindole) staining**.

1102 Abbreviations: AI, agranular insular area; AIp; agranular insular area, posterior part;
1103 BLA, basolateral amygdalar nucleus; DR, dorsal nucleus raphe; MOp, primary motor
1104 area; PFC, prefrontal cortex; SPVI, spinal nucleus of the trigeminal, interpolar part;
1105 SSp, primary somatosensory area; SSs, supplemental somatosensory area; VAL,
1106 ventral anterior-lateral complex of the thalamus; VP, ventral posterior complex of the
1107 thalamus.

1108

1109

1110

1111

1112

1113

1114

1115

1116

1117

1118

1119

1120

1121

1122

1123

1124

1125

1126

1127 **Supplementary Figure 3**
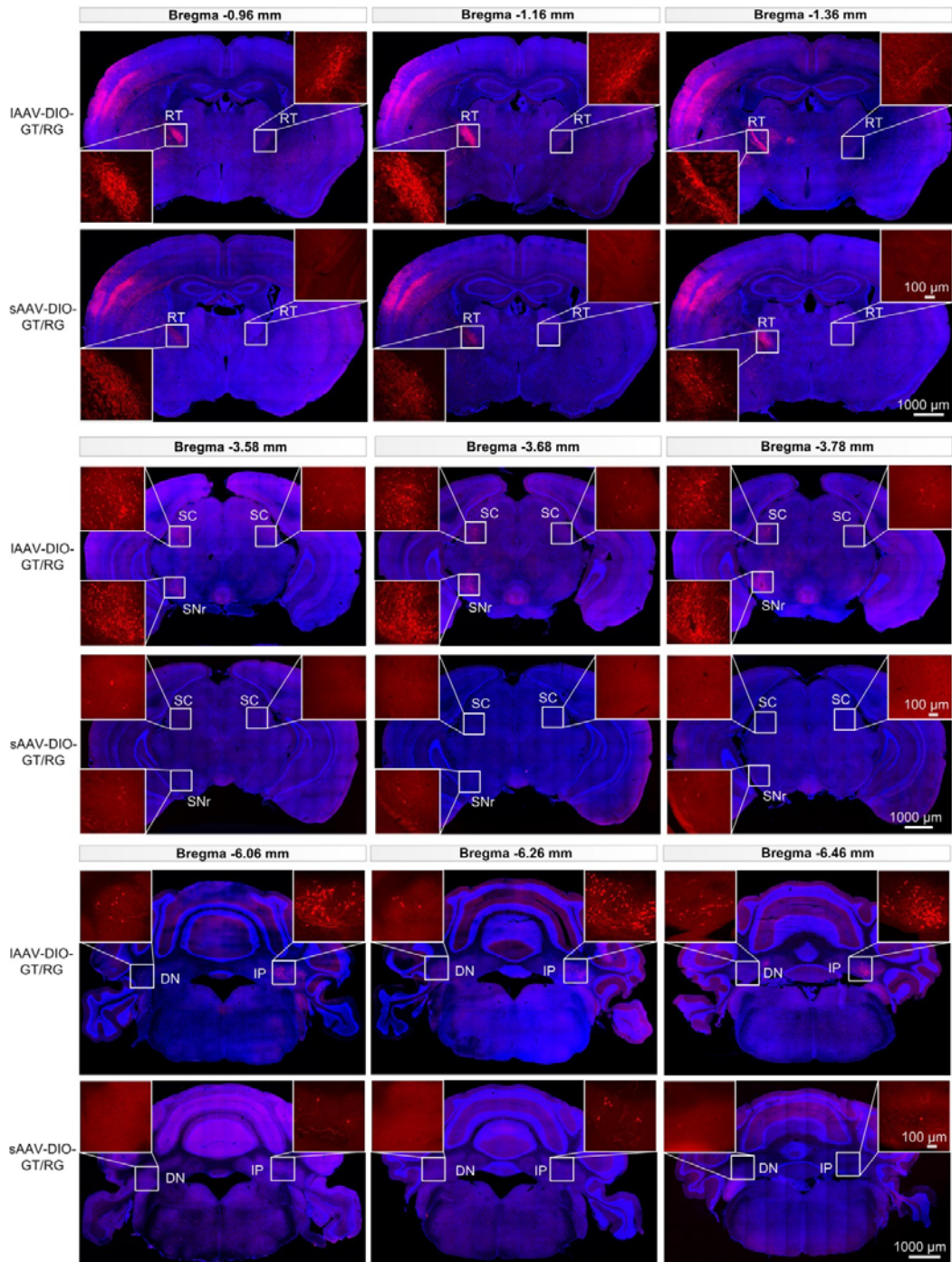
1128

1129 **Supplementary figure 3**

1130 **Comparisons of inputs in RT of thalamus, SC and SNr of midbrain, DN and IP**
1131 **of cerebellum between lAAV-DIO-GT/RG and sAAV-DIO-GT/RG labeling**
1132 **groups.** Insets were enlargements respective brain regions. DN, dentate nucleus; IP,

1133 interpeduncular nucleus; RT, reticular nucleus of the thalamus; SC, superior colliculus;

1134 SNr, substantia nigra pars reticulate.

1135 **Supplementary Figure 4**
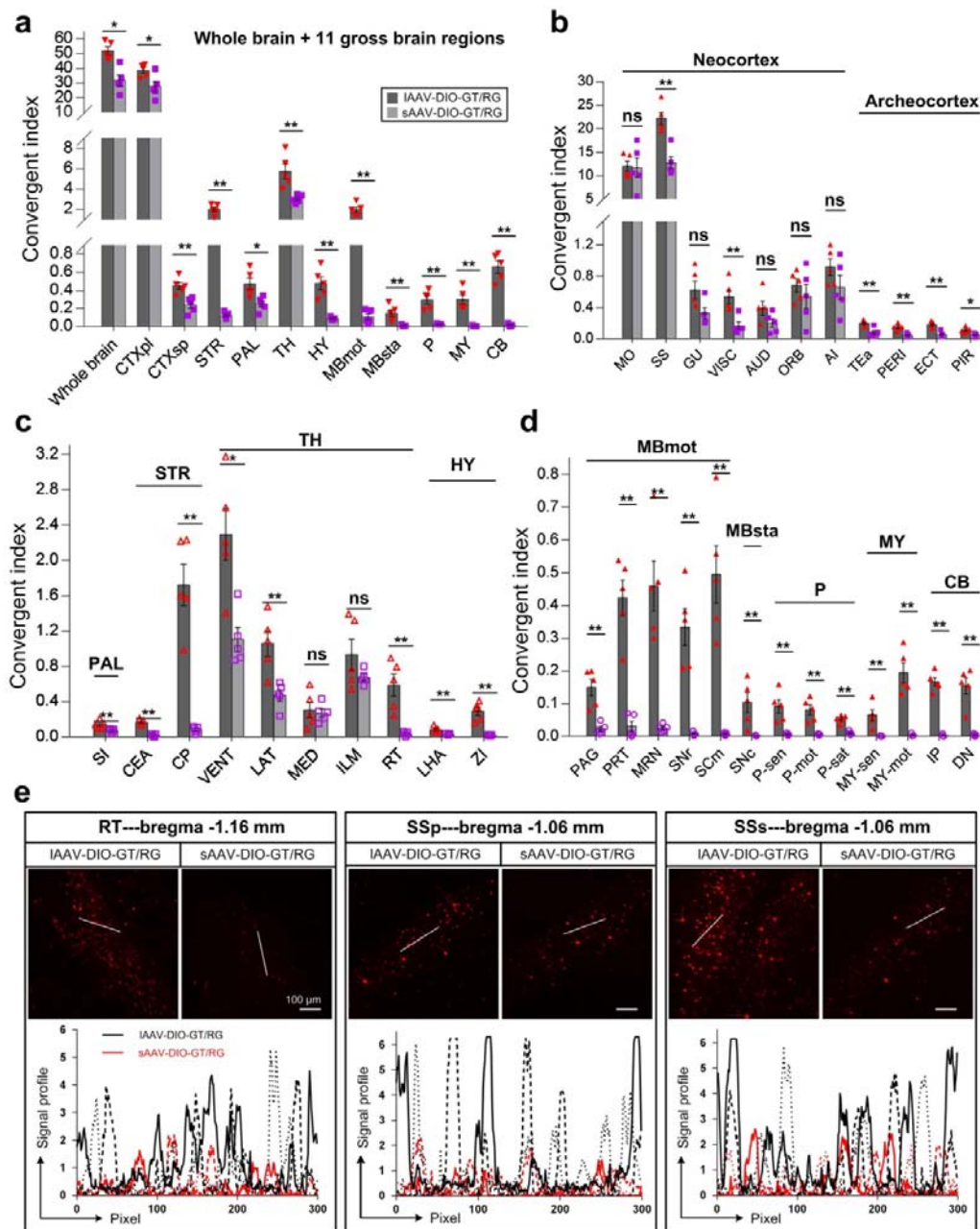
1136

1137

1138

1139

1140

Supplementary figure 4

(a-d) Brain-wide comparisons of tracing efficiency between lAAV-DIO-GT/RG and sAAV-DIO-GT/RG labeling groups.

(a) Comparisons of convergent index of total inputs and 11 gross brain regions.

(b) Comparisons of convergent index in diverse cortical regions.

(c) Comparisons of convergent index in pallidum (PAL), striatum (STR), thalamus (TH) and hypothalamus (HY).

(d) Comparisons of convergent index in midbrain, motor related (MBmot), midbrain, behavioral state related (MBsta), pons (P), medulla (MY) and cerebellum (CB).

All data are presented as mean ± s.e.m. n = 5 mice for each group in **a-d**. Mann-Whitney U test. n.s, non-significant (P > 0.05), *P < 0.05, **P < 0.01.

(e) Signal profile of input neurons in RT, SSp and SSs in lAAV-DIO-GT/RG and sAAV-DIO-GT/RG labeling groups. n = 3 mice for each group.

Abbreviations see **Supplementary Table 2**.
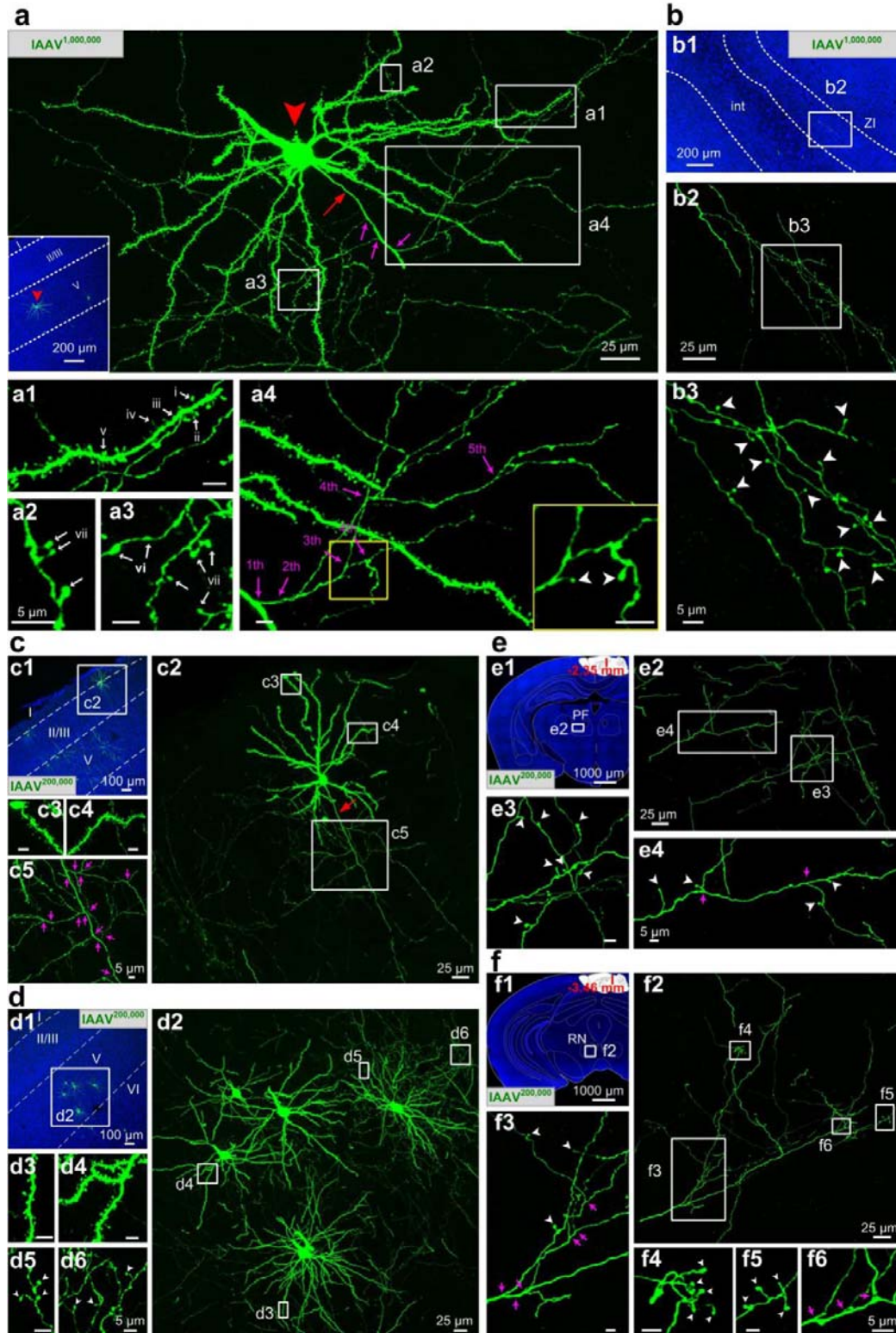
1169   **Supplementary Figure 5**

1170

1171

Supplementary figure 5

Fine structures of individual neurons labeled with lAAV^{1,000,000} and lAAV^{200,000}.

(a) Confocal image (100-µm thickness) of a representative individual neuron labeled with lAAV^{1,000,000} in injection site. Inset showed the localization of cell body (indicated by red arrowhead). **(a1)** Five types of spines: (i) mushroom, (ii) thin, (iii) stubby, (iv) filopodium, and (v) branched spines. **(a2-a3)** Two types of boutons: (vi) en passant boutons and (vii) terminal boutons. **(a4)** Different levels of local axonal collaterals.

(b) Confocal images of representative long-range axonal projections in the ZI region **(b1)** labeled with lAAV^{1,000,000}. Fine structures were progressively enlarged from **b1** to **b3**.

(c-d) Fine structures of MOp L2 (**c**) and L5 (**d**) pyramidal neurons labeled with lAAV^{200,000} in injection site. **c1** and **d1** were low-magnification images indicating the locations of cell bodies. **c2** and **d2** were high-magnification images showing the fine structures of the representative neurons. **c3-c5** and **d3-d6** were enlargements of box regions in **c2** and **d2**, respectively.

(e-f) Fine structures of MOp long-range axonal projections labeled with lAAV^{200,000}. **e1** and **f1** were composite coronal sections indicated the locations of the axonal projections, including parafascicular nucleus (PF, **e1**) in thalamus and red nucleus (RN, **f1**) in midbrain. **e2** and **f2** were high-magnification images showing the fine structures of the complex axonal arborizations. **e3-e4** and **f3-f6** were enlargements of the boxed regions in **e2** and **f2**, respectively. Red arrows indicated the primary axon emitting from soma. The pink arrows and numerals indicate the orders of the axonal branches and bright, large bulb-shaped terminal boutons were indicated by white arrowheads.

Definition the boundary of cortical layers (indicated by white dashed lines) and location of nuclei were all based on DAPI (4',6-diamidino-2-phenylindole, blue) staining. int, internal capsule; ZI, zona incerta. I-VI, cortical layers I to VI.

1201 **Supplementary Figure 6**

1202
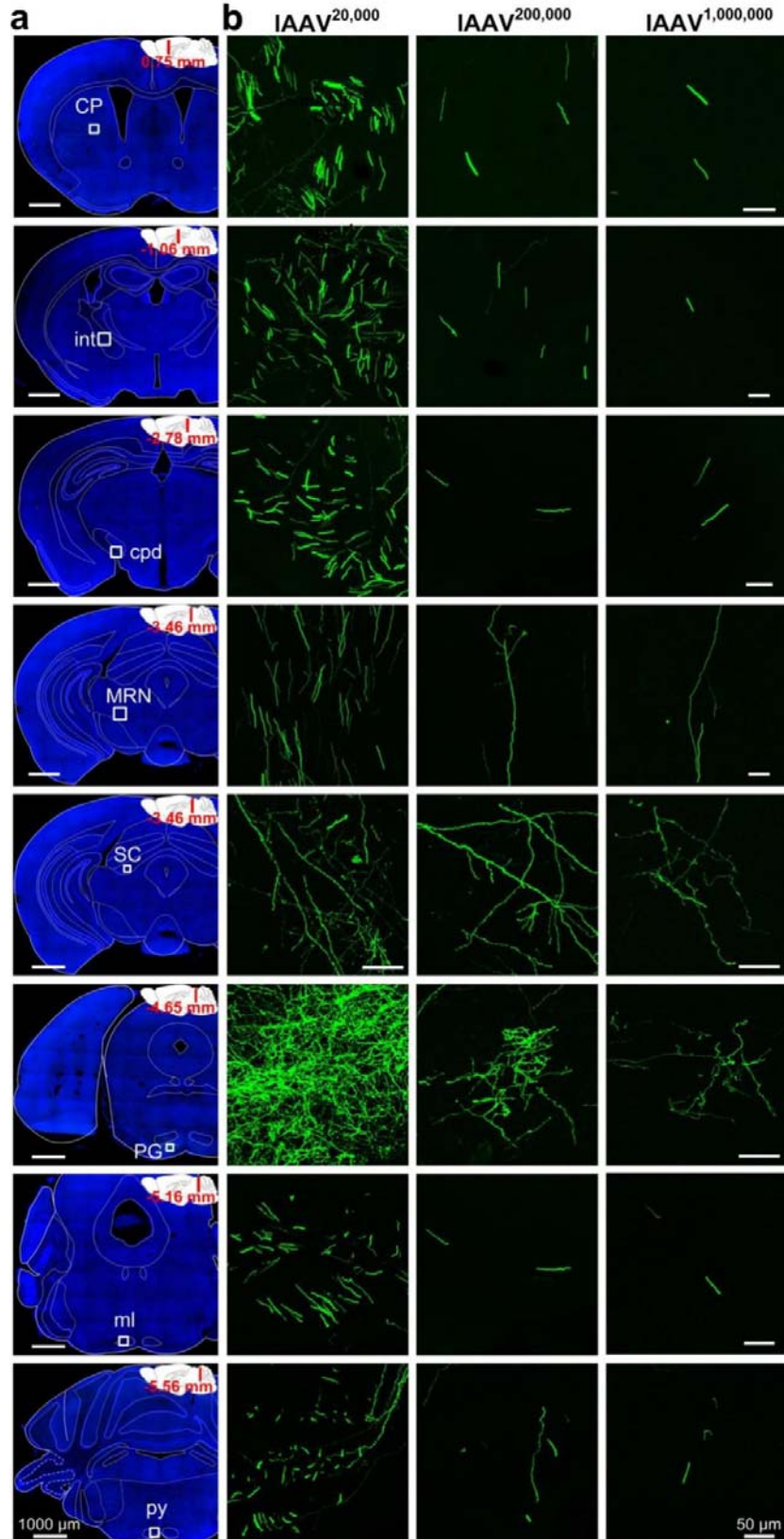
1203   **Supplementary figure 6**

1204   **Brain-wide long-range axonal projections of three lAAVs in MOp.**

1205   We injected equal volume (100 nl) of three lAAVs (lAAV^{20,000}, lAAV^{200,000} and
1206   lAAV^{1,000,000}) into MOp of wild-type mice. After 21d's expression, we examined
1207   brain-wide long-range axonal projections of three lAAVs, including CP (bregma level:
1208   0.75 mm), int (bregma level: -1.06 mm), cpd (bregma level: -2.78 mm), MRN and SC
1209   (bregma level: -3.46 mm), PG (bregma level: -4.65 mm), ml (bregma level: -5.16
1210   mm), and py (bregma level: -5.56 mm).

1211   **(a)** Composite coronal sections showing the locations of the axonal projections.

1212   **(b)** Maximum-intensity projections of the boxed regions in **a**, showing the fine
1213   structures of the axonal projections in different brain regions. Images coming from the
1214   same brain region were obtained with the same imaging conditions and processed
1215   identically.

1216   Abbreviations: CP, caudoputamen; int, internal capsule; cpd, cerebal peduncle; ml,
1217   medial lemniscus; MRN, midbrain reticular nucleus; PG, pontine gray; py, pyramid;
1218   SC, superior colliculus.

1219
1220

1221

1222

1223

1224

1225

1226

1227

1228

1229

1230

1231

1232

1233

1234
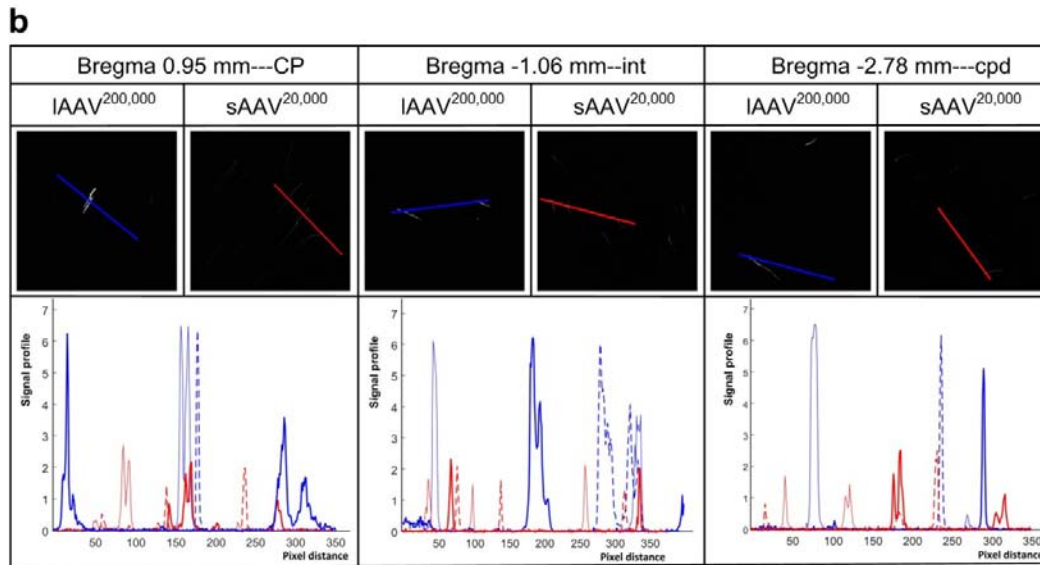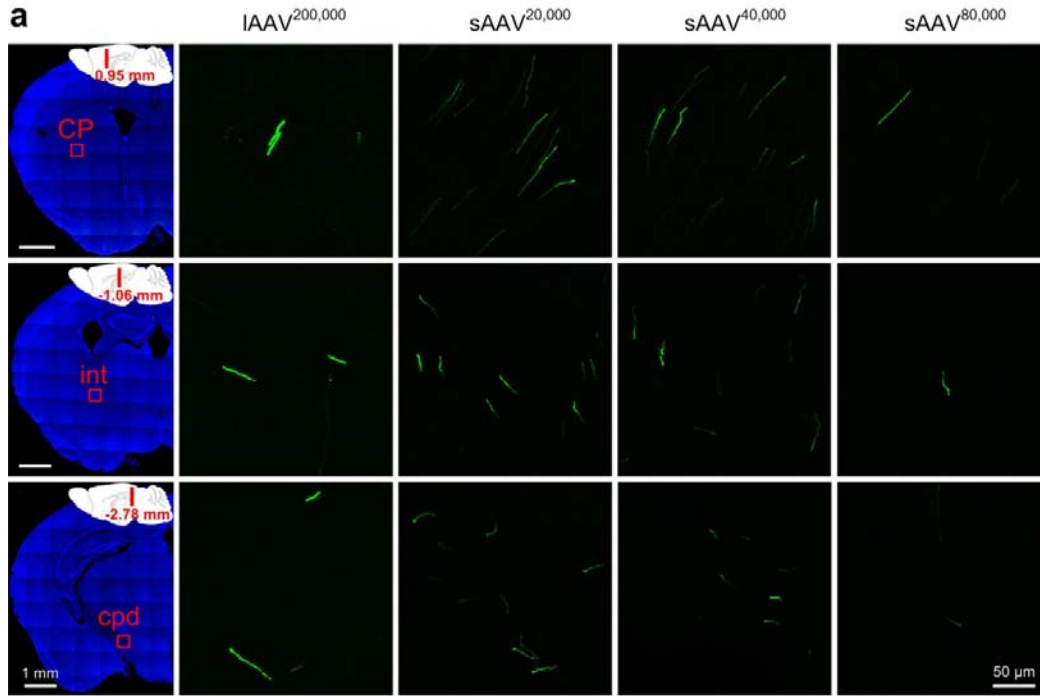
Supplementary Figure 7

Supplementary figure 7
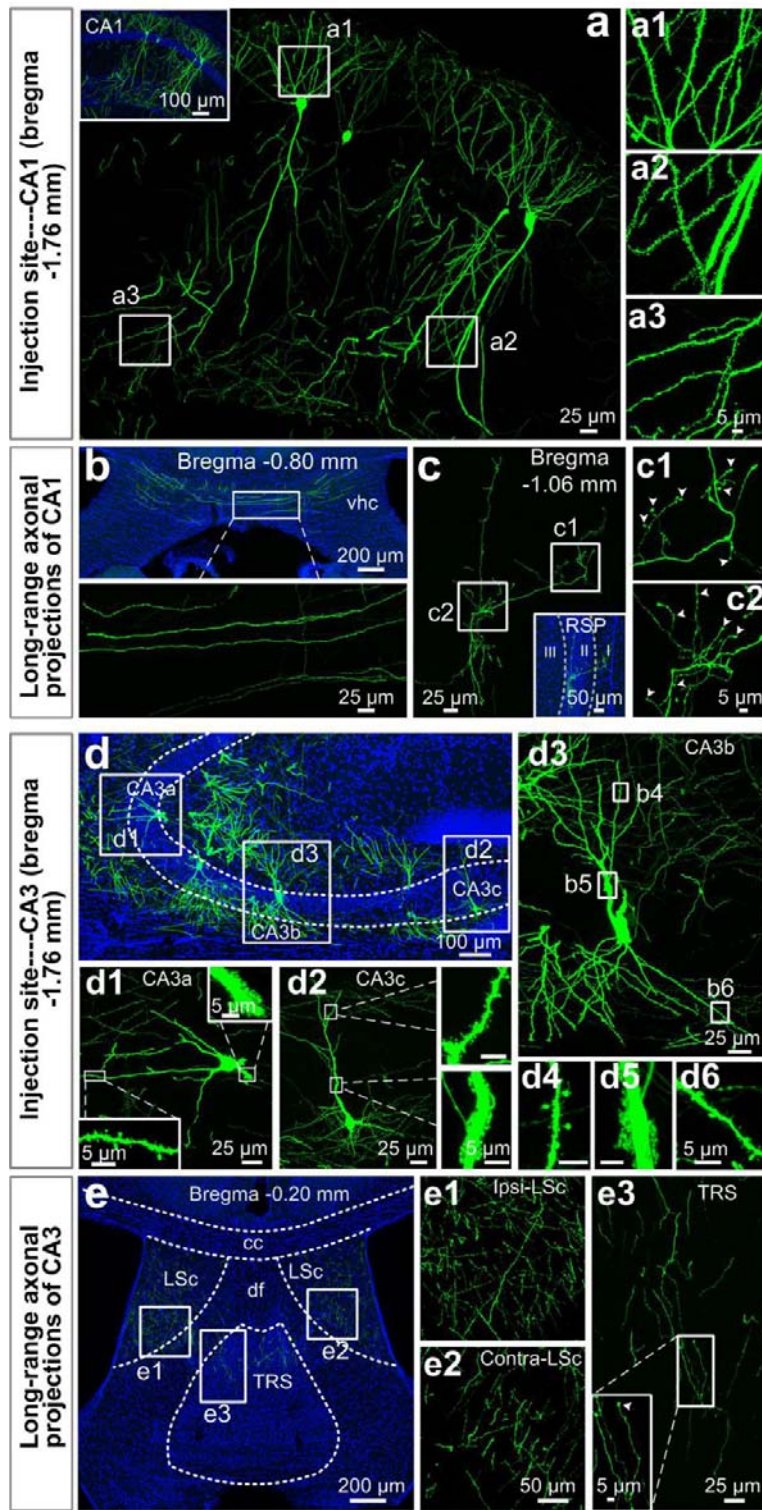
Comparisons of brightness of long-range axonal projections between lAAV^{200,000} and diverse sAAVs (sAAV^{20,000}, sAAV^{40,000} and sAAV^{80,000}).

(a) Representative confocal images of long-range axonal projections in different brain regions. All images in each brain region were obtained under the same imaging conditions and processed identically.

(b) Measurements of fluorescence intensities in **a** for lAAV^{200,000} (indicated by blue lines, three types of blue lines represent three different mice) and sAAV^{20,000} (indicated by red lines, three types of red lines represent three different mice). The data showed that the fluorescence in neurons labeled by lAAVs was stronger than by sAAVs.

1254 **Supplementary Figure 8**

1255

1256

1257

Supplementary figure 8

Applications of lAAV^{200,000} in CA1 and CA3 region.

(a-c) Applications of lAAV^{200,000} in CA1 region.

(a) Representative confocal images showing the fine structures of labeled neurons in injection site of CA1. Inset shows the locations of the somata.

(a1-a3) Enlargements of the boxed regions in **a** showing different parts of dendritic spines.

(b-c) Representative confocal images of the long-range axonal projections of CA1 in ventral hippocampal commissure (vhc, **b**) and retrosplenial cortex (RSP, **c**). **c1-c2** were enlargements of the corresponding boxed regions in **c**. Insets in **c** were approximate location of the axonal arborizations. White arrowheads indicate terminal boutons. White dashed lines on inset define the boundary of cortical layers based on DAPI staining.

(d-e) Applications of lAAV^{200,000} in CA3 region.

(d) Low-magnification images showing the overall labeling in CA3.

(d1-d3) Fine structures of the CA3a (**d1**), CA3b (**d3**), and CA3c (**d2**) pyramidal neurons. Respective box regions in **d1** and **d2** were enlarged to show proximal and distal dendritic spines.

(d4-d6) Enlargements of the box regions in **(d3)** showing apical **(d4),** proximal **(d5),** and basal dendritic spines **(d6)** of CA3b pyramidal neuron, respectively.

(e) Low-magnification images indicate the locations of the axonal projections in TRS and LSc. The location of nuclei was based on Paxinos Mouse Brain Atlas (PMBA) with the aid of DAPI staining. **(e1-e3)** High-magnification images of the boxed regions in **e** showing the fine structures of axonal projections and axonal terminals.

Abbreviations: CA1, field CA1 of hippocampus; CA3, field CA3 of hippocampus; cc: corpus callosum; df: dorsal fornix; DG, dentate gyrus; LSc: lateral septal nucleus, caudal (caudodorsal) part; TRS: triangular nucleus of septum.
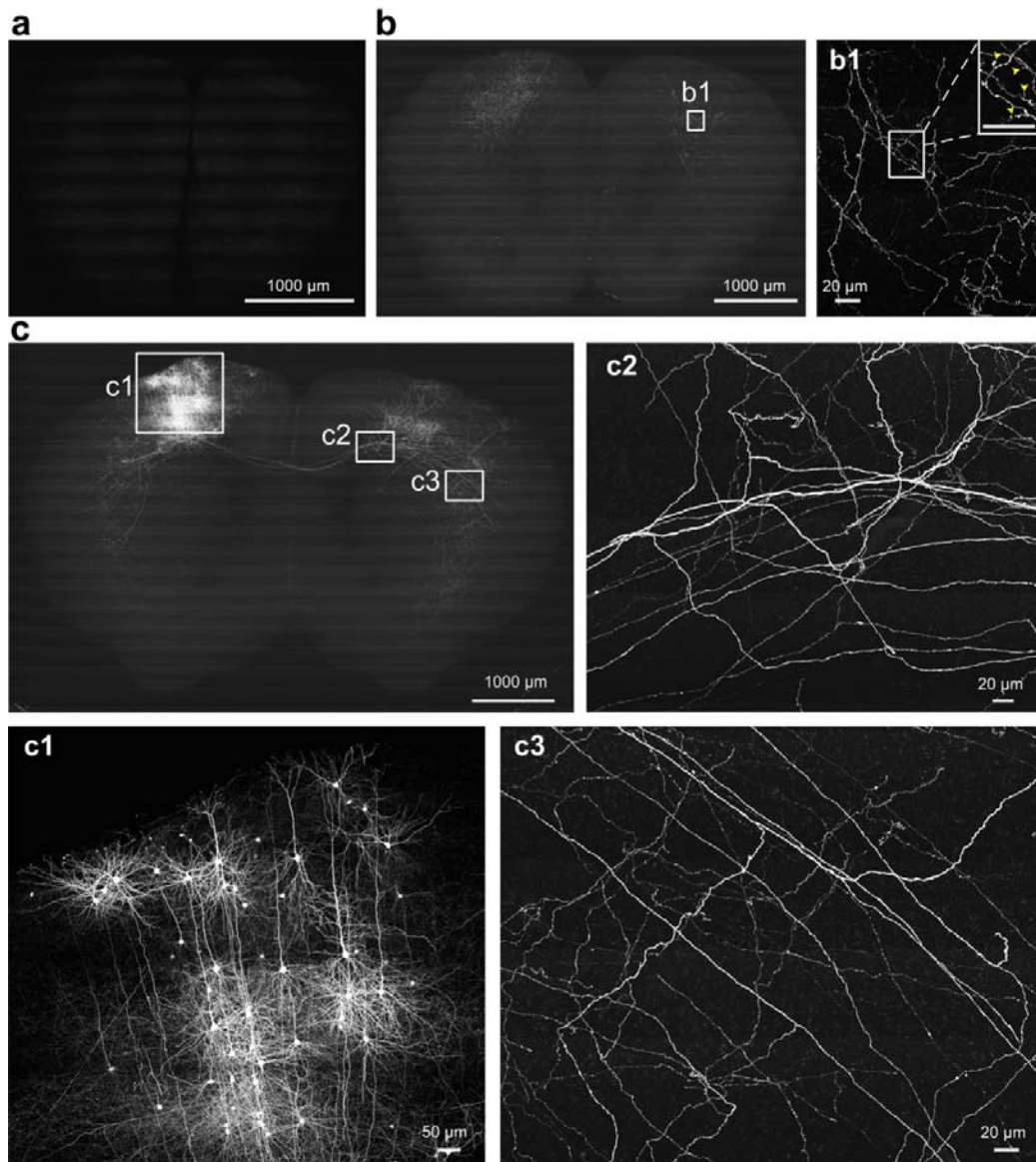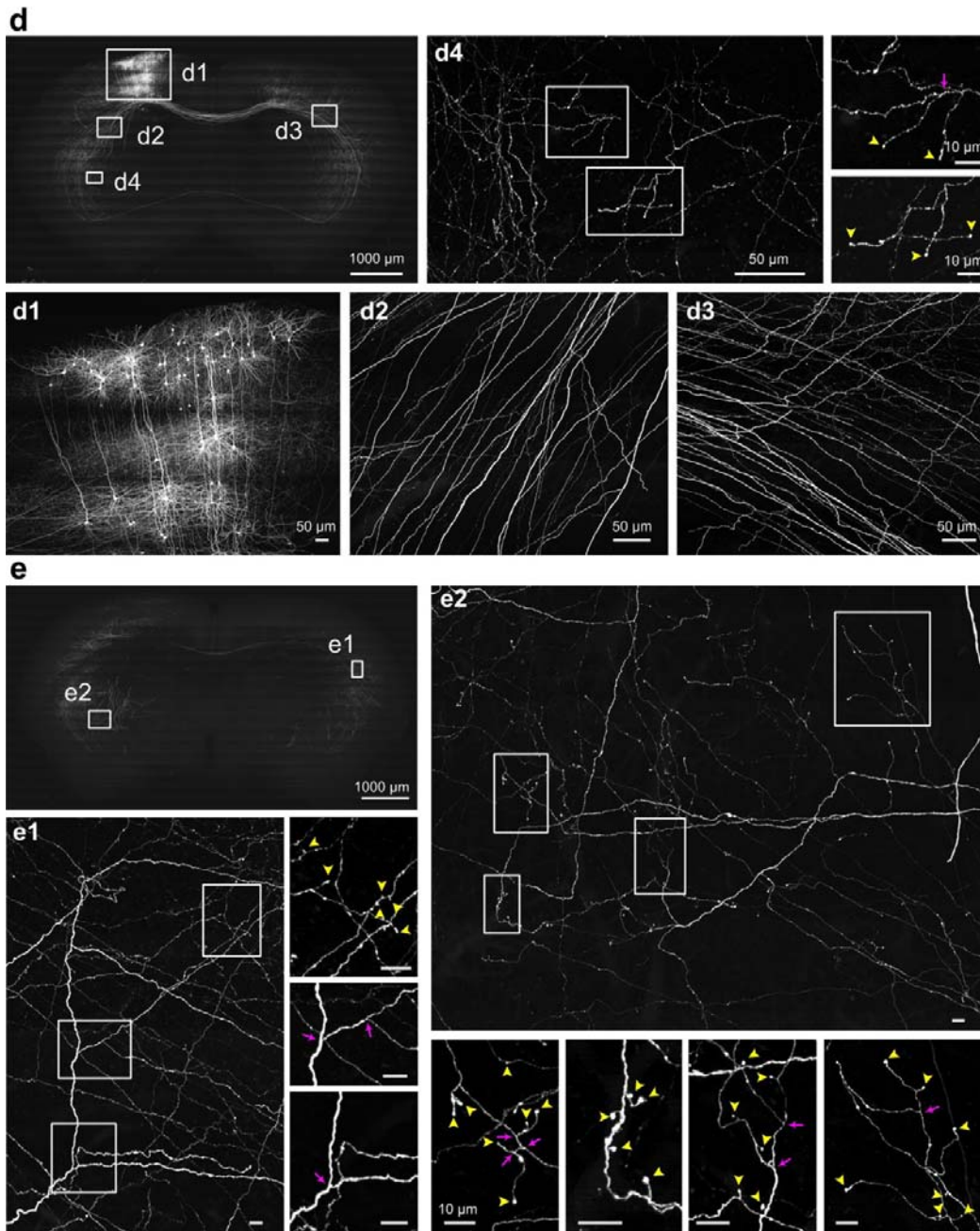
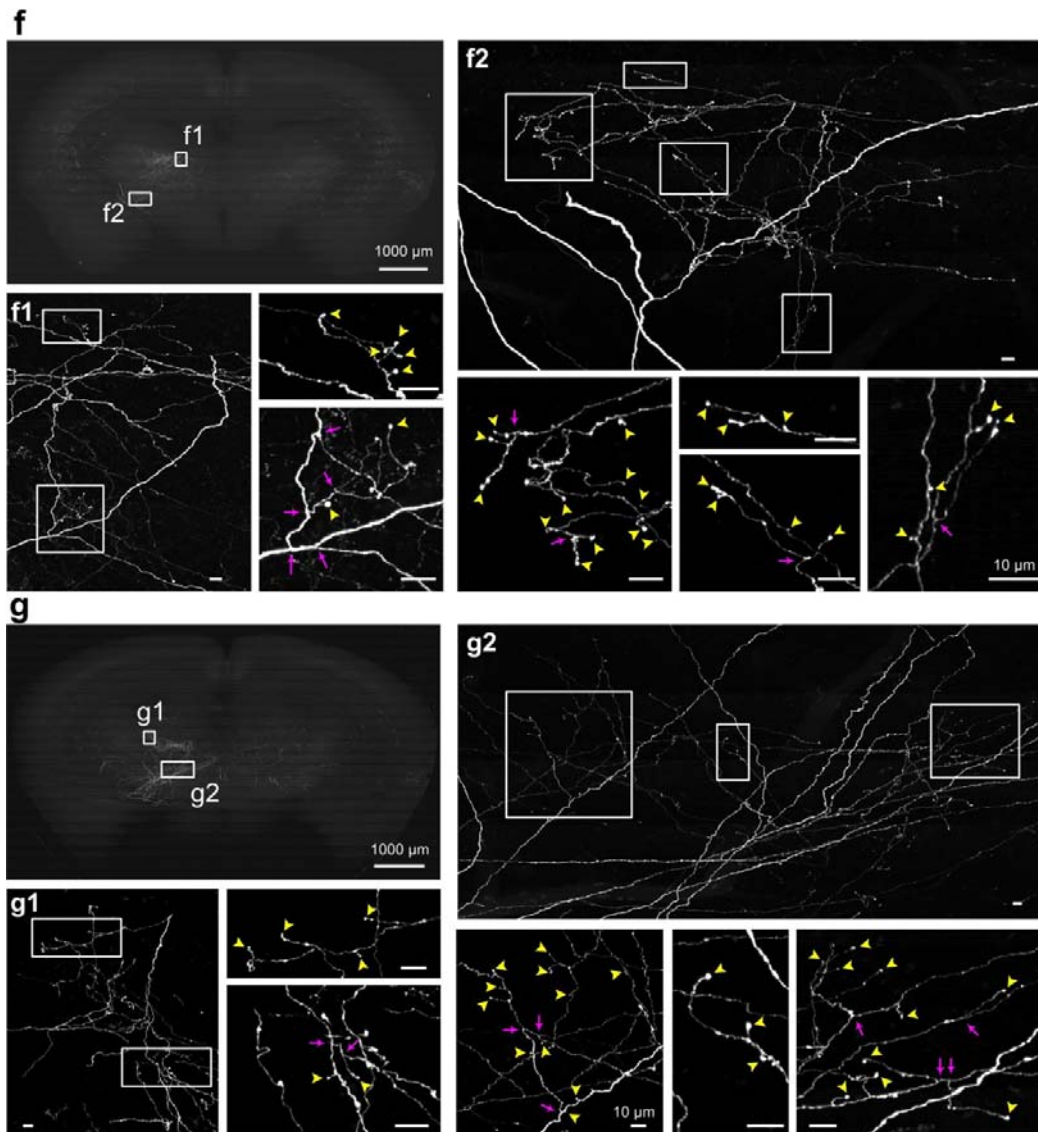1291 **Supplementary Figure 9**

1292
1293

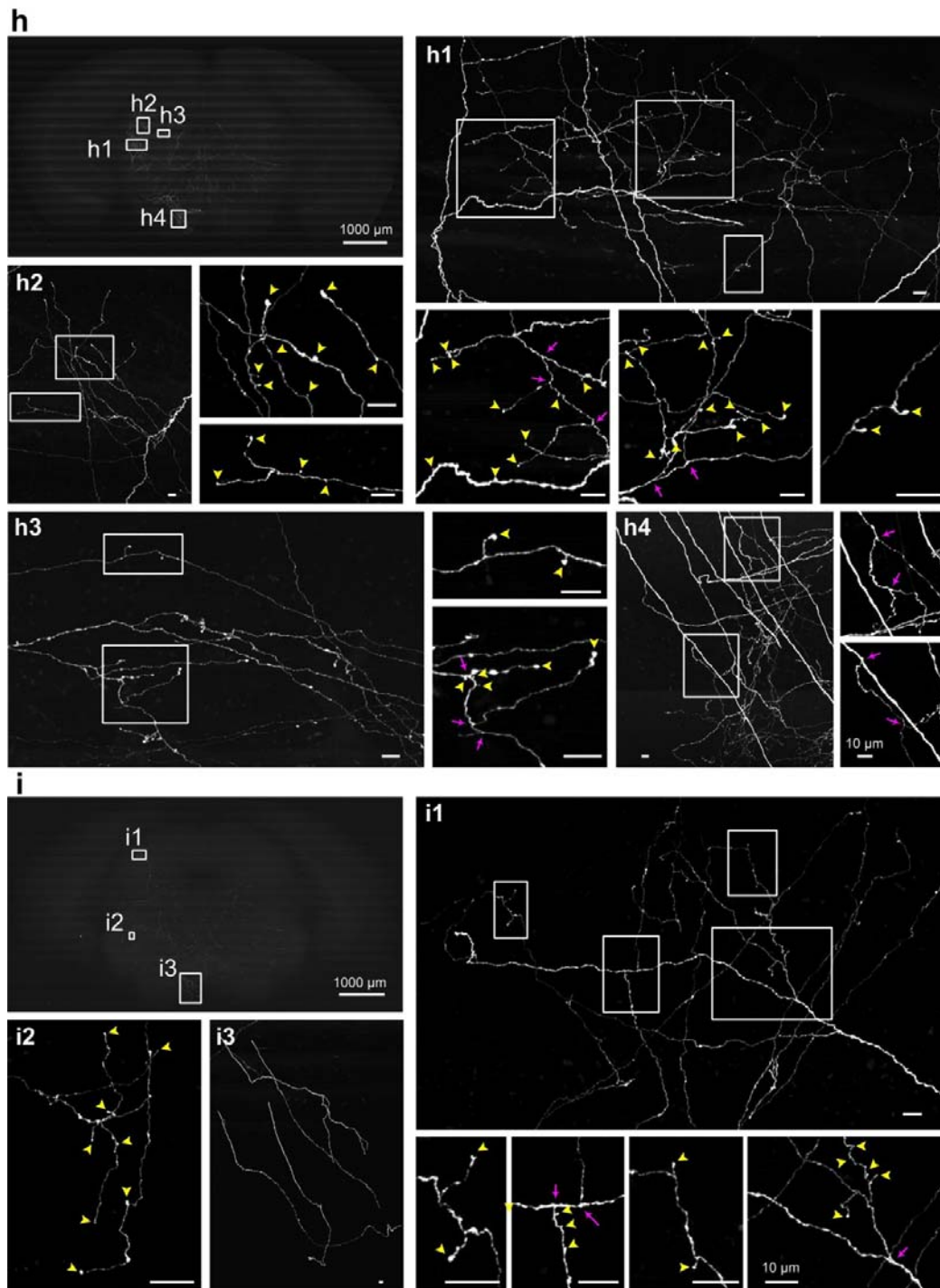1294 **Supplementary Figure 9** (continued)**:**

1295

1296

1297 **Supplementary Figure 9** (continued)**:**

1298

1299

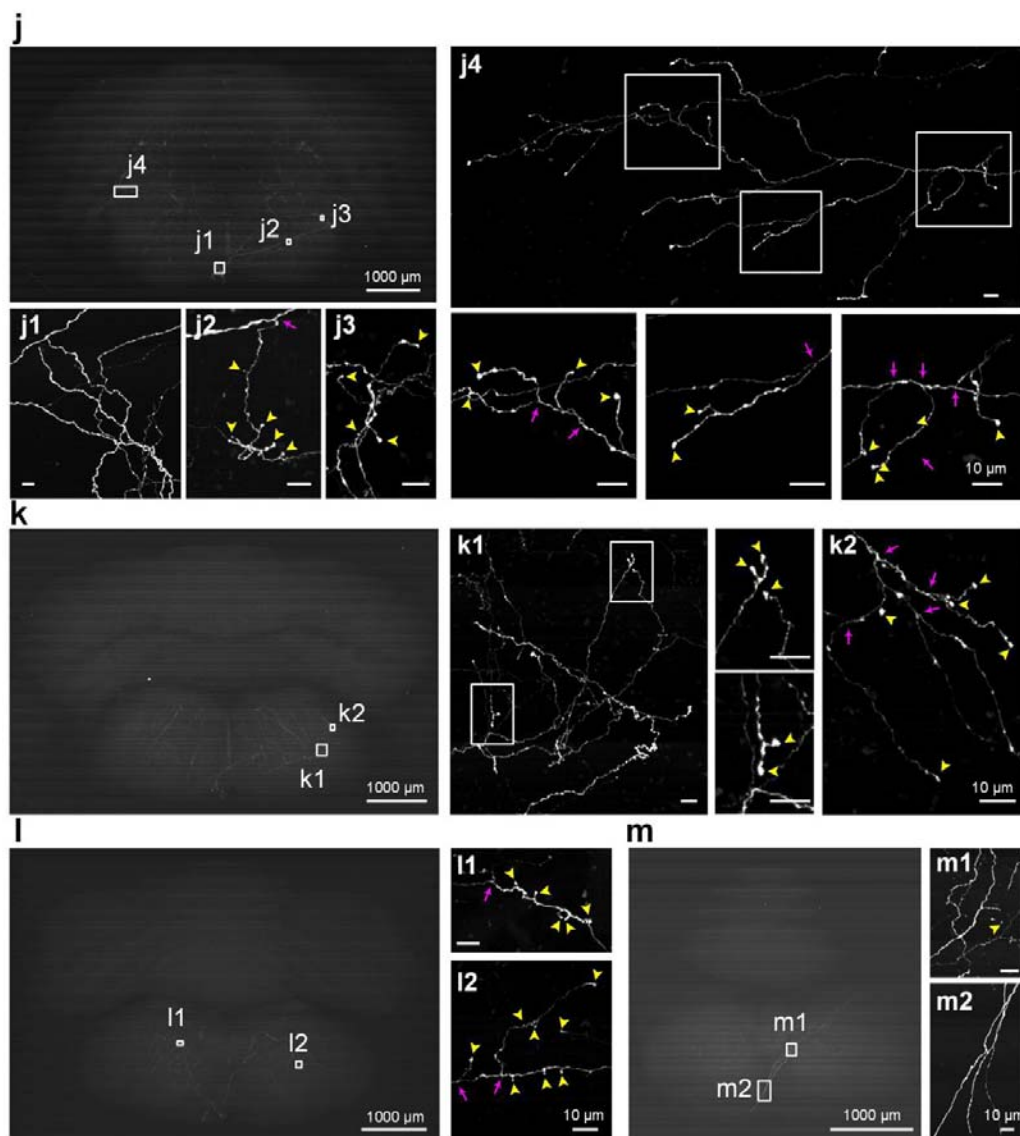1300 **Supplementary Figure 9** (continued)**:**

1301

1302

1303

1304

1305 **Supplementary Figure 9** (continued)**:**
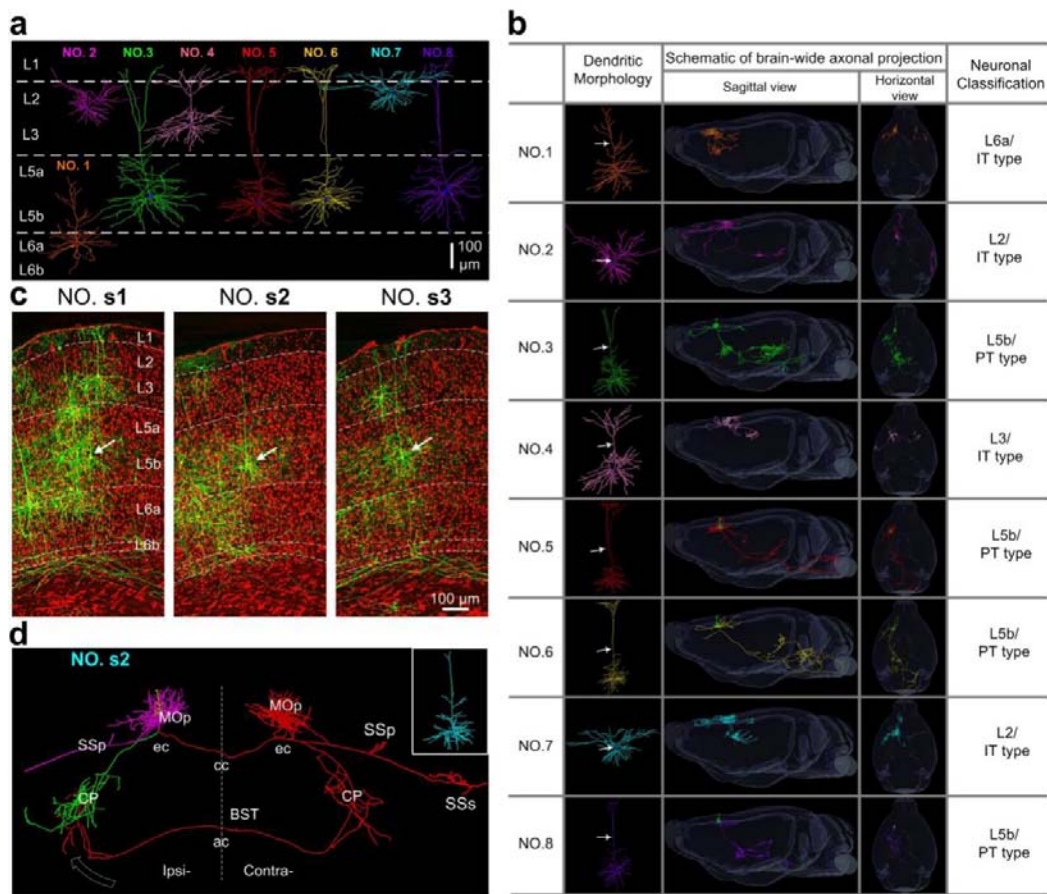

1306

1307 **Supplementary figure 9**

1308 **Whole-brain data sets of MOp (labeled with lAAV[200,000]).**

1309 **a** and **b** were maximum-intensity projections of 800 and 1,600 coronal sections. **c-l**
1310 were maximum-intensity projections of 1000 coronal sections and **m** was maximum-
1311 intensity projections of 420 coronal sections, respectively. All other images were
1312 enlargements of respective box regions showing the injection site or fine structures,
1313 including axonal branches (indicated by purple arrows) and terminal boutons
1314 (indicated by yellow arrowheads).

1315

1316

1318

Supplementary figure 10

Localization, dendritic and axonal morphologies of the reconstructed MOp pyramidal neurons.

(a) Gallery of dendritic morphologies and approximate laminar distributions of eight reconstructed pyramidal neurons (No.1-8).

(b) Gallery of Axonal morphologies and probable classifications of 8 neurons. White arrows indicate apical dendrites.

(c) Composite coronal sections show the locations of the cell body of neurons **s1**-**s3,** which were indicated by white arrows (EYFP signals were in green with 100-µm thickness and cytoarchitectonic reference, i.e. propidium iodide (PI) signals were in red with 10-µm thickness). White dashed lines define boundary of cortical layers.

(d) Localization of the brain-wide axonal projections of neurons **s2** (dendrites: yellow; local axons: magnet; left branches and right branches originated from ipsilateral external capsule were in green and red color, respectively). The brain regions were

1333 defined according to the Allen Brain Atlas (ABA) with the aid of the PI signals.
1334 Dashed white arrows pointed terminated directions of main axons.

1335 **Supplementary Figure 11**
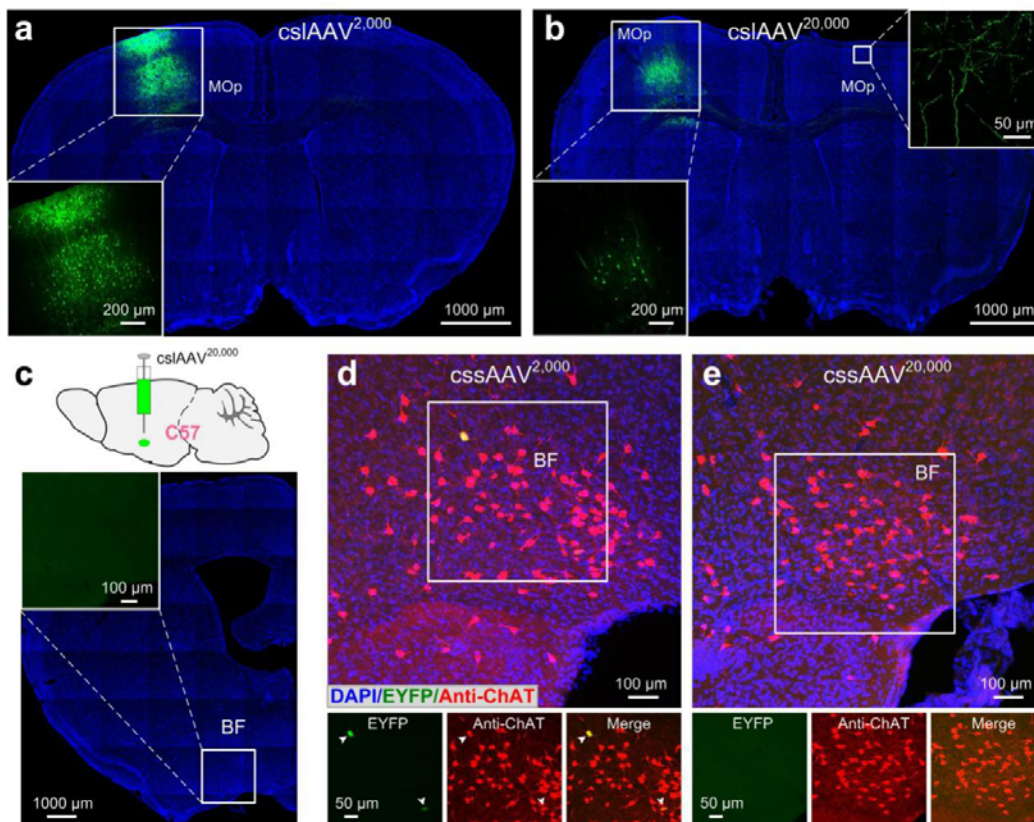
1336

1337 **Supplementary figure 11**

1338 **Validation of cell-type-specific labeling strategy with cslAAVs in Thy1-Cre and**
1339 **ChAT-Cre transgenic mice.**

1340 **(a-b)** Two versions of cslAAVs, cslAAV^{2,000} (**a**) or cslAAV^{20,000} (**b**) were injected into
1341 MOp of Thy1-Cre transgenic mice to achieve tunable neuron labeling. Lower left
1342 insets in **a** and **b** were enlargements of the corresponding boxes showing labeling in
1343 injection sites. Upper right inset in **b** was contralateral MOp axonal projections.

1344 **(c)** 100nl cslAAV^{20,000} was injected into basal forebrain (BF) of wild-type mice, we
1345 found no neurons were labeled across the injection site of 4 injected mice 21d later,
1346 indicating that the expression of cslAAVs was strictly restricted to Cre-driver lines**.**

1347 **(d-e)** For control experiments, we injected 100 nl two diluted ratios of Flp-expressing
1348 rAAV: Flp- and Cre-dependent rAAVs mixtures (abbreviated for cssAAV^{2,000} and
1349 cssAAV^{20,000} hereafter, in which the Flp-expressing rAAV was diluted to ratios of
1350 1:2,000 and 1:20,000 in PBS respectively before equally mixed with Flp- and Cre-
1351 dependent rAAV into BF of ChAT-Cre transgenic mice (n = 5 mice each). We found

1352   no labeled neurons were detectable in cssAAV^{20,000}-treated mice and in cssAAV^{2,000}-

1353   treated mice, only two mice each contained three or four faintly labeled cholinergic

1354   neurons (note that the imaging parameters of EYFP were much higher than **Fig. 3c**)

1355   whereas the other three mice rarely contained any signals in injection sites.
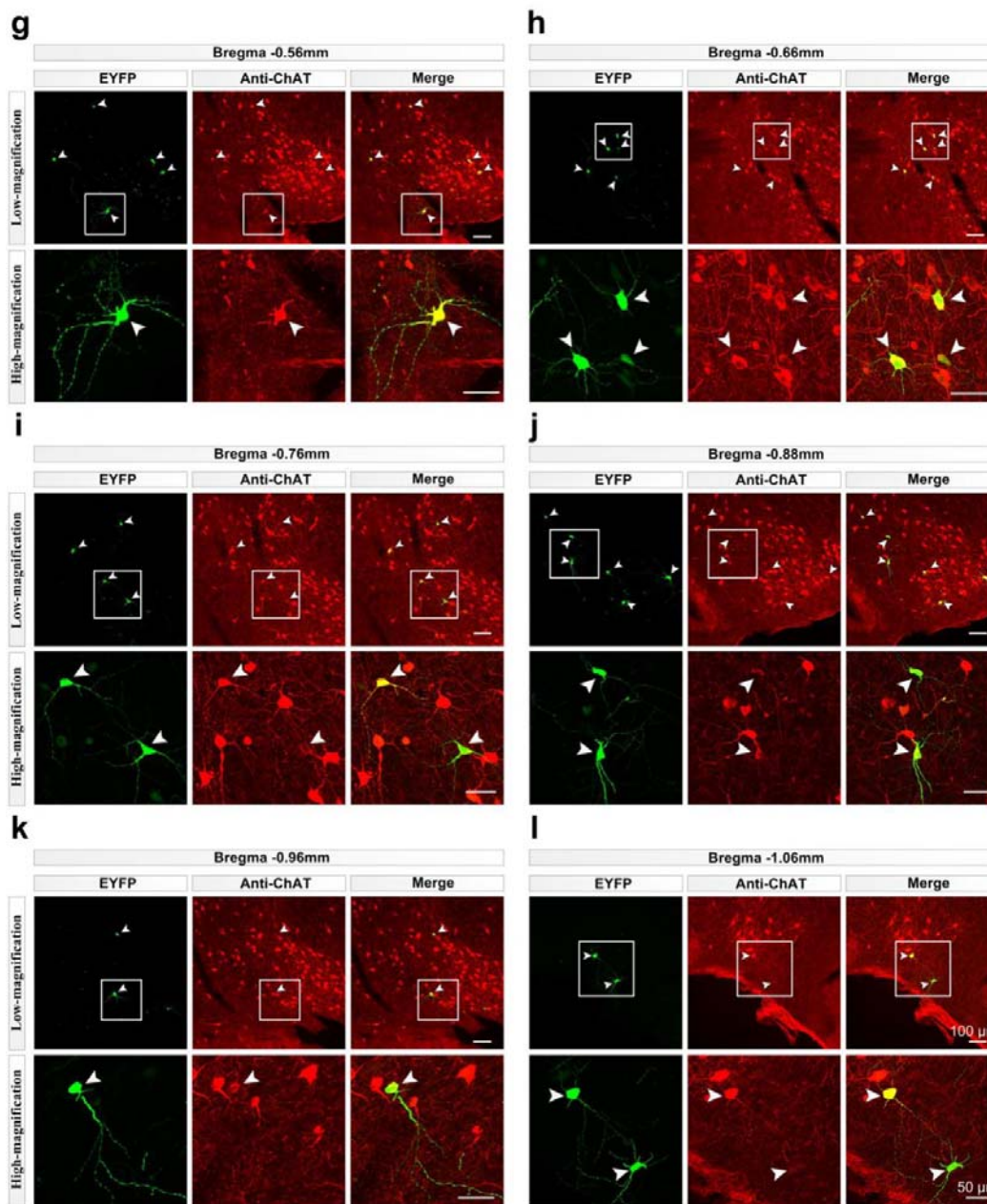
1356

Supplementary Figure 12
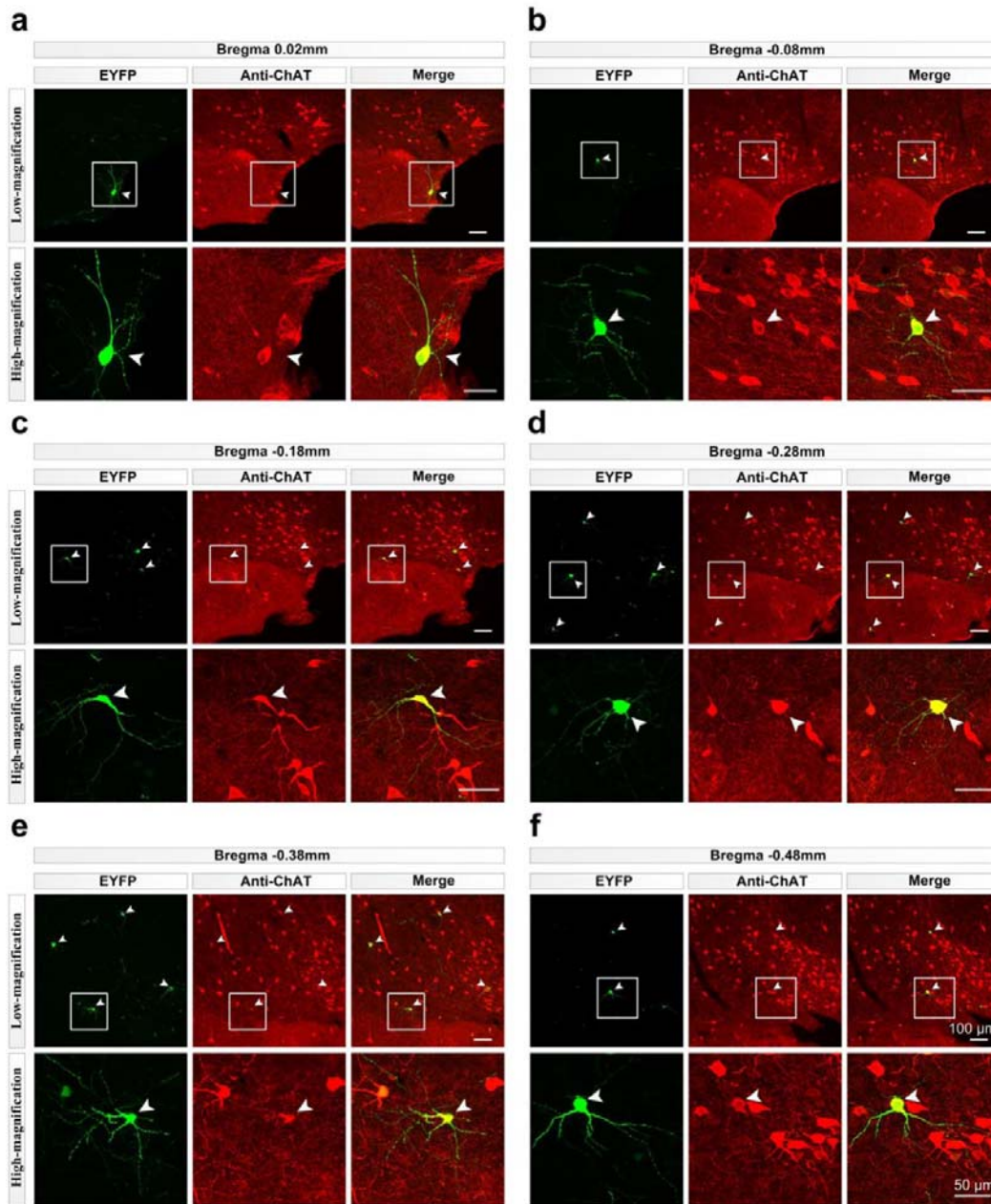
1358

1359

1360

Supplementary Figure 12 (continued)**:**

Supplementary figure 12

Cell-type-specific, sparse and super-bright BF cholinergic neuron labeling.
Twelve 50-μm thickness coronal sections ranging from Bregma 0.02 mm to Bregma -1.06 mm of the injection site were selected from a cslAAV^{20,000}-labeled ChAT-Cre transgenic mouse sample and displayed with a 50-μm intervals and immunostained with anti-ChAT antibody. Upper panels of **a-l** were low-magnification images showing overall labeling on each section and lower panels were high-magnification images of the corresponding boxes. Colabeled neruons were indicated by white arrowheads. This brain sample contained 62 labeled neurons (mouse 4 in

1372 **Supplementary Table 1**) and all of them were ChAT-positive and approximately 39
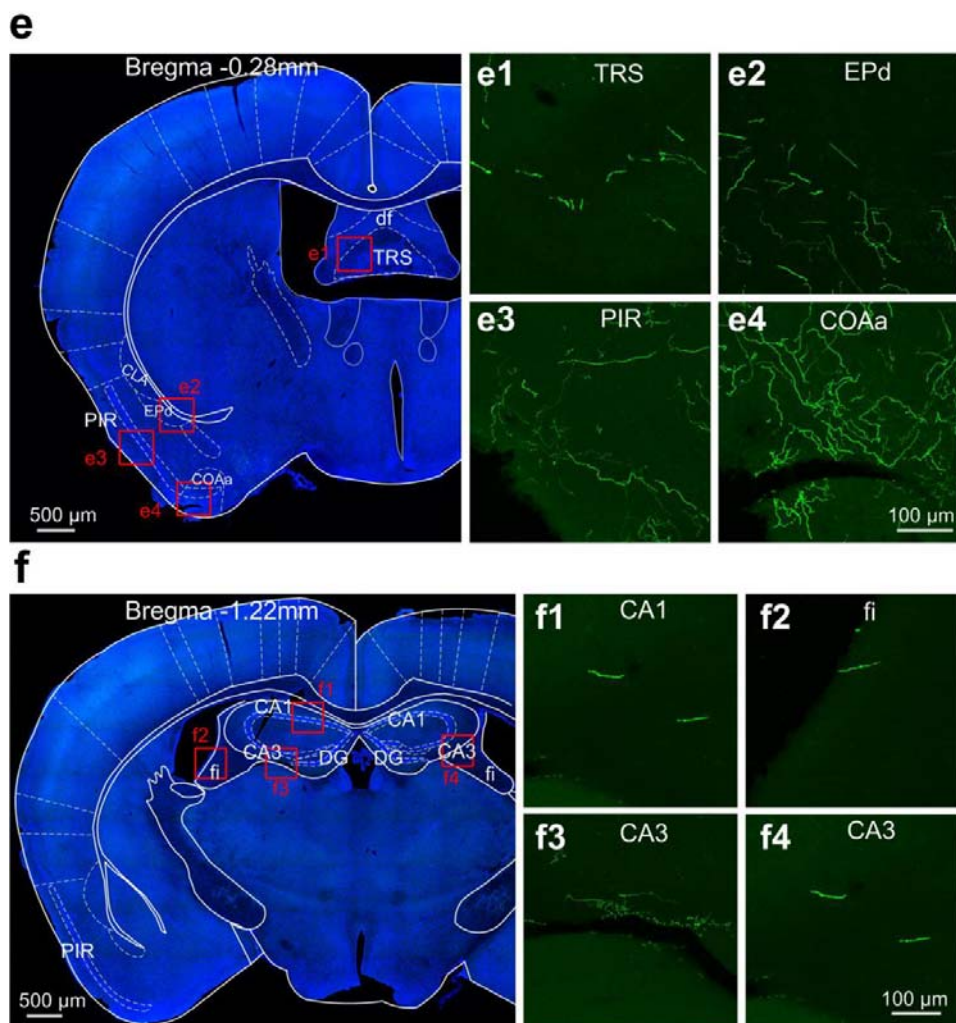1373 neurons were listed here.

1374

1375 **Supplementary Figure 13**
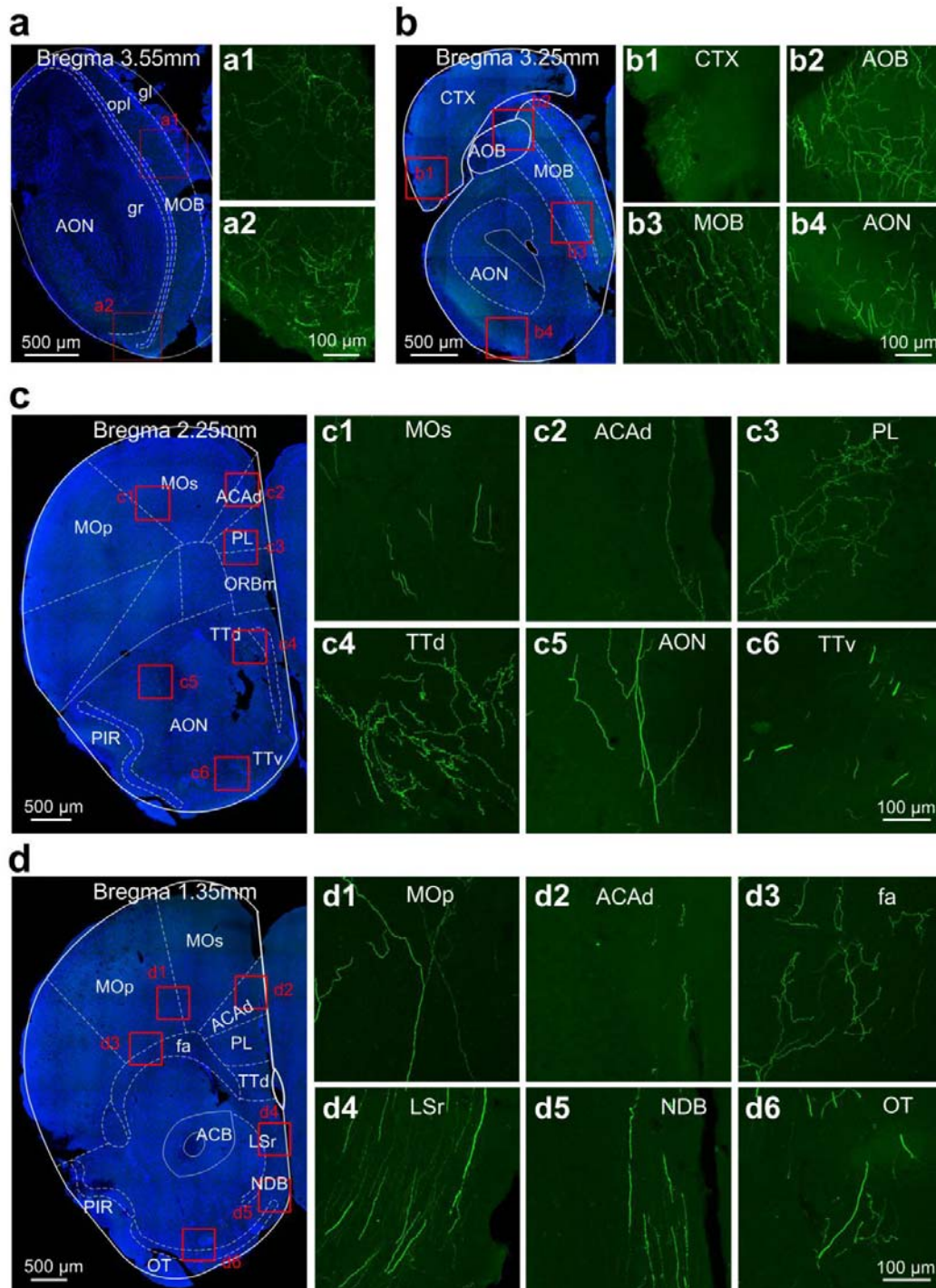
1376

1377

1378 **Supplementary Figure 13** (continued)**:**

1379

1380 **Supplementary figure 13**

1381 **Brain-wide long-range projections of BF cholinergic neurons.**

1382 Six coronal sections from a representative cslAAV[20,000]-labeled ChAT-Cre transgenic
1383 mouse brain sample were selected to show long-range projections of BF cholinergic
1384 neurons. **a1-a2**, **b1-b4**, **c1-c6**, **d1-d6**, **e1-e4** and **f1-f4** were maximum-intensity
1385 projections of the respective boxed regions in **a-f** showing the details of the axonal
1386 projections in different brain regions.

1387 Abbreviations: ACAd, Anterior cingulate area, dorsal part; ACB, nucleus accumbens;
1388 AOB, accessory olfactory bulb; AON, accessory olfactory nucleus; CA1, field CA1 of
1389 hippocampus; CA3, field CA3 of hippocampus; CLA, claustrum; COAa, cortical
1390 amygdalar area, anterior part; CTX, cerebral cortex; df, dorsal fornix; DG, dentate
1391 gyrus; ENd, endopiriform nucleus, dorsal part; fa, fcorpus callosum, anterior forceps;
1392 fi, fimbria of the hippocampus; LSr, lateral septal nucleus, rostral (rostroventral) part;

1393 MOB, main olfactory bulb; MOBgl, main olfactory bulb, glomerular layer; MOBgr,
1394 main olfactory bulb, granule layer; MOBopl, main olfactory bulb, outer plexiform
1395 layer; MOp, primary motor area; MOs, secondary motor area; NDB, diagonal band
1396 nucleus; ORBm, orbital area, medial part; OT, olfactory tubercle; PIR, piriform area;
1397 PL, Prelimbic area; TRS, triangular nucleus of septum; TTd, taenia tecta, dorsal part;
1398 TTv, taenia tecta, ventral part.

1399

1400 **Supplementary Figure 14**

1401

1402

1403

1404

1405 **Supplementary figure 14**

1406 **Quantitative analysis of MOp boomerang neurons** (No. **s1-s3**) **and BF cholinergic**
1407 **neurons** (No. **c1-c4**).

1408 For three boomerang neurons, dendrites were depicted in yellow, local axons were in
1409 magnet, left branches and right branches originated from ipsilateral external capsule
1410 were in green and red color, respectively for better differentiation. White arrows
1411 indicate apical dendrites. For four cholinergic neurons, coarse outlines and green dots
1412 indicated approximate locations of cell body, brain-wide long-range projections were
1413 demonstrated in sagittal and horizontal views, dendritic morphologies were depicted
1414 in yellow (No. **c1-c3**) and white (No. **c4**).

1415

1416

1417

1418

1419

1420

1421

1422

1423

1424

1425

1426

1427

1428

1429

1430

1431

1432

1433   **Supplementary Figure 15**
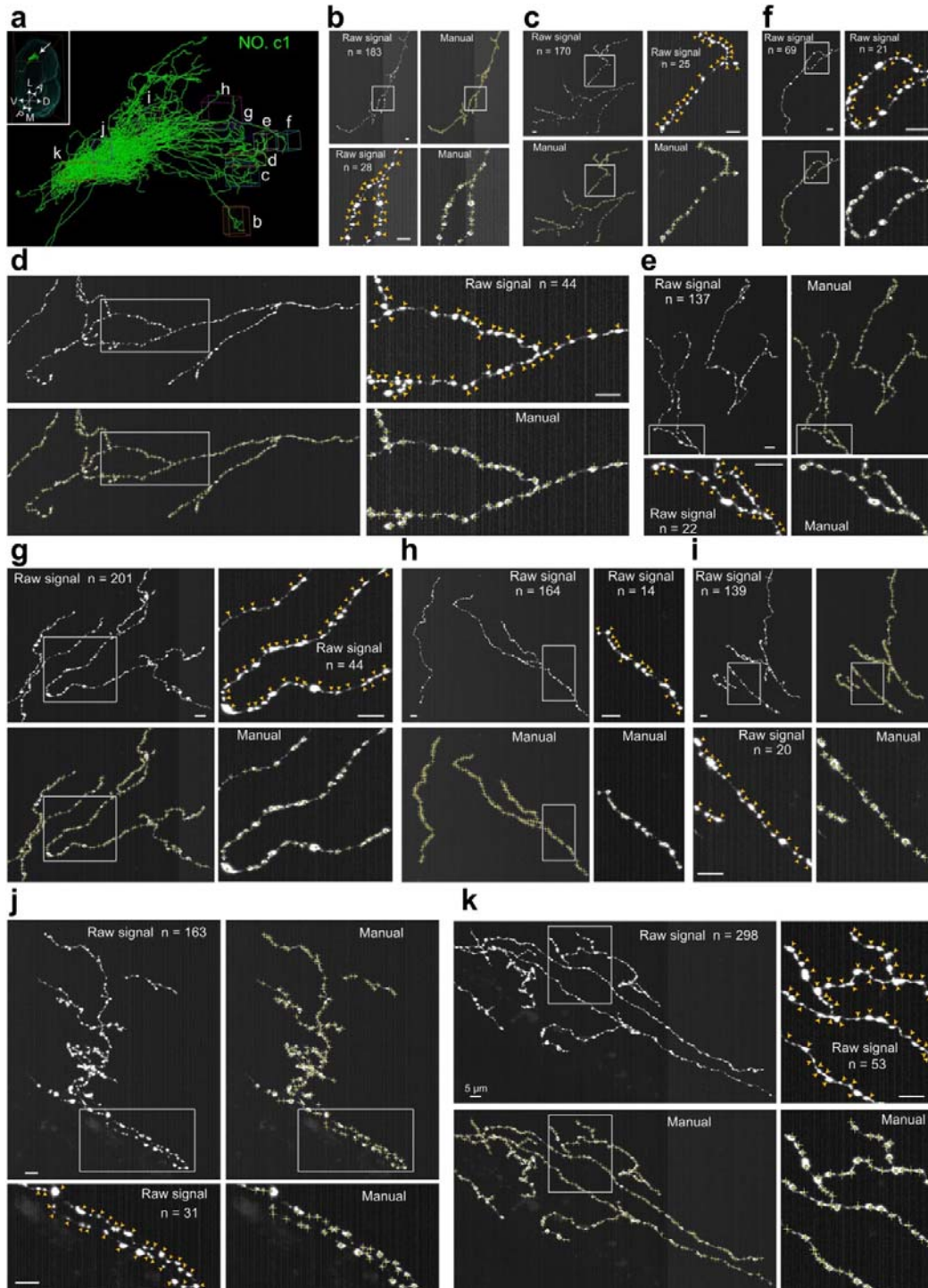
1434

1435

1436

1437

1438 **Supplementary figure 15**

1439 **Schematic of identifying presynaptic axonal boutons with a representative**
1440 **cholinergic neuron (No. c1).**

1441 **(a)** Overview of ten regions of interest (ROIs, **b-k**) randomly selected from No. **c1** for
1442 bouton identification.

1443 **(b-k)** Demonstration of raw signals (indicated by yellow arrowheads) and manual
1444 identification of boutons with ImageJ (indicated by yellow crosses) of ten ROIs in **a**.

1445

1446

1447

1448

1449

1450

1451

1452

1453

1454

1455

1456

1457

1458

1459

1460

1461

1462

1463

1464

1465

1466 **Supplementary Table 1. Quantifications of starter cells and total input cells of**
1467 **lAAV-DIO-GT/RG and sAAV-DIO-GT/RG labeling groups.**

Total number of starter cells						
	Mouse 1	Mouse 2	Mouse 3	Mouse 4	Mouse 5	Mean ± sem
lAAV-DIO-GT/RG	2,999	2,308	2,396	1,940	2,286	2,386 ± 172
sAAV-DIO-GT/RG	1,842	2,406	2,155	1,974	1,817	2,039 ± 127
Total number of input cells across the whole brain						
lAAV-DIO-GT/RG	150,915	132,027	113,278	115,100	105,647	123,393 ± 9,076
sAAV-DIO-GT/RG	81,771	70,309	72,182	43,507	54,665	64,487 ± 7,617

1468

1469

1470

1471

1472

1473

1474

1475

1476

1477

1478

1479

1480

1481

1482

1483

1484

1485 **Supplementary Table 2. Abbreviations of anatomical structures according to the**
1486 **Allen Brain Atlas (ABA, http://mouse.brain-map.org/).**

Abbreviations	Definitions	Abbreviations	Definitions
AAA	Anterior amygdalar area	MOBgl	Main olfactory bulb, glomerular layer
ac	Anterior commissure	MOBgr	Main olfactory bulb, granule layer
ACAd	Anterior cingulate area, dorsal part	MOBopl	Main olfactory bulb, outer plexiform layer
ACB	Nucleus accumbens	MOp	Primary motor area
AI	Agranular insular area	MOs	Secondary motor area
AIp	Agranular insular area, posterior part	MRN	Midbrain reticular nucleus
APN	Anterior pretectal nucleus	MY	Medulla
AOB	Accessory olfactory bulb	MY-mot	Medulla, motor related
AON	Anterior olfactory nucleus	MY-sen	Medulla, sensory related
AUD	Auditory areas	NDB	Diagonal band nucleus
BLA	Basolateral amygdalar nucleus	OB	Olfactory bulb
BMA	Basomedial amygdalar nucleus	ORB	Orbital area
BST	Bed nuclei of the stria terminalis	ORBm	Orbital area, medial part
CA1	Field CA1 of hippocampus	OT	Olfactory tubercle
CA3	Field CA3 of hippocampus	P	Pons
CB	Cerebellum	PAG	Periaqueductal gray
CBX	Cerebellar cortex	PAL	Pallidum
cc	Corpus callosum	PARN	Parvicellular reticular nucleus
CEA	Central amygdalar nucleus	PB	Parabrachial nucleus
CEAc	Central amygdalar nucleus, capsular part	PCN	Paracentral nucleus
CEAl	Central amygdalar nucleus, lateral part	PERI	Perirhinal area
CEAm	Central amygdalar nucleus, medial part	PF	Parafascicular nucleus
CL	Central lateral nucleus of the thalamus	PG	Pontine gray
CLA	Claustrum	PIR	Piriform area
CP	Caudoputamen	PL	Prelimbic area
cpd	Cerebral peduncle	P-mot	Pons, motor related
COAa	Cortical amygdalar area, anterior part	PO	Posterior complex of the thalamus
CTXpl	Cortical plate	PPN	Pedunculopontine nucleus
CTXsp	Cortical subplate	PRNc	Pontine reticular nucleus, caudal part
CUN	Cuneiform nucleus	PRNr	Pontine reticular nucleus
df	Dorsal fornix	PRT	Pretectal region
dhc	Dorsal hippocampal commissure	P-sen	Pons, sensory related
DG	Dentate gyrus	py	Pyramid
DN	Dentate nucleus	RN	Red nucleus
DR	Dorsal nucleus raphe	RR	Midbrain reticular nucleus, retrorubral area
ec	External capsule	RSP	Retrosplenial area
ECT	Ectorhinal area	RT	Reticular nucleus of the thalamus
ENTm	Entorhinal area, medial part, dorsal zone	SC	Superior colliculus
EPd	Endopiriform nucleus, dorsal part	SCm	Superior colliculus, motor related
EPv	Endopiriform nucleus, ventral part	SCs	Superior colliculus, sensory related
fa	Corpus callosum, anterior forceps	SI	Substantia innominata
fi	Fimbria	SNc	Substantia nigra, compact part
FN	Fastigial nucleus	SNr	Substantia nigra, reticular part
FRP	Frontal pole, cerebral cortex	SPF	Subparafascicular nucleus
FS	Fundus of striatum	SPVI	Spinal nucleus of the trigeminal, interpolar part
GP	Globus pallidus	SS	Somatosensory areas
GRN	Gigantocellular reticular nucleus	SSp	Primary somatosensory area
GU	Gustatory areas	SSs	Supplemental somatosensory area
HIP	Hippocampal region	STN	Subthalamic nucleus
HPF	Hippocampal formation	STR	Striatum
HY	Hypothalamus	SUB	Subiculum
IC	Inferior colliculus	TEa	Temporal association areas
ILM	Intralaminar nuclei of the dorsal thalamus	TH	Thalamus
int	Internal capsule	TRS	Triangular nucleus of septum
IP	Interposed nucleus	TTd	Taenia tecta, dorsal part
IPN	Interpeduncular nucleus	TTv	Taenia tecta, ventral part
IRN	Intermediate reticular nucleus	VAL	Ventral anterior-lateral complex of the thalamus
LAT	Lateral group of the dorsal thalamus	VISal/l	Anterolateral/lateral visual area
LHA	Lateral hypothalamic area	VISC	Visceral area
LSc	Lateral septal nucleus, caudal (caudodorsal) part	VM	Ventral medial nucleus of the thalamus
MBmot	Midbrain, motor related	VNC	Vestibular nuclei
MBsta	Midbrain, behavioral state related	VP	Ventral posterior complex of the thalamus
MD	Mediodorsal nucleus of thalamus	VPL	Ventral posterolateral nucleus of the thalamus
MED	Medial group of the dorsal thalamus	VPM	Ventral posteromedial nucleus of the thalamus
ml	Medial lemniscus	VTA	Ventral tegmental area
MO	Somatomotor areas	ZI	Zona incerta

1487

1488

1489

Supplementary Table 3. The total numbers of labeled neurons across the whole brain after labeling with the indicated lAAVs , sAAVs and cslAAVs in different regions.

Non-cell-type-specific labeling with lAAVs (wild-type mice)

Injection site		Coordinates	Cell number across the whole brain				
			Mouse 1	Mouse 2	Mouse 3	Mouse 4	Mean ± sem
MOp	lAAV^{20,000}	AP= 1.54 ML= -1.60 DV= -1.60	652	916	688	329	646 ± 121
	lAAV^{200,000}		74	68	58	77	69 ± 4
	sAAV^{20,000}		100	182	260	236	195 ± 35
	sAAV^{40,000}		103	183	151	114	138 ± 18
	sAAV^{80,000}		66	36	16	59	44 ± 11

lAAV^{200,000}

	Coordinates	Mouse 1	Mouse 2	Mouse 3		Mean ± sem
CA3	AP= -1.7; ML= -2.0; DV= -2.0	49	75	59		61 ± 8
CA1	AP= -1.7; ML= -2.0; DV= -1.5	150	98	137		128 ± 16

Cell-type-specific labeling with cslAAVs (Cre-driver transgenic mice)

		Coordinates	Mouse 1	Mouse 2	Mouse 3	Mouse 4	Mean ± sem
Mop	cslAAV^{20,000}	AP= 1.54 ML= -1.6 DV= -1.6	497	573	580		550 ± 27
Basal forebrain	cslAAV^{20,000}	AP= 0.21 ML= -1.5 DV= -5.5	46	58	48	62	54 ± 4
VTA	cslAAV^{8,000}	AP= -3.4 ML= -0.3 DV= -4.1	116	137	159	214	157 ± 21

1501 **Supplementary Table 4. Quantifications of presynaptic axonal boutons of four**
1502 **cholinergic neurons (No. c1-c4).**

	No.c1			No.c2			No.c3			No.c4		
	Number of boutons	Axonal length (μm)	density /μm	Number of boutons	Axonal length (μm)	density /μm	Number of boutons	Axonal length (μm)	density /μm	Number of boutons	Axonal length (μm)	density /μm
ROI-1	183	539.7119	0.3391	59	217.998	0.2706	43	154.5866	0.2782	45	142.4557	0.3159
ROI-2	170	652.3893	0.2606	45	146.6952	0.3068	112	336.6172	0.3327	41	108.3174	0.3785
ROI-3	209	615.2699	0.3397	43	156.8266	0.2742	41	178.8266	0.2293	113	383.7817	0.2944
ROI-4	298	919.7885	0.324	38	125.9487	0.3017	58	210.1786	0.276	46	197.7769	0.2326
ROI-5	69	177.9003	0.3879	39	160.4843	0.243	41	142.1778	0.2884	52	189.0938	0.275
ROI-6	137	407.4272	0.3363	33	96.53236	0.3419	69	233.0409	0.2961	57	169.729	0.3358
ROI-7	201	568.9249	0.3533	59	192.9515	0.3058	46	172.0581	0.2674	64	240.632	0.266
ROI-8	163	772.5238	0.211	69	151.3374	0.4559	62	248.3191	0.2497	43	130.3187	0.33
ROI-9	164	490.4556	0.3344	48	176.4415	0.272	73	298.1006	0.2449	146	386.982	0.3773
ROI-10	139	441.6116	0.3148	36	147.8423	0.2435	56	171.7005	0.3261	34	106.6103	0.3189
Mean	173.3	558.6003	0.3201	46.9	157.305786	0.3015	60.1	214.5606	0.2789	64.1	205.56975	0.3124
SEM	18.637507	64.5331285	0.0158	3.7340773	10.6693277	0.0197	6.8190094	20.31245507	0.0106	11.485692	32.7300585	0.0148
Estimated number of boutons	64,295 ± 3,174			147,958 ± 9,668			56,592 ± 2,151			125,138 ± 5,928		

1503

1504

1505

1506 **Supplementary Table 5. Summary of viruses used in this study.**

Part I----rAAVs

		Plasmids (µg/µl)	Titres (viral genome/ml)	Notes
Verification of viral interactions				
	lAAV-EYFP/mCherry	A. pAAV-EF1α-EYFP (1.0 µg/µl)	5.0×10^{12}	Plasmids A and B were pre-mixed at a ratio of 1:1
sAAV-EYFP/mCherry	rAAV2/9-EF1α-EYFP		5.0×10^{12}	rAAV2/9-EF1α-EYFP and rAAV2/9-EF1α-EYFP were post-mixed at a ratio of 1:1, generating sAAV-EYFP/mCherry
	rAAV2/9-EF1α-mCherry	B. pAAV-EF1α-mCherry (0.7 µg/µl)	5.0×10^{12}	
Non-cell type specific labelling systems (lAAVs)				
lAAVs	lAAV^{20,000}	A. pAAV-CMV-Cre (1.2 µg/µl);	4.0×10^{12}	Plasmids A and B were pre-mixed at a ratio of 1:20,000, 1:200,000 and 1:1,000,000, generating lAAV^{20,000}, lAAV^{200,000} and lAAV^{1,000,000}, respectively
	lAAV^{200,000}		7.0×10^{12}	
	lAAV^{1,000,000}	B. pAAV-EF1α-double floxed-EYFP-WPRE-HGHpA (Addgene #20296; 1.0 µg/µl)	2.9×10^{12}	
sAAVs	rAAV2/9-CMV-Cre		4.0×10^{12}	rAAV2/9-CMV-Cre and rAAV2/9-EF1α-double floxed-EYFP were post-mixed at a ratio of 1:20,000, 1:40,000, 1:80,000 and 1:1,000,000, generating sAAV^{20,000}, sAAV^{40,000}, sAAV^{80,000} and sAAV^{1,000,000}, respectively
	rAAV2/9-EF1α-double floxed-EYFP		1.0×10^{13}	
Cell-type-specific labelling systems (cslAAVs)				
cslAAVs	cslAAV^{2,000}	A. pAAV-EF1α-Flp (1.0 µg/µl);	7.1×10^{12}	Plasmids A and B were pre-mixed at a ratio of 1:2,000, 1:8,000 and 1:20,000, generating cslAAV^{2,000}, cslAAV^{8,000} and cslAAV^{20,000}, respectively
	cslAAV^{8,000}		6.0×10^{12}	
	cslAAV^{20,000}		7.0×10^{12}	
cssAAVs	rAAV2/9-EF1α-Flp	B. pAAV-hSyn Con/Fon EYFP (Addgene #55650; 1.0 µg/µl)	2.0×10^{12}	rAAV2/9-EF1α-Flp and rAAV2/9-hSyn Con/Fon EYFP were post-mixed at a ratio of 1:2,000 and 1:20,000, generating cssAAV^{2,000} and cssAAV^{20,000}, respectively
	rAAV2/9-hSyn Con/Fon EYFP		5.0×10^{12}	
Monosyanptic tracing systems				
sAAV-DIO-GT/RG	lAAV-DIO-GT/RG	A. pAAV-EF1α-DIO-EGFP-TVA (GT) (1.0 µg/µl)	7.0×10^{12}	Plasmids A and B were pre-mixed at a ratio of 1:2
	rAAV2/9-EF1α-DIO-EGFP-TVA		5.6×10^{12}	rAAV2/9-EF1α-DIO-EGFP-TVA and rAAV2/9-EF1α-DIO-RG were post-mixed at a ratio of 1:2, generating sAAV-DIO-GT/RG
	rAAV2/9-EF1α-DIO-RG	B. pAAV-EF1α-DIO-RG (0.5 µg/µl)	6.3×10^{12}	

Part II----RV

EnvA-SADΔG-DsRed	Titre: 2.0×10^{8} infectious particles/ml

1507

1508